In presenting this dissertation in partial fulfillment of the requirements for an advanced degree at Idaho State University, I agree that the Library shall make it freely available for inspection. I further state that permission to download and/or print my dissertation for scholarly purposes may be granted by the Dean of the Graduate School, Dean of my academic division, or by the University Librarian. It is understood that any copying or publication of this dissertation for financial gain shall not be allowed without my written permission.

Signature _____

Date _____

A MEASUREMENT OF THE POSITRON PRODUCTION EFFICIENCY

USING A QUADRUPOLE TRIPLET SYSTEM FOR A POTENTIAL

POSITRON SOURCE AT JEFFERSON LAB

by

Sadiq Setiniyaz (Shadike Saitiniyazi)

A dissertation

submitted in partial fulfillment

of the requirements for the degree of

Doctor of Philosophy in the Department of Physics

Idaho State University

May 2014

To the Graduate Faculty:

The members of the committee appointed to examine the dissertation of Sadiq Setiniyaz (Shadike Saitiniyazi) find it satisfactory and recommend that it be accepted.

_____

Tony Forest, Ph.D.

Major Advisor

_____

Yujong Kim, Ph.D.

Committee Member

_____

Dustin McNulty, Ph.D.

Committee Member

_____

Mahbub A. Khandaker, Ph.D.

Committee Member

_____

Wenxiang Zhu, Ph.D.

Graduate Faculty Representative

قەدىرلىك ئاتا ـ ئانام، ئىمانخان ھەمدۇللا ۋە سەتنىياز ئەخمەتكە
بىغىشلايمەن!

سادىق سەتنىياز

to my parents Imanhan Hemdulla and Setiniyaz Ahmet

Sadiq Setiniyaz

Acknowledgments

In the name of Allah, the most compassionate and the most merciful. All praise and thanks be to Allah, the creator, owner, and sustainer of the Worlds. Peace be upon prophet of Allah, Muhammad and his companions.

All success come from Allah alone. I thank Allah for giving me this wonderful life and ask him to guide me to the right path.

The research included in this dissertation could not have been performed if not for the assistance, patience, and support of many individuals. I would like to extend my gratitude first and foremost to my advisor Dr. Forest, who made this whole work possible. He has always been helpful with the every detail of my work. I am grateful to him and I appreciate his patience.

I would additionally like to thank Dr. Kim for his guidance on the accelerator physics area of my project and his support in revision process of my dissertation. He helped me to construct the experimental apparatus and built the foundations for the emittance measurement.

I would like to extend my appreciation to Dr. Chouffani for his guidance and assistance in this project. Dr. Chouffani's guided and helped in the beamline alignment, emittance measurement, magnet mappings, and many other aspects of this project.

I would also like to extend my appreciation to Dr. Freyberger who have collaborated with us in this project and conduct the emittance measurement with us. With his help and guidance I was able to successfully participated in the PEPPO (Polarized Electron and Polarized Positron) project in the Jefferson Lab.

I would like to thank my committee members Dr. McNulty, Dr. Khandaker and Dr. Zhu for their reviews of my dissertation and feedbacks.

I would like to acknowledge the outstanding efforts of Idaho Accelerator Center (IAC). Thanks to the engineers at IAC Chad O'Neill, Kevin Folkman, Brian Berls,

and John Ralph have been really helpful.

I would like to thank the Department of Physics at Idaho State University for making my PhD. study possible. I spend wonderful 6 years here. I love ISU, Pocatello, and the community here. I will always remember the smiling and friendly people here.

Thanks to my friends Oleksiy Kosinov, Jasen Swanson, Carlos Bula Villarreal, Zaijing Sun, Olga Cortes, Mikheil Titberidze, Jack Wang, Chris Eckman, and Anthony Andrews (aka Misha Titberidze) always there when I needed them.

Thanks to my friend Mayir Mamtimin and his wife Kadirya Dolqun. Because of them, I didn't feel homesick and life at Pocatello was more fun. Also thanks to Mamatimin Omar and his wife Gulzar Osmanjan for their hospitality and friendship.

Finally, and most importantly, I would like to thank my wife Mihrigul Eli. Her support, encouragement, quiet patience and unwavering love which laid the foundations for my success. I am thankful to my parents Setiniyaz Ahmet and Imanhan Hemdulla for raising me with love and care. My success of today would not possible without their support and faith in me.

Contents

List of Figures

List of Tables

Abstract

Positrons were produced using a tungsten target when impinged by an electron beam from the High Repetition Rate Linac (HRRL) in the Physics Department's Beam Lab at Idaho State University (ISU). The HRRL cavity was relocated. Dipole and quadrupole magnets were added to the new beamline. Insertable OTR and YAG screens were added to the beamline for beam diagnostics. Faraday cups were installed at the end of the 0, 45, and 90 degree beamlines to measure the electron beam current. The emittance, Twiss parameters, and energy distribution of the HRRL were measured.

The produced positrons were transported to another tungsten target where they annihilate and create 511 keV photons. Two shielded NaI detectors were positioned to measure 511 keV photons in coincidence with the pulsed electron gun. The intensity of the produced positrons were measured at five (1-5 MeV) different energies using the annihilation target. The ratio of positrons, detected by the NaI detectors, to electrons incident on the tungsten converter was on the order of 10^{-15}.

Simulations were performed using G4beamline to study the processes of position generation and transportation. The simulation was carried out in three steps, because of the large amount of beam loss that was observed during the initial simulation. While the simulation result agrees with the experiment in that the peak energy distribution is near 3 MeV, it predicts a higher positron to electron ratio.

Chapter 1

Introduction

The positron production efficiency using a proposed linac based quadrupole triplet collection system is measured in partnership with the Continuous Electron Beam Accelerator Facility (CEBAF) of Thomas Jefferson National Accelerator Facility (commonly referred to as Jefferson Lab or JLab) and the Idaho Accelerator Center (IAC) of Idaho State University (ISU). There has been substantial interest in developing a polarized positron source for the nuclear physics community [1]. The main challenge has been increasing the intensity and polarization of the beam. This work investigates a proposed method for collecting positrons using a quadrupole triplet system.

1.1 Different Approaches to Produce Positrons

Positrons are used in several disciplines of science, such as chemistry, physics, material science, surface science, biology and nanoscience [2]. Positrons may be obtained either from radioactive sources or from pair production of high energy photons. Radioactive sources like Co-58, Na-22, and Cu-64 emit positive beta particles β^+ when they decay. As given in Table 1.1, the positron rate of radioactive sources is about $10^7 \sim 10^8$ e$^+$/s because of the source activity limits of 100 mCi [3] that are imposed for radiation safety.

Positrons are available for use in experiments at the nuclear reactors [4] shown in Table 1.1. Neutrons are used to produce positrons from the photons emitted when neutrons interact with cadmium. Photons pair produce positrons within the tungsten foils positioned in the photon flux. The positron beam created in the nuclear reactor has the intensity shown in Table 1.1.

Table 1.1: Different Positron Sources [3, 4].

β^+ sources			
Source	Activity	Rate (e$^+$/s)	Facility/Source Type
Co-58	100 mCi	3×10^5	W-moderator
Na-22	100 mCi	2×10^6	W-moderator
Cu-64	80 Ci/cm^2	$10^7 \sim 10^8$	Brookhaven, reactor beam
Pair-production			
Energy		Rate (e$^+$/s)	Facility/Source Type
36 MeV		10^8	Giessen, LINAC
100 MeV		10^{10}	Livermore, LINAC
150 MeV		10^8	Oak Ridge, LINAC
5 keV		5×10^6	NC State University, reactor

Another common method used to generate positrons is by using an electron linear accelerator (linac). In this method, electrons, from the linac, incident on a high Z material like tungsten, produce positrons by bremsstrahlung and pair production. One of the advantages of the linac based positron beam is its variable energy, intensity, and the ability to pulse the source on and off at specific time intervals as given in Table 1.1.

1.2 Positron Beam Generation from Bremsstrahlung

When a moving charged particle interacts with the electric field of another charged particle, it can be deflected and lose energy in the form of photons, as shown in Figure 1.1. This interaction is known as the bremsstrahlung process. The probability of this interaction increases with the square of the atomic number of the material traversed by the incident charged particle. Figure 1.2 shows the photon energy distribution produced when the 12 MeV electron energy distribution from Figure 1.3 interacts with a 1 mm thick tungsten target. As shown in Figure 1.2, the distribution peaks at 0.3 MeV.
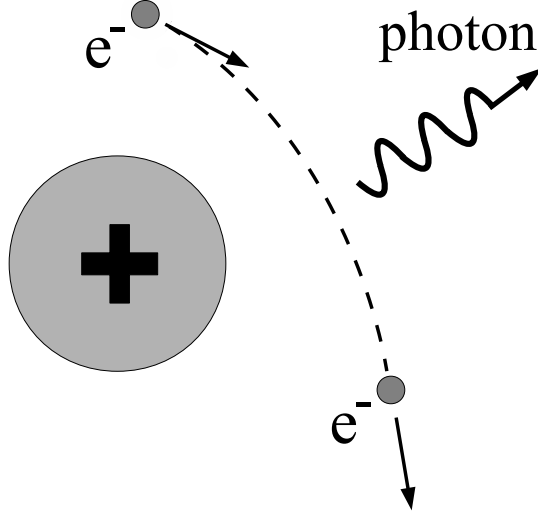
Figure 1.1: Photon emission from the bremsstrahlung processes.

The bremsstrahlung cross section for the energy range of this experiment is given by [5]

$$
\begin{aligned}
d\sigma = \ & 4Z^2 r_e^2 \alpha \frac{d\nu}{\nu} \left\{ \left(1 + \left(\frac{E}{E_0} \right)^2 \right) \left[\frac{\phi_1(\gamma)}{4} - \frac{1}{3} \ln Z - f(Z) \right] \right. \\
& \left. - \frac{2E}{3E_0} \left[\frac{\phi_2(\gamma)}{4} - \frac{1}{3} \ln Z - f(Z) \right] \right\},
\end{aligned}
\tag{1.1}
$$

where E_0 is the initial total energy of the electron, E is the final total energy of the electron, $\nu = \frac{E_0 - E}{h}$ is the frequency of the emitted photon, and Z is the atomic number of the target. $\gamma = \frac{100 m_e c^2 h \nu}{E_0 E Z^{1/3}}$ is the charge screening parameter, and $f(Z)$ is given by

$$
f(Z) = (Z\alpha)^2 \sum_1^\infty \frac{1}{n[n^2 + (Z\alpha)^2]},
\tag{1.2}
$$

where $\alpha = \frac{1}{137}$ is the fine-structure constant, ϕ_1 and ϕ_2 are screening functions that depend on Z.

There are three competing processes that a photon can undergo when interacting with matter. Figure 1.4 illustrates the cross-sections for the different interactions
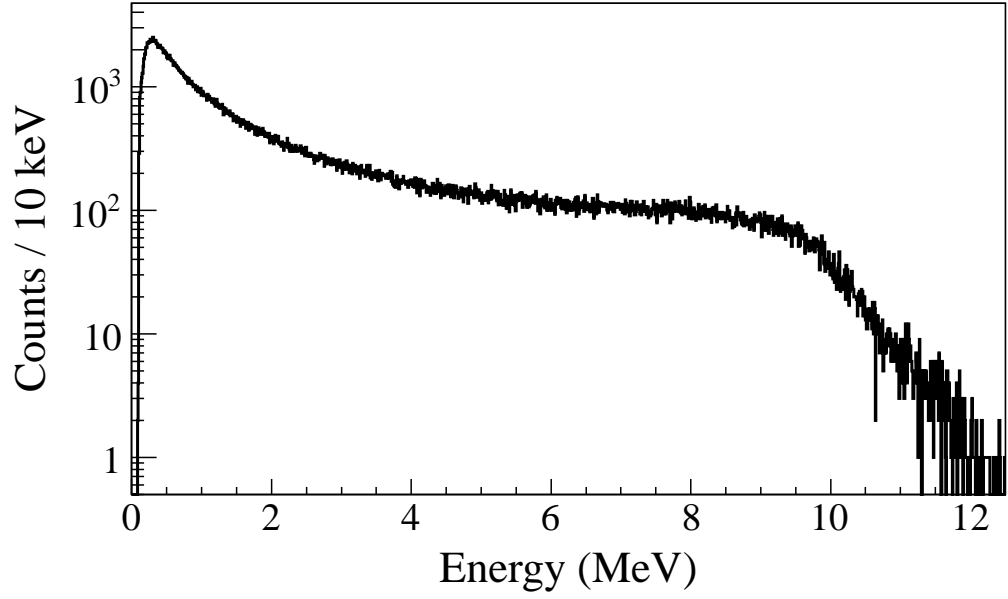
Figure 1.2: Bremsstrahlung photon energy distribution produced when the 12 MeV electron energy distribution from Figure 1.3 interacts with the simulation's 1 mm thick tungsten target.
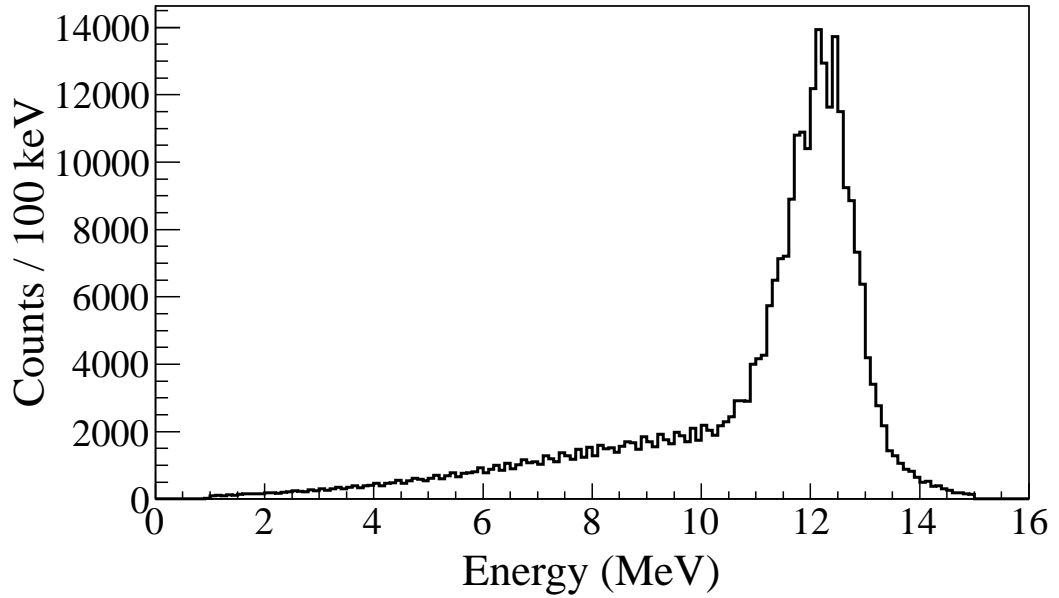
Figure 1.3: The electron energy distribution incident on a tungsten foil used in the simulation that is based on the measurements shown in Figure 3.6.

that can occur when a photon traverses tungsten as a function of photon energy. At electron volt (eV) energies, which are comparable to the electron atomic binding energy, the dominant photon interaction is the photoelectric effect. As the photon energy increases up to the kilo electron volt (keV) range, the Compton scattering process starts to be more dominant. Although the photon is totally absorbed during the photoelectric effect, photons merely lose energy when undergoing Compton scattering. As the photon energy reaches twice the rest mass energy of the electron, *i.e.* 2 × 511 keV, pair production begins to occur. Pair production becomes the dominant interaction process when photon energies are beyond 5 MeV [6]. In this process, a photon interacts with the electric field of the nucleus or the bound electrons and is converted into an electron and positron pair.
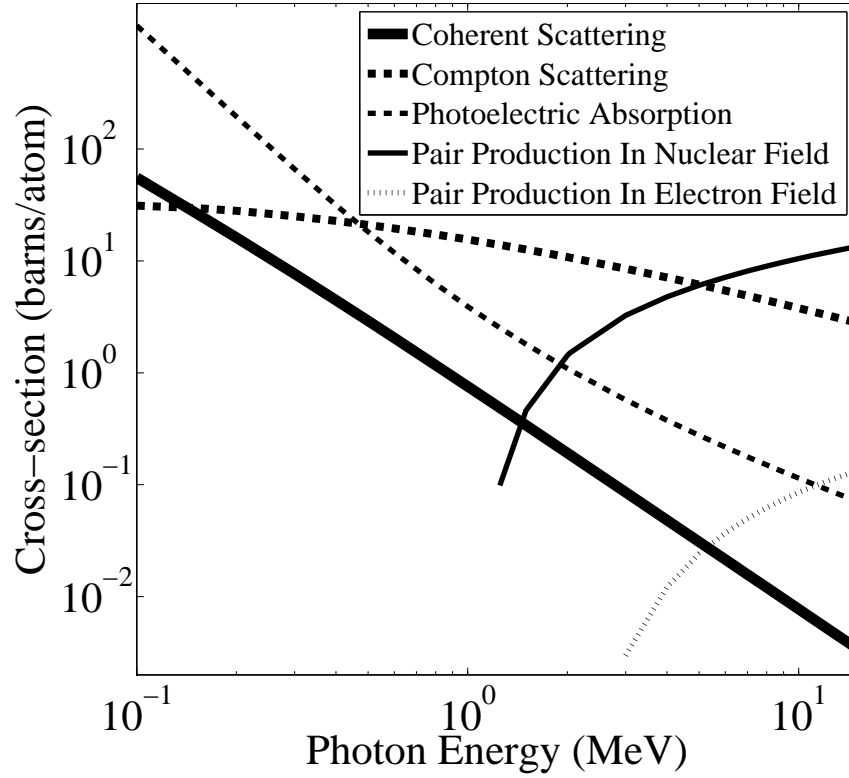
Figure 1.4: The cross-sections for the three photon interaction types with tungsten as a function of photon energy [7].

Using natural unit, where $c \equiv 1$, the differential cross-section for pair production

can be expressed as

$$\frac{d\sigma}{d\epsilon_1 d\theta_1 d\theta_2} = 8\left(\frac{\pi a}{\sinh(\pi a)}\right)^2 \frac{a^2}{2\pi}\frac{e^2}{\hbar c}\left(\frac{\hbar}{m_e c}\right)^2 \frac{\epsilon_1 \epsilon_2}{k^3}\theta_1\theta_2$$

$$\times\{\frac{V^2(x)}{q^4}\left[k^2(u^2 + v^2)\xi\eta - 2\epsilon_1\epsilon_2(u^2\xi^2 + v^2\eta^2) + 2(\epsilon_1^2 + \epsilon_2^2)uv\xi\eta cos(\phi)\right] \tag{1.3}$$

$$+a^2 W^2(x)\xi^2\eta^2\left[k^2(1 - (u^2 + v^2)\xi\eta - 2\epsilon_1\epsilon_2(u^2\xi^2 + v^2\eta^2)\right.$$

$$\left. -2(\epsilon_1^2 + \epsilon_2^2)uv\xi\eta\cos(\phi)\right]\},$$

where k is photon energy, θ_1 and θ_2 are the scattering angle of e^+ and e^- respectively, $\phi = \phi_1 - \phi_2$ is the angle between the e^+ and e^- pair, ϵ_1 and ϵ_2 are the energy of the positron and electron respectively. Other constants are $u = \epsilon_1\theta_1$, $v = \epsilon_2\theta_2$, $\xi = \frac{1}{1+u^2}$, $\eta = \frac{1}{1+v^2}$, $q^2 = u^2 + v^2 + 2uv\cos(\phi)$, $x = 1 - q^2\xi\eta$, $a = \frac{Ze^2}{\hbar c}$, $V(x) = 1 + \frac{a^2}{(1!)^2} + \frac{a^2(1+a^2)x^2}{(2!)^2} + \frac{a^2(1+a^2)(2^2+a^2)x^4 x^2}{(3!)^2} + \cdots$, and $W(x) = \frac{1}{a^2}\frac{dV(x)}{dx}$.

In pair production, positron and electron pairs are created back to back in the center of mass frame as given by

$$\gamma \rightarrow e^+ + e^-. \tag{1.4}$$

In the lab frame, electrons and positrons tend to move in the direction of the photon, as shown in Figure 1.5. The positron and electron carry away the energy from the photon that is in excess of 1.022 MeV. In the center of mass frame, the kinetic energy is equally shared. Photons with an energy above 1.022 MeV in the bremsstrahlung spectrum of Figure 1.2 have the potential to create electron and positron pairs. Figure 1.6 is the simulation of 10 million 12 MeV mono energetic electrons impinging on a 1.016 mm thick tungsten target. Turning on the annihilation process resulted in a 511 keV peak on top of the bremsstrahlung spectrum. This 511 keV peak represents photons produced when the created positrons from the pair production annihilate with atomic electrons inside the tungsten target.
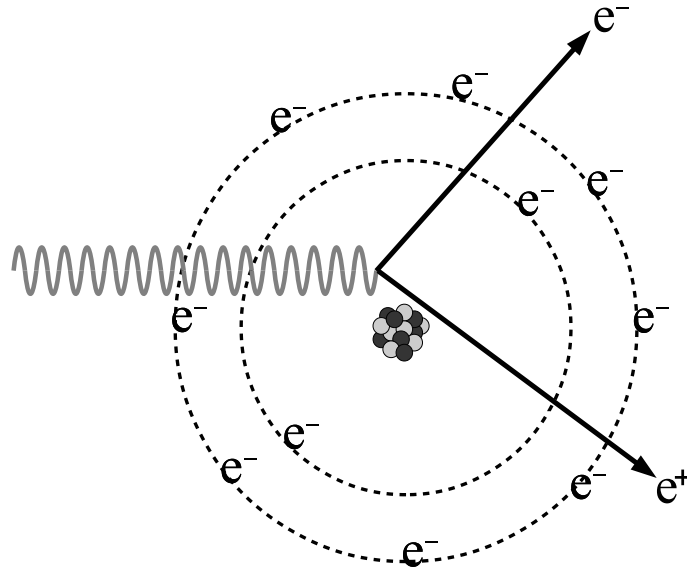
Figure 1.5: Pair production.
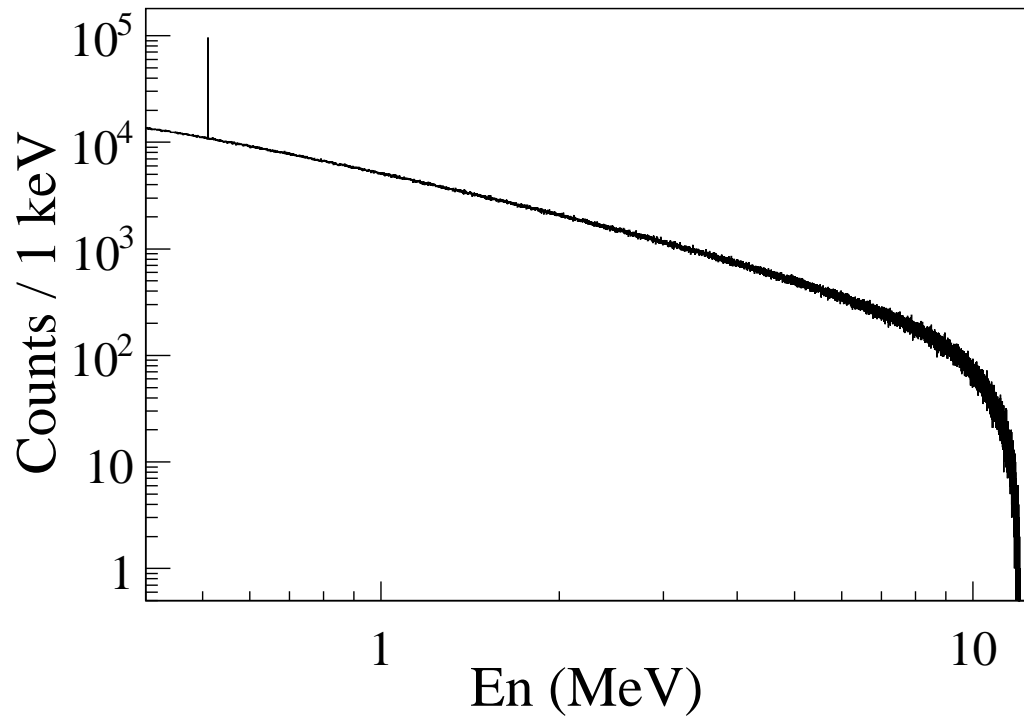
Figure 1.6: Photon spectrum created by one million 12 MeV mono energy electrons impinging on a 1.016 mm thick tungsten target.

1.3 Generation of Electron Beam Using a Linac

Electrons need to be accelerated, using a linac (linear particle accelerator), up to at least a few mega electron volts (MeV) in order to generate bremsstrahlung photons with enough energy to produce electron and positron pairs. A linac is a device that accelerates charged particles to nearly the speed of light using an electromagnetic wave. The HRRL (High Repetition Rate Linac), located in the Beam Lab of ISU's Physics Department, can accelerate electrons up to 16 MeV peak energy, and is a sufficient energy for positron production.

To optimize positron production, one needs to know the beam size and divergence of the electrons impinging the production target. The emittance and the Twiss parameters (α, β, and γ) quantify these beam properties and are used as the input parameters for accelerator simulation tools. These tools can study beam transport and predict beam properties (beam size and divergence) along the beam line.

1.3.1 Emittance and Twiss Parameters

In accelerator physics, a Cartesian coordinate system is used to describe the motion of the accelerated particles. As shown in Figure 1.7, the s-axis of the Cartesian coordinate system is defined as the natural coordinate that is oriented along the same direction as the beam momentum. The x-axis and y-axis are horizontal and vertical coordinates which constitute the transverse beam profile. The transverse beam profiles are described as a function of the longitudinal coordinates, $x(s)$ and $y(s)$.

The horizontal phase space x' vs. x (similar for y projection), shown in Figure 1.8, of the beam is an ellipse with invariant area along the beamline (under conditions that space charge effects, coherent synchrotron radiation, and wakefield are ignorable) [8].
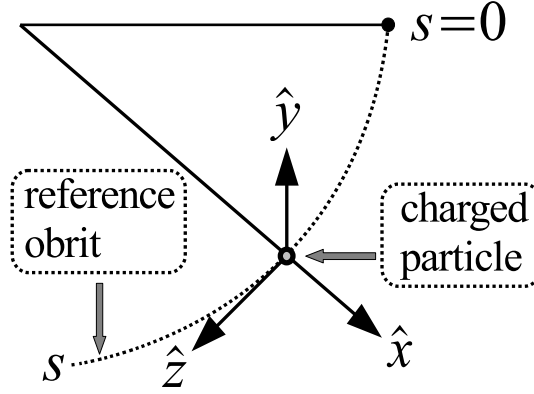
Figure 1.7: Coordinate system and reference orbit (dashed line) [8].

Here x' is defined as

$$x' = \frac{dx}{ds}. \tag{1.5}$$

The area of the ellipse is

$$A = \pi w = \pi(\gamma z^2 + 2\alpha z z' + \beta z'^2). \tag{1.6}$$

Here w is called the Courant-Snyder invariant [8] and α, β, and γ are called Twiss parameters. The transverse emittance, ϵ, of the beam is defined to be the area of the ellipse that contains a fraction of the particles. The units for the emittance are m·rad and mm·mrad. Conventionally used unit for emittance is μm, which is similar as mm·mrad (1 μm = 1 mm·mrad = 10^{-6} m·rad). Twiss parameters are useful because they are related to the beam size and divergence by

$$\sigma_x(s) = \sqrt{\epsilon_x(s)\beta_x(s)}, \ \sigma_{x'}(s) = \sqrt{\epsilon_x(s)\gamma_x(s)}, \tag{1.7}$$

where ϵ_x is the beam's horizontal emittance, σ_x is the horizontal rms beamsize, $\sigma_{x'}$ is the horizontal rms beam divergence, and β_x and γ_x are two of the three Twiss

parameters (same for vertical projection). The Twiss parameters are related by

$$\gamma = \frac{1 + \alpha^2}{\beta}. \tag{1.8}$$

The beam emittance is inversely proportional to the beam energy. As the electron
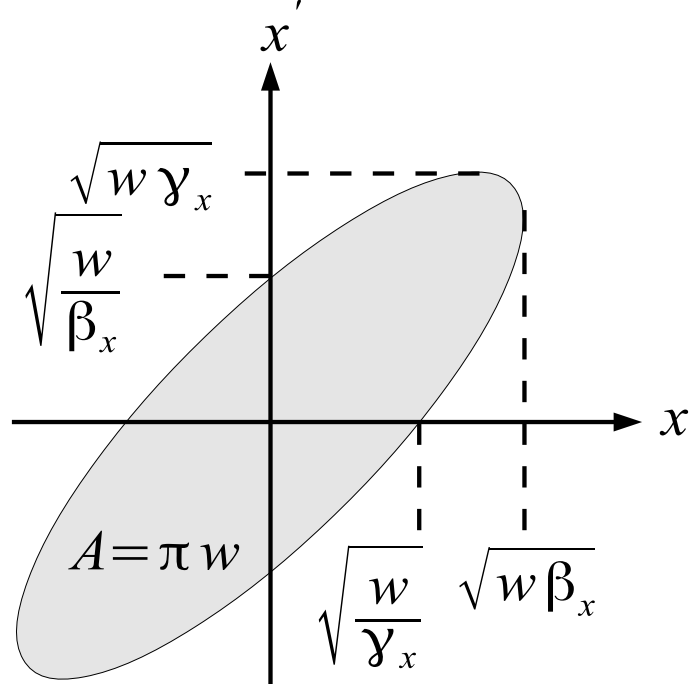
Figure 1.8: Phase space ellipse and its relation to the emittance and the Twiss parameters α, β, and γ [8].

beam gains energy during acceleration, the divergence of the beam decreases because the momentum increases in the forward direction. This emittance decrease due to the energy gain is called adiabatic damping. Thus, it is more practical to use normalized emittance which is defined as

$$\epsilon_\mathrm{n} = \beta\gamma\epsilon, \tag{1.9}$$

where β is c/v, γ is relativistic (Lorentz) factor, and ϵ unnormalized emittance.

In this chapter, the possible ways to generate positrons were described. Positrons

from radioactive sources have lower intensities due to safety limits placed on the source activity. Positrons from reactors have intensities comparable to radioactive sources but are low in energy. Generating positrons using a linac can produce higher energy positrons at higher fluxes than reactors.

Chapter 2 discusses the hardware used in this experiment and the tools used to measure emittance, Twiss parameter, and energy of the HRRL. The measured emittance, Twiss parameter and energy, as well as the positron production efficiency are discussed in the Chapter 3. The simulation of the positron production efficiency and transportation process are compared with measurement in Chapter 4. The conclusion from this work is presented in Chapter 5.

Chapter 2

Apparatus

This chapter describes the apparatus and associated hardware used in the experiment to produce positrons as described in Chapter 1. The new HRRL beamline was constructed using two dipoles as well as ten quadrupoles to optimize the beam transportation. Beamline elements were aligned using a laser alignment system. Additional beamline elements such as an energy slit, beam viewers, and Faraday cups were added. Two NaI detectors were installed at the end of the beamline and were used to detect 511 keV photons emitted when positrons annihilate in a second tungsten target.

2.1 HRRL Beamline

A 16 MeV S-band (2856 MHz RF frequency) standing-wave High Repetition Rate Linac (HRRL) located in the Department of Physics Beam Lab at Idaho State University was used to impinge a 12 MeV electron beam onto a tungsten foil. The energy of the HRRL is tunable between 3 to 16 MeV and its repetition rate is variable from 1 to 300 Hz. The operating parameters of the HRRL are given in Table 2.1. As shown in Figure 2.1, the HRRL has a thermionic gun, vertical and horizontal steering magnet sets on two ends, and two solenoid magnets. The startup, shutdown, and beam optimization procedures of the HRRL are given in the Appendix C.

The accelerator's cavity was relocated to the position shown in Figure 2.2 to provide enough space for a beam line that can transport achromatic positrons or electrons. The beam elements are described in Table 2.2. Quadrupole and dipole magnets, described in Appendix D, were added to the new beam line as well as an OTR and YAG view screen to measure and monitor the beam profile and position.

Table 2.1: The Basic Parameters of the HRRL.

Parameter	Unit	Value
maximum energy	MeV	16
peak current	mA	100
repetition rate	Hz	300
absolute energy spread	MeV	25%
macro pulse length	ns	>50
RF Frequency	MHz	2856
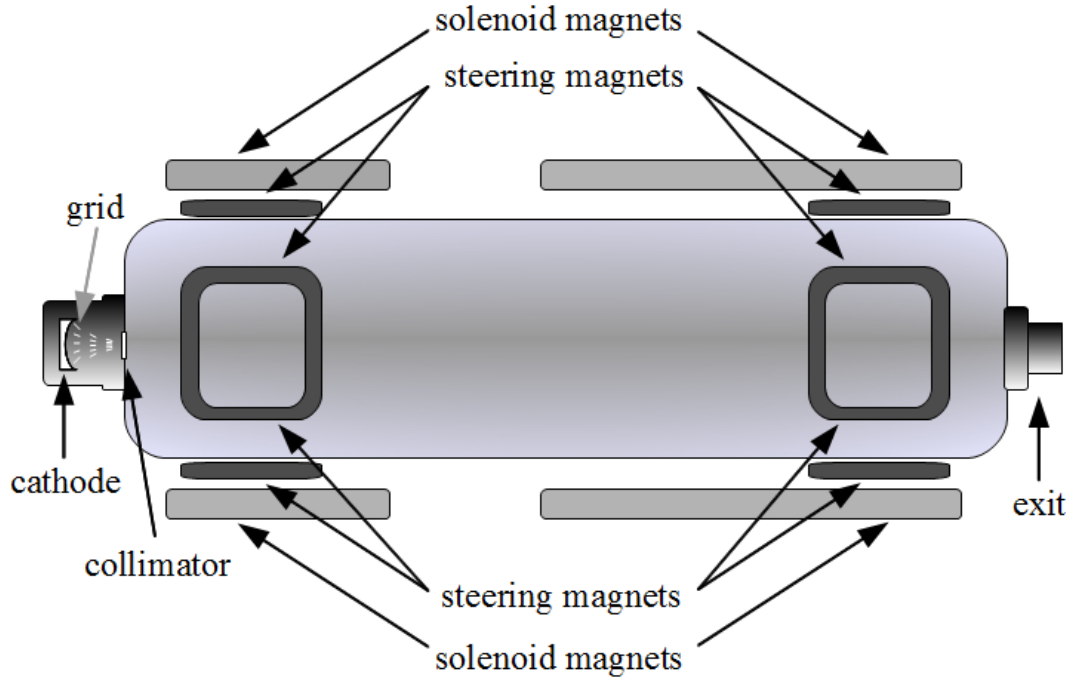
Figure 2.1: Adjustable elements within the HRRL cavity.

Table 2.2: The HRRL Beamline Parts and Coordinates.

Label	Beamline Element	Distance from Linac Exit (mm)
Q1	quadrupole	335
Q2	quadrupole	575
Q3	quadrupole	813
T1	e^+ production target	1204
Q4	quadrupole	1763
Q5	quadrupole	2013
Q6	quadrupole	2250
D1	dipole	2680
S1	OTR screen	3570
FC1	Faraday cup	3740
EnS	energy slit	3050
S2	YAG screen	3410
Q7	quadrupole	3275
D2	dipole	3842
FC2	Faraday cup	4142
Q8	quadrupole	4044
Q9	quadrupole	4281
Q10	quadrupole	4571
T2	annihilation target	7381

Faraday cups and toroids were installed to measure the electron beam current. Energy slits were installed to control the energy/momentum spread of the beam after the first dipole (D1).

A 1.016 mm thick retractable tungsten (99.95%) foil target (T1) was placed between the 1st and 2nd quadrupole triplets and used to produce positrons when the electron beam interacts with it. The room where the HRRL is located is divided by a wall into two parts; the accelerator side and the experimental cell. A beam pipe at the end of the 90 degree beamline goes through a hole in the wall and delivers the beam from the accelerator side to the experimental cell. The positron detection system consisting of two NaI detectors was placed at the end of the beamline in the experimental cell side as shown in Figure 2.2.

The positron production target, T1 was shielded with 8 inches of Fe bricks and 4 inches of Pb bricks to lower photon and electron background. The two dipoles were

Figure 2.2: The HRRL beamline layout.

also shielded with Pb bricks because the beam scrapes the dipole vacuum chamber when it is transported. An eight inch thick Pb wall was installed on both sides of the wall dividing the accelerator and the experimental cell to shield the cell from background generated on the accelerator side. The NaI detectors were shielded with Pb brick as well to lower background. Positioning the NaI detector in a separate room from the positron production target T1 was done to decrease the high background that is historically present in the accelerator room. While this choice reduces the background there is also substantial signal loss, as will be shown in subsequent chapters, transporting a chromatic positron sample to the experimental cell.

2.2 HRRL Beamline Alignment Using Laser

The HRRL beamline was aligned using a laser beam as shown in Figure 2.3. The HRRL electron gun was removed so that the laser beam from a laser placed on a table in the experimental side of the HRRL cell would be directed through the cavity. Mirrors were mounted onto holders with horizontal and vertical adjustments. The laser was first adjusted with two mirrors on the laser table and focused using two focusing lenses. Two mirrors, one on the experimental side and one on the linac side, reflected the laser beam through the center of the linac.

The laser beam was shot through the center of the HRRL cavity and the geometrical center of the 0 degree beamline magnets (quadrupoles Q1∼Q6, first dipole D1) downstream were aligned according to the laser beam. The laser beam was reflected by a mirror mounted on a rotator that reflected the beam by 90° to the 90 degree beamline and the quadrupole magnets in the 90 degree beamline were aligned relative to the laser beam reference point.

Two irises were placed at the end of the 90 degree beamline and centered on the reflected 90 degree laser beam. A second laser was mounted on the wall in the experimental cell side. The laser on the wall was positioned to pass through the center of the two irises placed at the end of the 90 degree beamline. Thus, the laser on the wall was aligned to the center of the 90 degree beamline and can be used as

Figure 2.3: HRRL beamline alignment using laser.
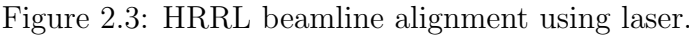
a reference as shown in Figure 2.4.
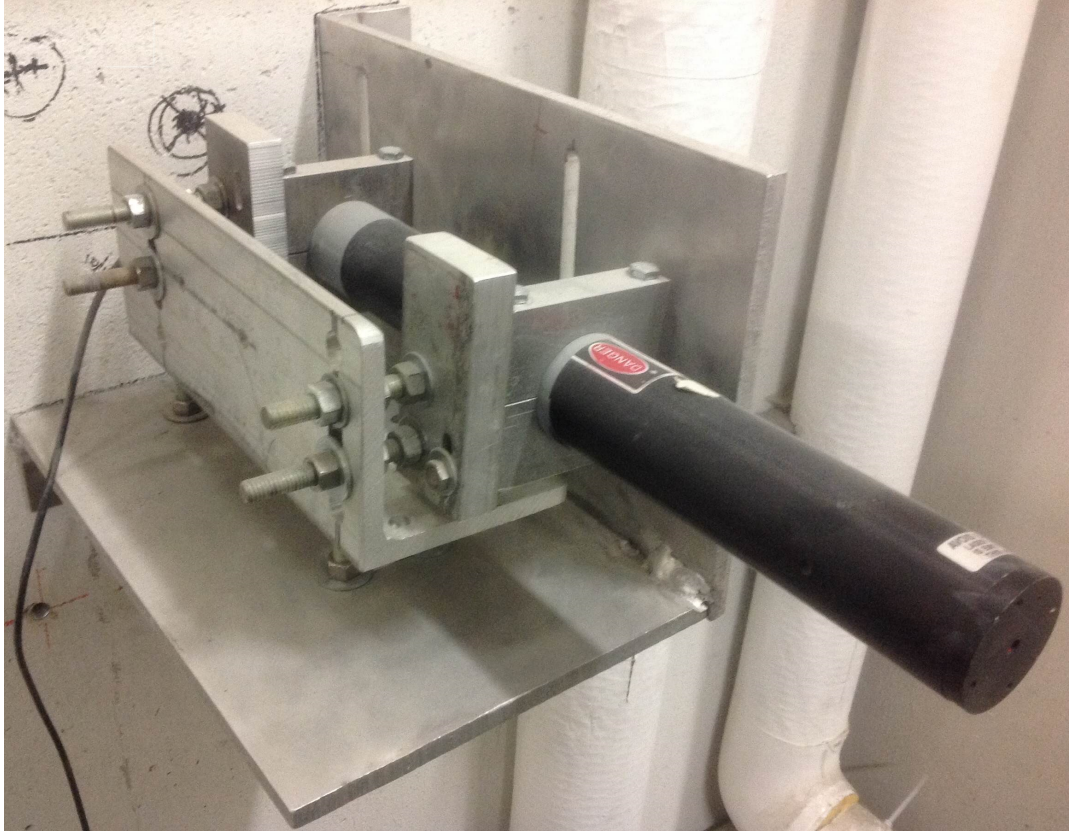
Figure 2.4: The laser mounted on the experimental cell side wall. This laser was aligned to the center of the 90 degree beamline.

At last, the second dipole, D2, was connected to the 90 degree beampipe and beamline elements between D1 and D2 (energy slits, Q7, and 5-way cross holds YAG screen) were placed one after another.

2.3   Energy Slit and Flag Controller

A control box was built to open and close the energy slit as well as control the three flags shown in Figure 2.5. The slit control is on the right side of the box and the maximum width of the slit is 3.47 cm as shown in Figure 2.5. On the left of the controller are the switches for three flags. Power supplies were installed inside the box and controlled by these switches to remove the targets from the beamline, turn on/off the cameras of the flags, and turn on/off the lights within each flag.

2.3.1 Energy Slit Controller

The controller was built to adjust the energy slit width (Danfysik water cooled slit model 563 system 5000) based on the design from Danfysik [14] as shown in Figure 2.5 (on right side). The wiring diagram of the controller is shown in Figure 2.6. When the energy slit is fully open, the width between slits is 3.47 cm as indicated by the LED number display. When the slit is fully open/closed, one of the two LED lights will light up and the motor will stop.

The power source of the energy slit provides 12 VDC, 1.8 A max current, 20 W power, and takes 85∼264 VAC input. The motor and the relay switch require 12 VDC. The LED indicating lights require 12 V/50 mA current and the 57 Ω resistors have a power rating of 0.5 W.

A potentiometer is placed inside the energy slit controller and the resistance of the potentiometer determines the width of the slit. A 370 mV voltage is applied to the potentiometer. An LED number display is connected to the potentiometer so that the voltage change in the potentiometer is numerically indicated by the LED display. The slit width is indicated by the potentiometer resistance in the circuit. The potentiometer resistance in the circuit is indicated by the voltage across the resistor in the circuit which is displayed on the LED number display. For example, when the width of the energy slit is 3.24 cm, the voltage on the potentiometer read by the LED display is 324 mV, and the LED number display indicates 3.24. The cm unit is labeled on the right of LED display.
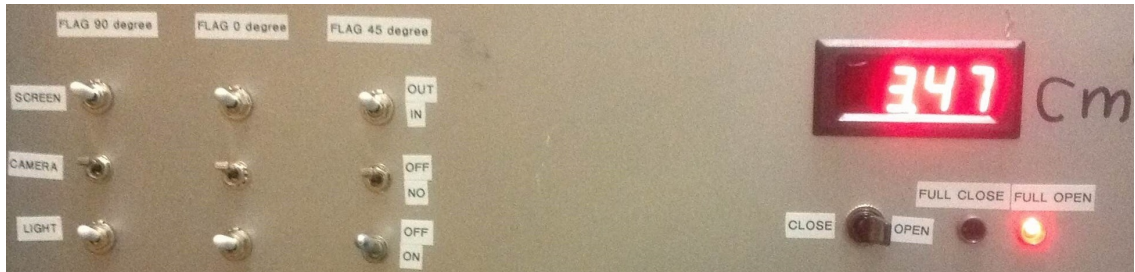
Figure 2.5: Front panel of the energy slit controller (on the right) and flag controllers (on the left).

Figure 2.6: Energy slit controller wiring diagram (modified from the design given in the Danfysik water cooled slit model 563 system 5000 manual) [14].

2.3.2 Flag Controller

On the left of the controller box are the switches for three flags (0 degree/OTR flag, 45 degree/YAG flag, and 90 degree/annihilation target flag) as shown in Figure 2.5. Four power supplies (one back up) were installed inside the box and controlled by these switches. The switches in the top row insert or remove the targets from the beamline and the ones in the middle turn the flag cameras on and off. The bottom row switches turn on/off the lights of the flag which lights up the target.

2.4 The OTR Imaging System

The OTR target is a 10 μm thick aluminum foil with a 1.25 inch diameter. A moving charged particle produces electromagnetic fields that are dependent on the dielectric constant of the media the particle traverses. When a moving charged particle crosses the boundary between two media (vacuum and aluminum in this case), electromagnetic radiation is emitted to reorganize the fields in the new media. The radiation is emitted in both forward (beam direction) and backward (image charge direction) as shown in Figure 2.7.

Three two inch diameter lenses were used for the imaging system to avoid optical distortion at lower electron energies. The focal lengths and positions of the lenses, shown in Figure 2.8, were calculated with the thin lens equation to produce the desired image magnification. The lenses, assembly rods, and lens holder plates for the camera cage system were purchased from Thorlabs, Inc. [16].

The camera used is a JAI CV-A10GE digital 1/2" progressive scan camera with a 767 (horizontal) by 576 (vertical) pixel area and 6.49 (horizontal) by 4.83 (vertical) mm sensing area. It has high speed shutter from 1/60 to 1/300,000 second, edge pre-select, pulse width trigger modes, auto shutter, and smear-less mode. The images were taken by triggering the camera (in edge pre-select mode) synchronously with the electron gun.
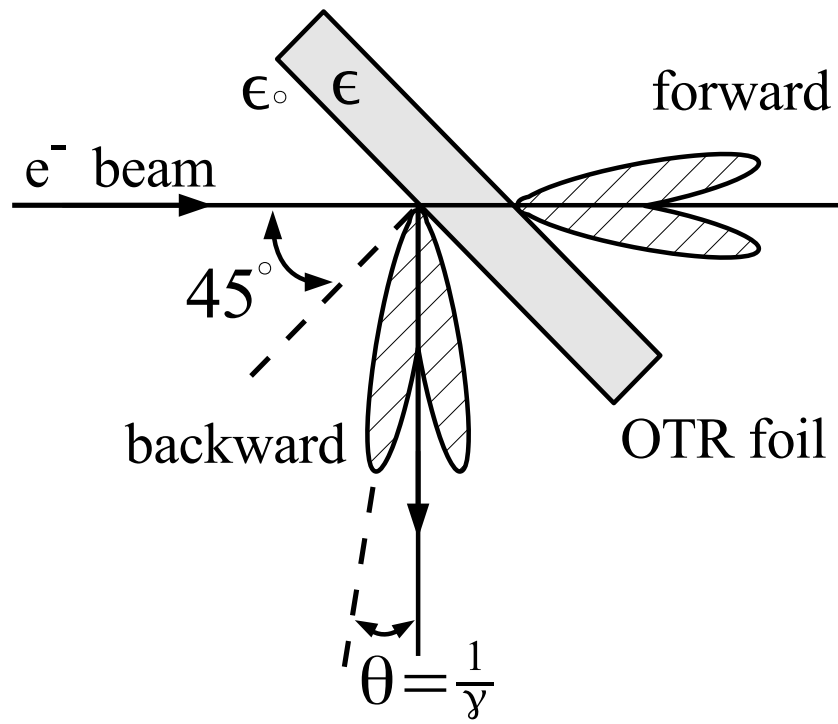
Figure 2.7: OTR pattern when the incident beam is at a 45° angle with respect to the foil [15].

OTR screen

17 cm

$\theta = \dfrac{1}{\gamma}$

f = 10 cm

2"

18 cm

f = 50 cm

4 cm

f = 5 cm

4 cm

camera
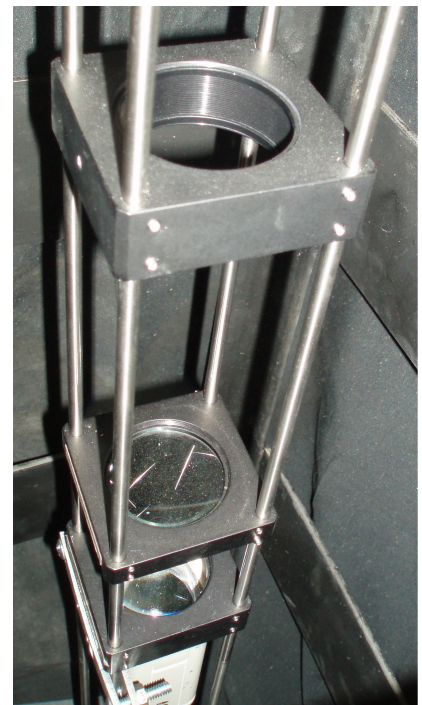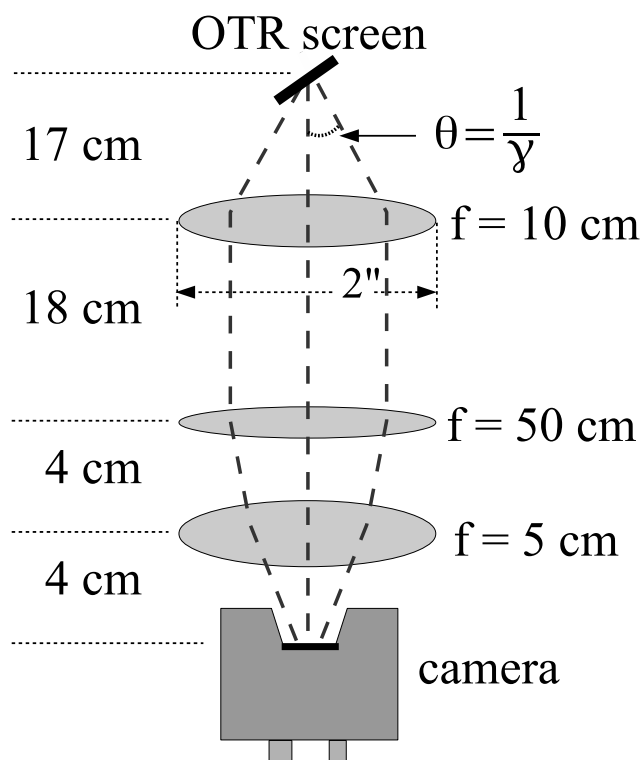
Figure 2.8: The OTR imaging system.

2.5   Positron Detection

When the electron beam is incident on T1, photons and secondary electrons are created along with positrons. These particles are the main source of noise in the experiment. The positrons were transported to the second tungsten target (T2) which was shielded from this background by the concrete wall and Pb bricks. The setup is shown in Figure 2.9. A 6-way cross was placed at the end of the beamline to hold T2. The 6-way cross has three 1 mil (0.0254 millimeters) thick stainless steel windows. The two horizontal windows perpendicular to the beamline allowed the 511 keV photons created from the positron annihilation to escape the beamline with limited attenuation. A third window at the end of the 90 degree beamline was used as the beam exit. Two NaI detectors were placed facing the two exit windows to detect the photons produced in T2. A 2 inch thick lead brick collimator with a 2 inch diameter hole was placed between the exit window and NaI detector. A scintillator (Scint) and a Faraday cup (FC3) were placed at the end of the beamline and were used to tune the electron and positron beam. When positrons reach T2, they can thermalise and annihilate inside T2. During thermalization, a positron looses its kinetic energy. When it annihilates with an electron, two 511 keV photons are emitted back to back. A triplet coincidence was required between the accelerator RF pulse and the detection of a photon in each NaI detector.

2.5.1   NaI Detectors

NaI crystals, shown in Figure 2.10, were used to detect 511 keV photons from positron annihilation. Originally, the detectors had signal pulse lengths around 400 μs. New PMT bases were built to use the HV divider shown in Figure 2.11. A picture of the constructed bases is shown in Figure 2.12. The pulse length of the new PMT base is about 1 μs. The NaI crystal is from Saint-Gobain Crystal & Detectors (Mod. 3M3/3) with a dimension of $3'' \times 3''$. Operating high voltage of -1150 V would position the 511 keV photons within the range of the charge sensing ADC (CAEN Mod. V792).
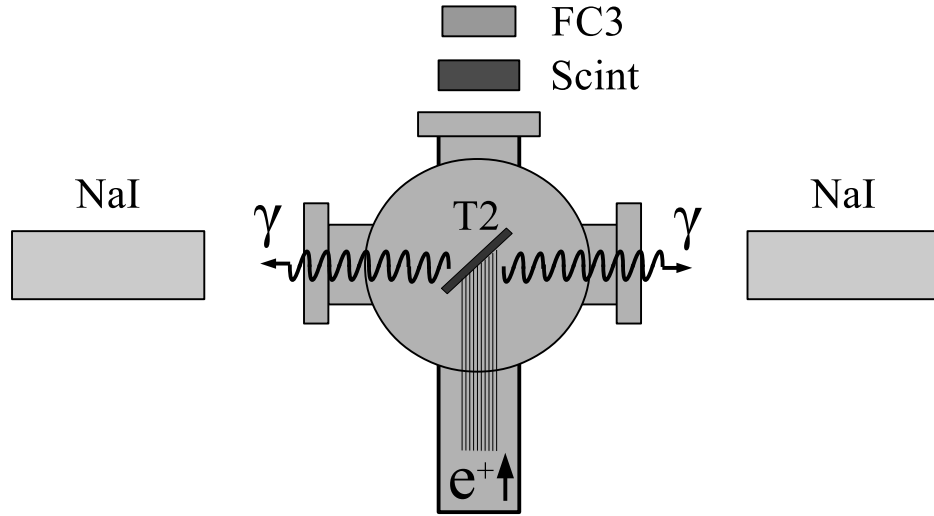
Figure 2.9: The positron detection system: T2 was placed at 45° with respect to the horizontal plane first, then rotated 45° along the vertical axis.

Table 2.3: The Radioactive Sources and Corresponding Photon Peaks.

Radioactive Sources	Unit	First Peak	Second Peak
Co-60	keV	1173	1332
Na-22	keV	511	1275
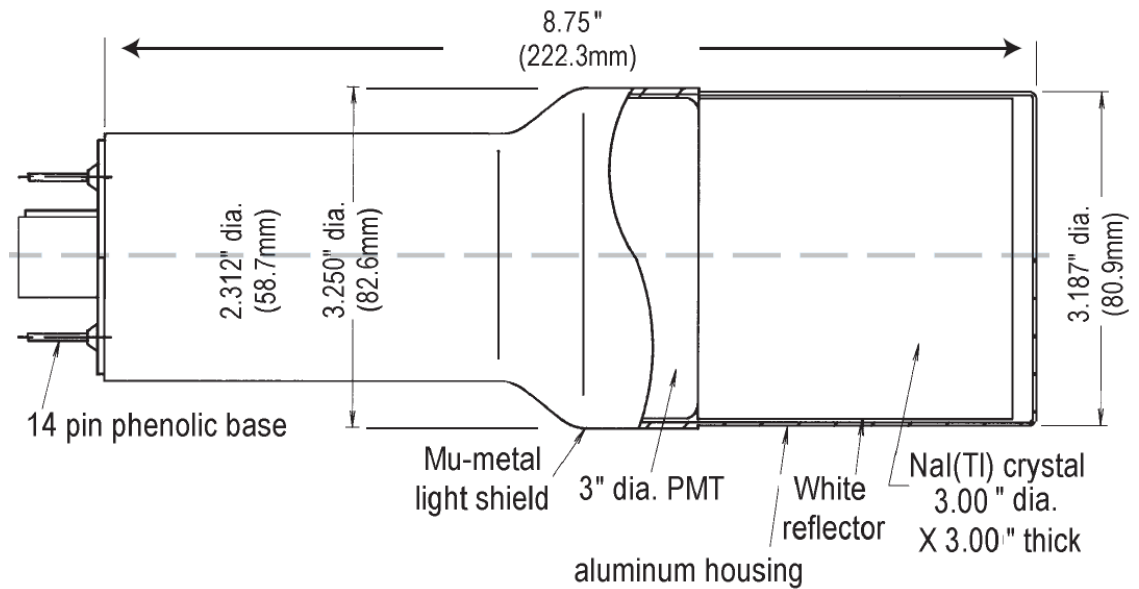
Figure 2.10: The NaI crystal dimension.
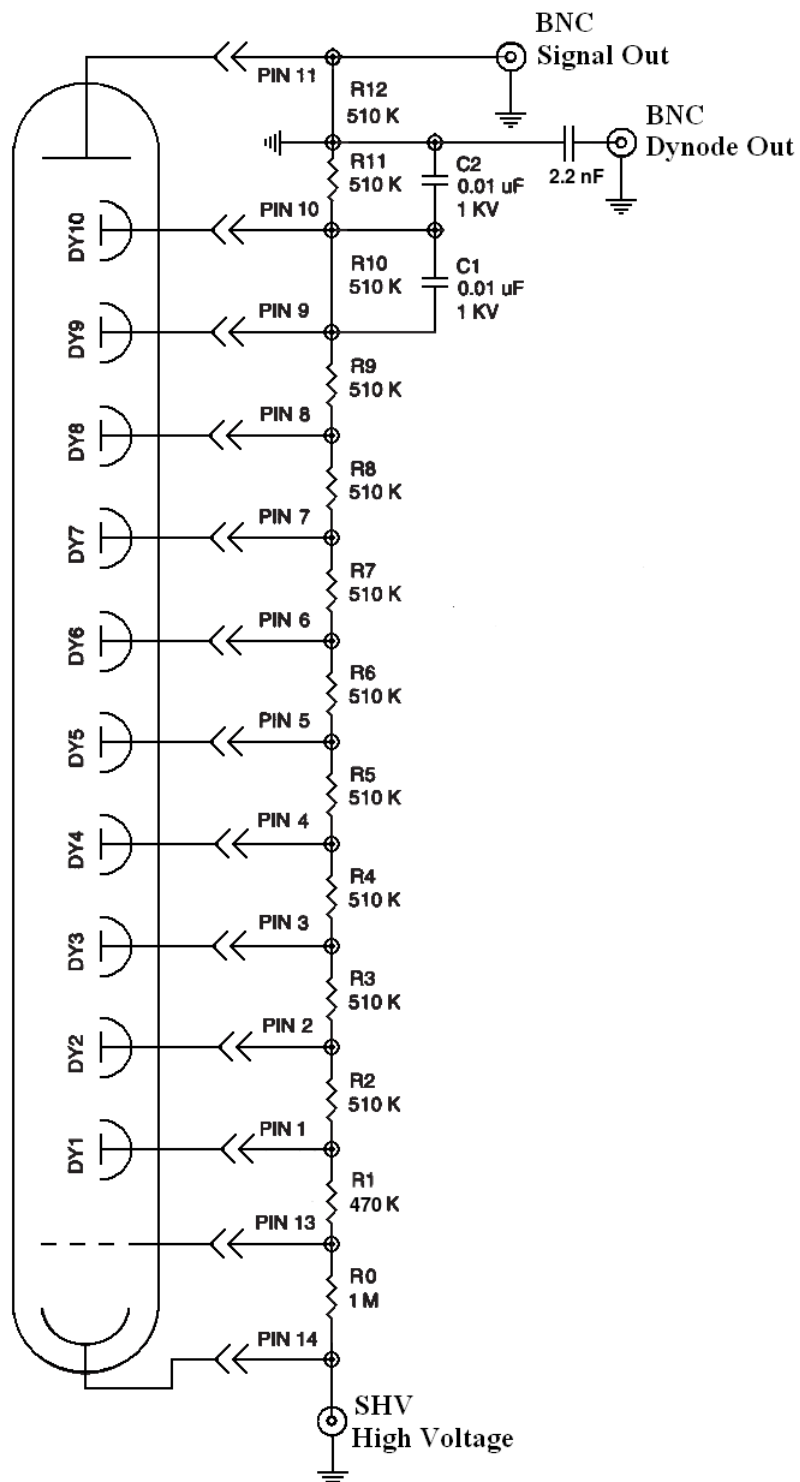
Figure 2.11: The modified PMT base design.
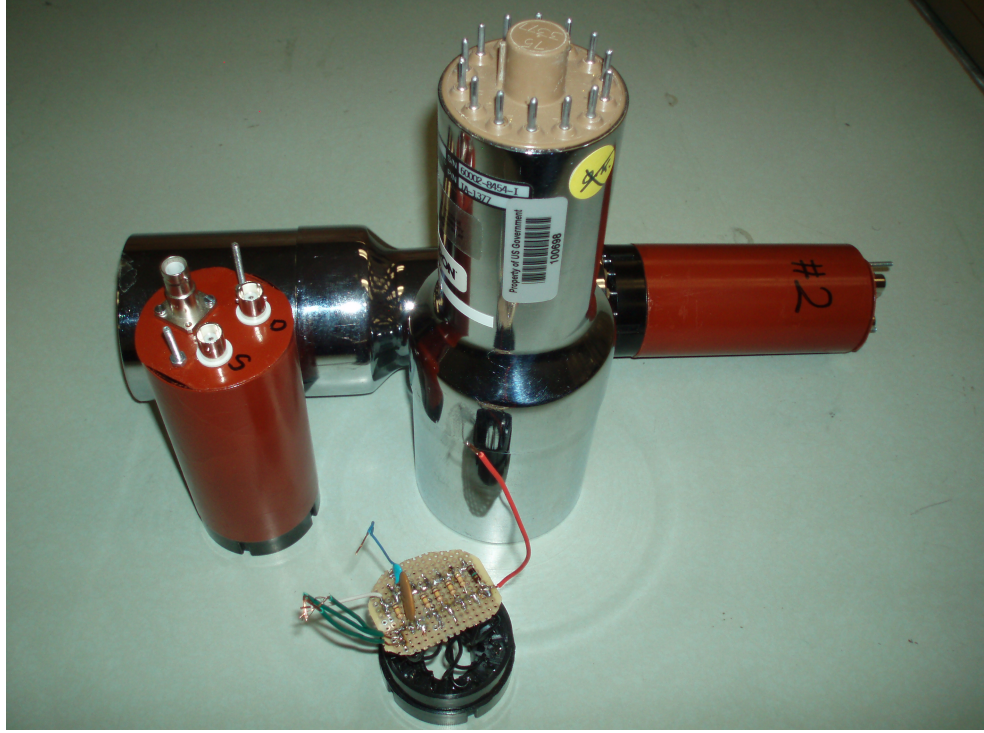
Figure 2.12: The NaI crystals and new bases.

The NaI detectors were calibrated using a Na-22 and a Co-60 source with the photon peaks indicated in Table 2.3. Figure 2.13 is the oscilloscope image of several Co-60 photon pulses observed by the detector with the new PMT. The calibrated NaI detector spectrum from the Na-22 and Co-60 sources is shown in Figure 2.14. The rms values of the fits on the four peaks shown in Figure 2.14 are $\sigma_{Na,511} = 18.28 \pm 0.04$ keV, $\sigma_{Na,1275} = 44.51 \pm 0.27$ keV, $\sigma_{Co,1173} = 42.49 \pm 0.24$ keV, and $\sigma_{Co,1332} = 50.30 \pm 0.39$ keV.

2.5.2 The DAQ Setup

The data acquisition (DAQ) setup and timing diagram is shown in Figure 2.15. The last dynode signals from the left and right NaI detectors were inverted using an ORTEC 474 inverting amplifier and sent to a CAEN Mod. N842 constant fraction discriminator (CFD). The electron gun pulse from the linac was used to generate a VETO for the CFD to prevent the RF noise from triggering the CFD, otherwise the
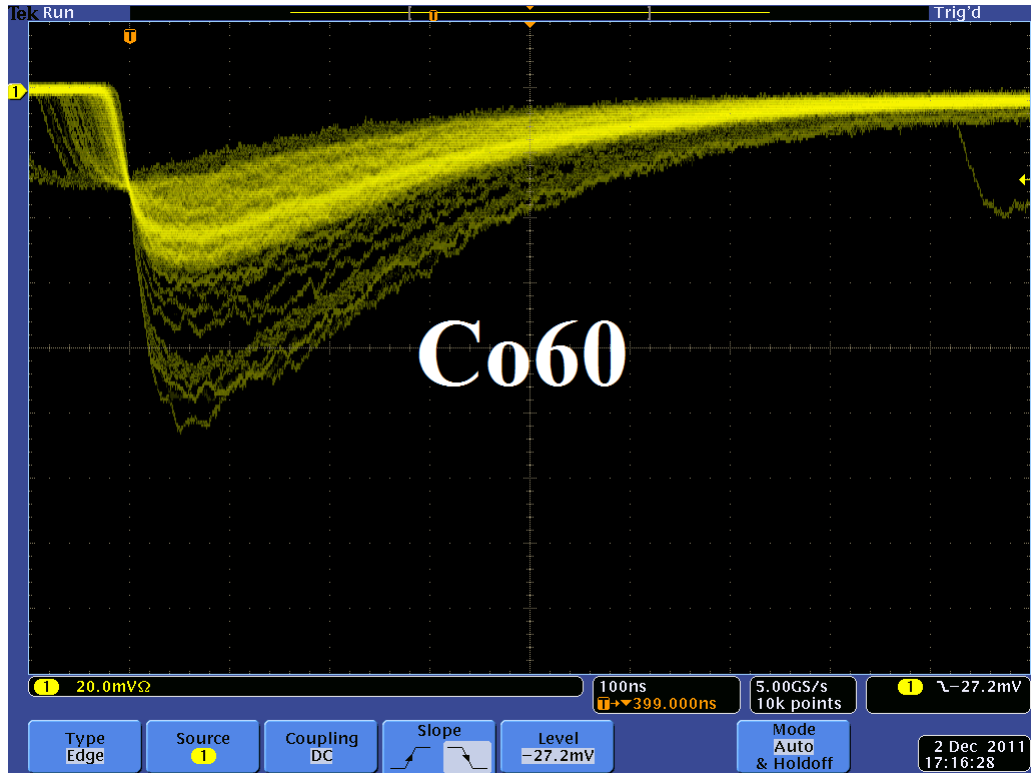
Figure 2.13: Detector output pulses using the Co-60 source and new PMT. The amplitude of the pulse is about 60 mV. The rise time of the pulse is longer than 50 ns, and the fall time is longer than 700 ns.
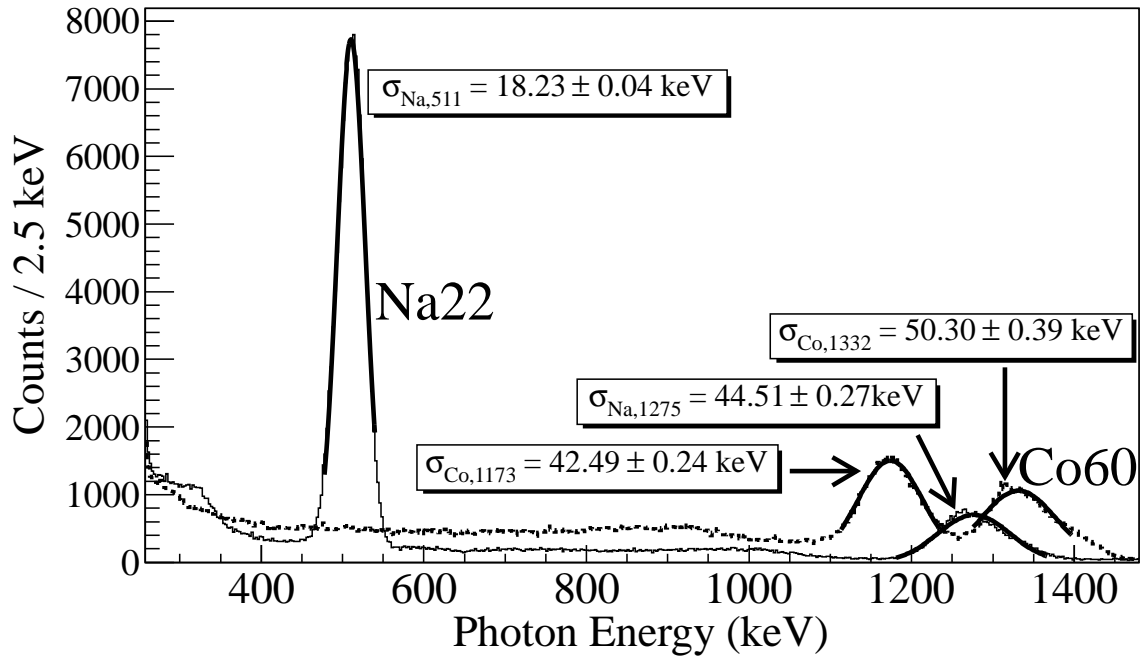
Figure 2.14: The calibrated NaI spectrum of Na-22 and Co-60 sources.

CFD would generate multiple digital pulses. The PMT output itself could produce multiple CFD output pulses due to the voltage fluctuations within a single pulse. To prevent multiple CFD outputs, a GG 8000-01 octal gate generator was used to create a single 1 μs wide pulse from the CFD's first pulse in order to ignore the multiple CFD pulses produced by a single analog output pulse from the detector. A triple coincidence was formed between the gun pulse and the 1 μs wide pulse from each detector using a LeCroy model 622 logic module.

The ADC requires 5.7 μs to convert the analog signal to a digital signal. The logic module output was delayed 6 μs by a dual timer (CAEN Mod. N93B) to accommodate the ADC's conversion time and trigger the DAQ. The ADC (CAEN Mod. V792) converted the NaI detector's analog signals to digital when a 1 μs gate, created by the gun pulse using a dual timer, was present as shown in the lower part of Figure 2.15. The ADC was fast cleared unless it received a veto signal from the inverted output of logic module created using a dual timer.

Figure 2.15: The DAQ setup and timing diagram.

Chapter 3

Data Analysis

In the first section of this chapter, the measurement of the HRRL emittance and Twiss parameters using the quadrupole scanning method is described. The current in the first quadrupole, Q1, was changed incrementally and the electron beam shapes were observed using the OTR screen located at the end of the 0 degree beamline. The emittance and Twiss parameters are obtained by fitting a parabolic function to the plot $\sigma_{x,y}^2$ vs K_1L (K_1 is quadrupole strength and L is the quadrupole effective length).

The second section describes the energy distribution measurement of the HRRL when it was tuned to generate an electron beam with its peak at 12 MeV. A Faraday cup, FC2, was placed at the end of the 45 degree beamline to measure the electron beam current when D1 was on and D2 was off. The energy scan data and the MATLAB script used for data analysis are given in the Appendix A.

Last section reports the positron production efficiency using the HRRL located in the Beam Lab of Physics Department. The 12 MeV electron beam from the HRRL, when incident on the tungsten production target (T1), produced positrons that were transported to the annihilation target (T2) where they annihilated and created back to back 511 keV photon pairs. Two NaI detectors, their shielding, placement, and operation modes are described. The different methods to count positron rates are discussed. The electron beam current of the HRRL during the positron production was monitored by a scintillator. The calibration of the scintillator using a Faraday cup and oscilloscope is described. At last, the ratios of positrons detected using NaI detectors in coincidence mode to the electrons impinging on T1 are given for 1∼5 MeV positron beam.

3.1 Emittance Measurement

The HRRL beam emittance was measured by using an optical transition radiation (OTR) screen. This transition radiation was theoretically predicted by Ginzburg and Frank [9] in 1946 to occur when a charged particle passes the boundary of two media. An OTR based viewer (31.75 mm in diameter and 10 μm thick aluminum foil) was installed to observe the electron beam size at 37.2 mA (higher currents might saturate the camera) electron peak currents, available using the HRRL at 15 ± 1.5 MeV with 200 ns macro pulse width. Visible light is produced when a relativistic electron beam crosses the boundary of two media (aluminum and air) with different dielectric constants.

Light is emitted in a conical shape at backward angles with the peak intensity at an apex angle of $\theta = 1/\gamma$ (γ is relativistic factor) with respect to the incident electron's angle of reflection. A 15 MeV electron accelerated by the HRRL would emit light at $\theta = 2°$. Orienting the OTR target at 45° with respect to the incident electron beam will result in the high intensity photons being observed at an angle of 90° with respect to the incident beam, see Figure 3.1. These backward-emitted photons are observed using a digital camera and can be used to measure the shape and the intensity of the electron beam. Although an emittance measurement can be performed in several ways [10, 11], the quadrupole scanning method [12] was used to measure the emittance and Twiss parameters in this work.

3.1.1 Emittance Measurement Using Quadrupole Scanning Method

Figure 3.1 illustrates the beamline components used to measure the emittance with the quadrupole scanning method. A quadrupole is positioned at the exit of the linac to focus or de-focus the beam as observed on the OTR view screen. The 3.1 m distance between the quadrupole and the screen was chosen in order to minimize chromatic effects and to satisfy the thin lens approximation. Assuming the thin
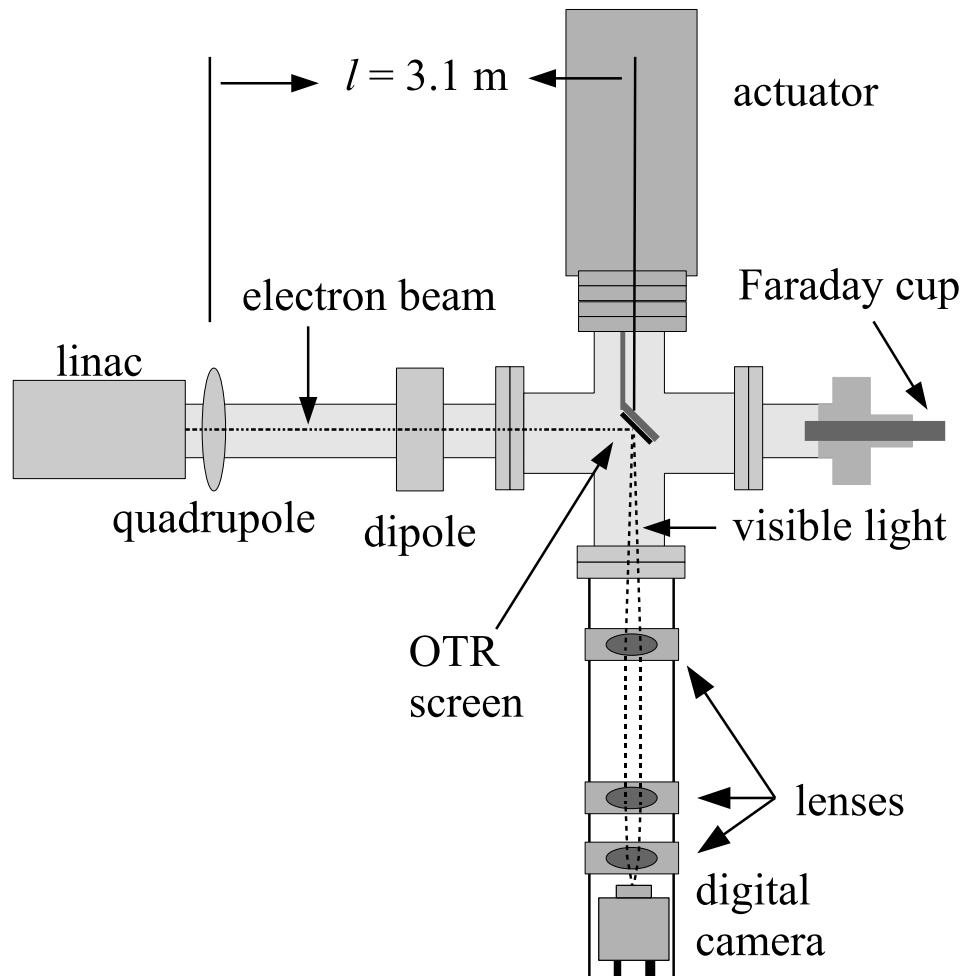
Figure 3.1: Apparatus used to measure the beam emittance.

lens approximation, $\sqrt{k_1}L << 1$, is satisfied, the horizontal transfer matrix of a quadrupole magnet may be expressed as

$$\mathbf{Q} = \begin{pmatrix} 1 & 0 \\ -k_1 L & 1 \end{pmatrix} = \begin{pmatrix} 1 & 0 \\ -\frac{1}{f} & 1 \end{pmatrix}, \tag{3.1}$$

where L is the length of quadrupole and f is the focal length. k_1 is the quadrupole strength given by

$$k_1 = 0.2998 \frac{g(\mathrm{T/m})}{p(\mathrm{GeV/c})} = 0.2998 \frac{\frac{B(I(\mathrm{A}))}{R_q}}{p(\mathrm{GeV/c})}, \tag{3.2}$$

where g is the gradient of the quadrupole with the Bore aperture radius R_q at a given coil current I and p is the momentum of the electron beam. A matrix representing the drift space between the quadrupole and screen is given by

$$\mathbf{S} = \begin{pmatrix} 1 & l \\ 0 & 1 \end{pmatrix}, \tag{3.3}$$

where l is the distance between the scanning quadrupole and the screen. The transfer matrix $\mathbf{M}$ of the scanning region is given by the matrix product $\mathbf{SQ}$. In the horizontal plane, the beam matrix at the screen ($\sigma_\mathbf{s}$) is related to the beam matrix of the quadrupole ($\sigma_\mathbf{q}$) using the similarity transformation

$$\sigma_\mathbf{s} = \mathbf{M}\sigma_\mathbf{q}\mathbf{M}^\mathrm{T}. \tag{3.4}$$

where the $\sigma_\mathbf{s}$ and $\sigma_\mathbf{q}$ are defined as [13]

$$\sigma_{\mathbf{s},x} = \begin{pmatrix} \sigma_{\mathrm{s},x}^2 & \sigma_{\mathrm{s},xx'} \\ \sigma_{\mathrm{s},xx'} & \sigma_{\mathrm{s},x'}^2 \end{pmatrix}, \; \sigma_{\mathbf{q},x} = \begin{pmatrix} \sigma_{\mathrm{q},x}^2 & \sigma_{\mathrm{q},xx'} \\ \sigma_{\mathrm{q},xx'} & \sigma_{\mathrm{q},x'}^2 \end{pmatrix}. \tag{3.5}$$

By defining the new parameters [12]

$$A \equiv l^2 \sigma_{\mathrm{q},x}^2, \ B \equiv \frac{1}{l} + \frac{\sigma_{\mathrm{q},xx'}}{\sigma_{\mathrm{q},x}^2}, \ \text{and} \ C \equiv l^2 \frac{\epsilon_x^2}{\sigma_{\mathrm{q},x}^2}, \tag{3.6}$$

the matrix element $\sigma_{\mathrm{s},x}^2$, the square of the beam size's rms at the screen, may be expressed as a parabolic function of the product of k_1 and L

$$\sigma_{\mathrm{s},x}^2 = A(k_1 L)^2 - 2AB(k_1 L) + (C + AB^2). \tag{3.7}$$

The emittance measurement was performed by changing the quadrupole current, which changes $k_1 L$, and measuring the corresponding beam image size on the view screen. The measured two-dimensional beam image was projected along the image's abscissa and ordinate axes. A super Gaussian fitting function is used on each projection to determine the rms value, σ_{s} in Eq. (3.7). Measurements of σ_{s} for several quadrupole currents ($k_1 L$) are then fit using the parabolic function in Eq. (3.7) to determine the constants A, B, and C. The unnormalized projected rms emittance (ϵ) and the Twiss parameters (α and β) can be found using Eq. (3.8)

$$\epsilon = \frac{\sqrt{AC}}{l^2}, \ \beta = \sqrt{\frac{A}{C}}, \ \alpha = \sqrt{\frac{A}{C}} \left(B + \frac{1}{l} \right). \tag{3.8}$$

3.1.2 HRRL Emittance Measurement Experiment

A quadrupole scanning method was used to measure the accelerator's emittance. The quadrupole current is changed to alter the strength and direction of the quadrupole magnetic field such that a measurable change in the beam shape is seen by the OTR system. Initially, the beam was steered by the quadrupole indicating that the beam was not entering along the quadrupole's central axis. Several magnetic elements upstream of this quadrupole were adjusted to align the incident electron beam with the quadrupole's central axis. First, the beam current observed by a Faraday cup located at the end of beam line was maximized using upstream steering coils within the linac nearest the gun. Second, the first solenoid nearest the

linac gun was used to focus the electron beam on the OTR screen. Steering coils were adjusted to maximize the beam current to the Faraday cup and minimize the deflection of the beam by the quadrupole. A second solenoid and the last steering magnet shown in Figure 2.1, both near the exit of the linac, were used in the final step to optimize the beam spot size on the OTR target and maximize the Faraday cup current. A configuration was found that minimized the electron beam deflection when the quadrupole current was altered during the emittance measurements.

The emittance measurement was performed using an electron beam energy of 15 MeV and a 200 ns long macro pulse of 40 mA electron current. The current in the first quadrupole after the exit of the linac was changed from -5 A to $+5$ A with an increment of 0.2 A. Seven measurements were taken at each current step in order to determine the average beam width and the variance. Background measurements were taken by turning the linac's electron gun off while keep the RF on. OTR images of the beam are shown in Figure 3.2. The digitized OTR images before and after background subtraction are shown in Figure 3.3. A small dark current is visible in Figure 3.3 (b) that is known to be generated when electrons are pulled off the cavity wall and accelerated.

The electron beam energy was measured using a dipole magnet downstream of the quadrupole used for the emittance measurements. Prior to energizing the dipole, the electron micro-pulse bunch charge passing through the dipole was measured using a Faraday cup located approximately 50 cm downstream of the OTR screen. The dipole current was adjusted until a maximum beam current was observed on another Faraday cup located just after the 45 degree exit port of the dipole. A magnetic field map of the dipole indicates that the electron beam energy was 15 ± 1.6 MeV.

Images from the JAI camera were calibrated using the OTR target frame. An LED was used to illuminate the OTR aluminum frame that has a known inner diameter of 31.75 mm. Image processing software was used to inscribe a circle on the image to measure the circular OTR inner frame in units of pixels. The scaling factor can be obtained by dividing this length with the number of pixels observed. The result is a horizontal scaling factor of 0.04327 ± 0.00016 mm/pixel and vertical

Figure 3.2: The 15 MeV electron beam observed using the OTR screen when the dipole coil current was at 0. The macro pulse was 200 ns and the electron peak current was 40 mA .

scaling factor of 0.04204 ± 0.00018 mm/pixel. Digital images from the JAI camera were extracted in a matrix format in order to take projections on both axes and perform a Gaussian fit. The observed image profiles were not well described by a single Gaussian distribution.

The profiles may be described using a Lorentzian distribution, however, the rms of the Lorentzian function is not defined. A super Gaussian distribution was used [20], because it has a sharper distribution than Gaussian and, unlike Lorentzian, the rms values may be directly extracted. The super Gaussian reduced the Chi-square per degree of freedom by a factor of ten compared to a typical Gaussian fit. The beam spot, beam projections, and fits are shown in Figure 3.4. In a typical Gaussian distribution, $\phi(x) = \frac{1}{\sqrt{2\pi}}e^{-\frac{1}{2}x^2}$, the independent variable x is raised to the 2nd power while in the super Gaussian it is raised to a power smaller than 2. For example, the beam projections shown in Figure 3.4 were fit with the super Gaussian distributions. The variable x on the exponent was raised to 0.9053 (x-projection) and 1.0427 (y-
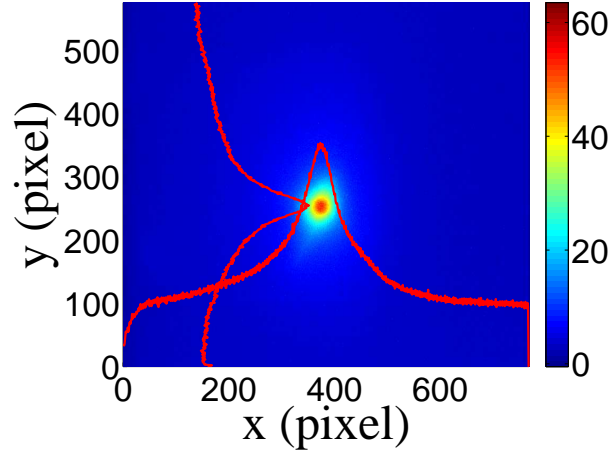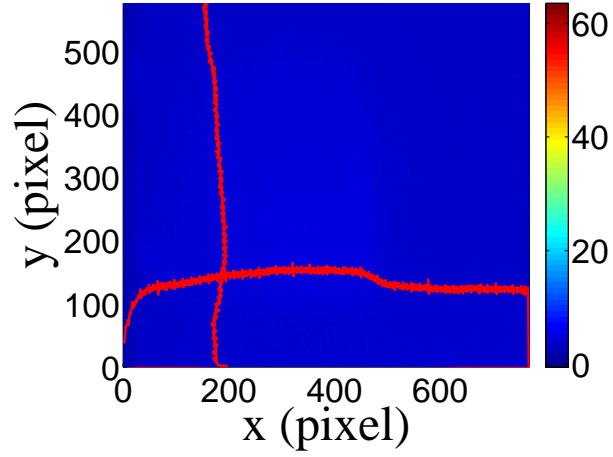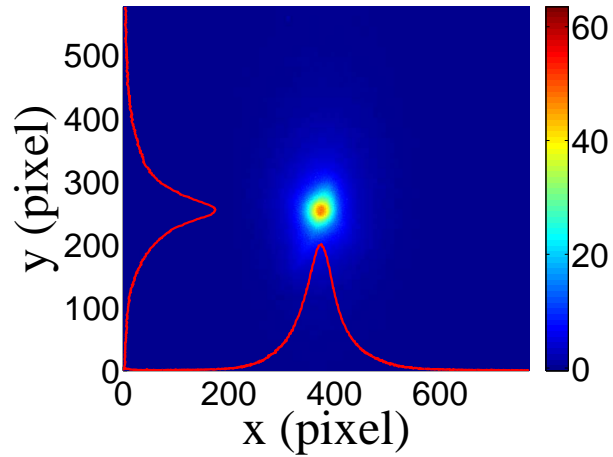
Figure 3.3: Digital image from the OTR screen; (a) an image taken with the beam on, (b) a background image taken with the RF on but the electron gun off, (c) The background subtracted beam image ((a)-(b)).

projection).
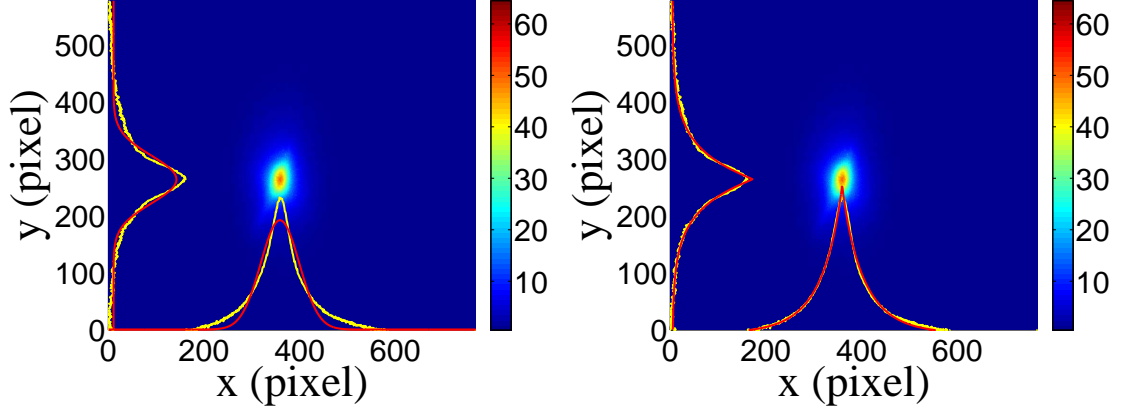
Figure 3.4: Gaussian and super Gaussian fits for the horizontal and vertical beam projections. The beam images is background subtracted image and taken when quadrupole magnets are turned off. Left image is Gaussian fit and right image is super Gaussian fit.

Figure 3.5 shows the square of the rms (σ_{s}^2) vs $k_1 L$ for x (horizontal) and y (vertical) beam projections along with the parabolic fits using Eq. 3.5. The emittance and Twiss parameters from these fits are summarized in Table 3.1. The MATLAB [21] scripts used to calculate emittance and Twiss parameters are given in appendix B.
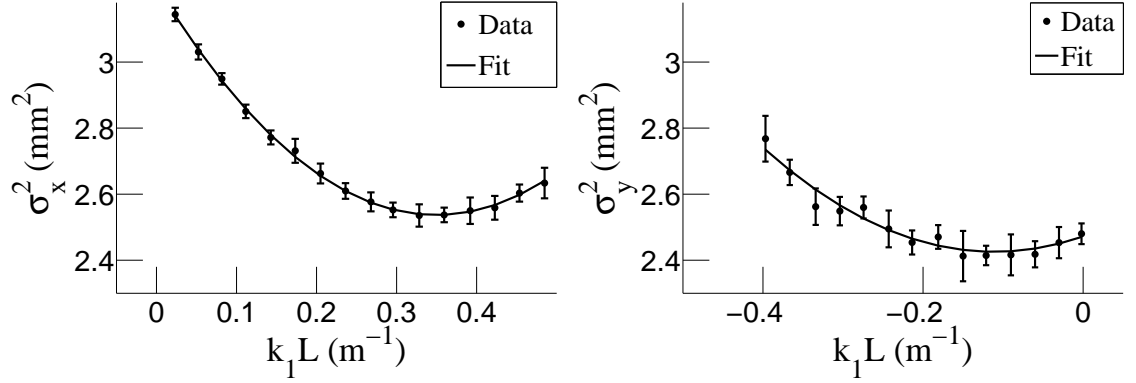
Figure 3.5: Beam profile measurements for an emittance measurement. As the quadrupole current changes, so does quadrupole strength times quadrupole length, $k_1 L$, and the square of the beam rms changes accordingly.

Table 3.1: Emittance Measurement Results

Parameter	Unit	Value
unpolarized projected emittance ϵ_x	μm	0.37 ± 0.02
unpolarized projected emittance ϵ_y	μm	0.30 ± 0.04
β_x-function	m	1.40 ± 0.06
β_y-function	m	1.17 ± 0.13
α_x-function	rad	0.97 ± 0.06
α_y-function	rad	0.24 ± 0.07
micro-pulse charge	pC	11
micro-pulse length	ps	35
energy of the beam E	MeV	15 ± 1.6
relative energy spread $\Delta E/E$	%	10.4

3.2 Measurement of HRRL Electron Beam Energy Spread at 12 MeV

The HRRL energy profile was measured when it was tuned to accelerate electrons to a peak energy of 12 MeV. A Faraday cup, FC2, was placed at the end of the 45 degree beamline to measure the electron beam current when D1 was on and D2 was off. The dipole coil current for D1 was changed in 1 A increments. As the dipole coil current was changed, the energy of the electrons transported to the Faraday cup would change as described in Appendix A. Figure 3.6 illustrates a measurement of the 12 MeV peak illustrating the observed low energy tail. The HRRL energy profile can be described by overlapping two skewed Gaussian fits [20]. The fit function is given by

$$G(En) = A_1 e^{\frac{-(En-\mu_1)^2}{2\{\sigma_1[1+sgn(En-\mu_1)]\}^2}} + A_2 e^{\frac{-(En-\mu_2)^2}{2\{\sigma_2[1+sgn(En-\mu_2)]\}^2}}, \qquad (3.9)$$

where sgn is the sign function, that is defined as

$$sgn = \begin{cases} \text{-1} & (x < 0) \\ 0 & (x = 0) \\ 1 & (x > 0). \end{cases}$$

40

Table 3.2: Fit Parameters using Two Skewed Gaussian.

Parameter	Notation	Unit	First Gaussian	Second Gaussian
amplitude	A	mA	2.14	10.88
mean	μ	MeV	12.07	12.32
sigma left	σ_L	MeV	4.47	0.70
sigma right	σ_R	MeV	1.20	0.45

The other variables are defined as $\sigma_1 = \frac{\sigma_{r,1}+\sigma_{l,1}}{2}$, $\sigma_2 = \frac{\sigma_{r,2}+\sigma_{l,2}}{2}$, $E_1 = \frac{\sigma_{r,1}-\sigma_{l,1}}{\sigma_{r,1}+\sigma_{l,1}}$, and $E_2 = \frac{\sigma_{r,2}-\sigma_{l,2}}{\sigma_{r,2}+\sigma_{l,2}}$. The measurement results and fits are shown in Figure 3.6 and in Table 3.2.
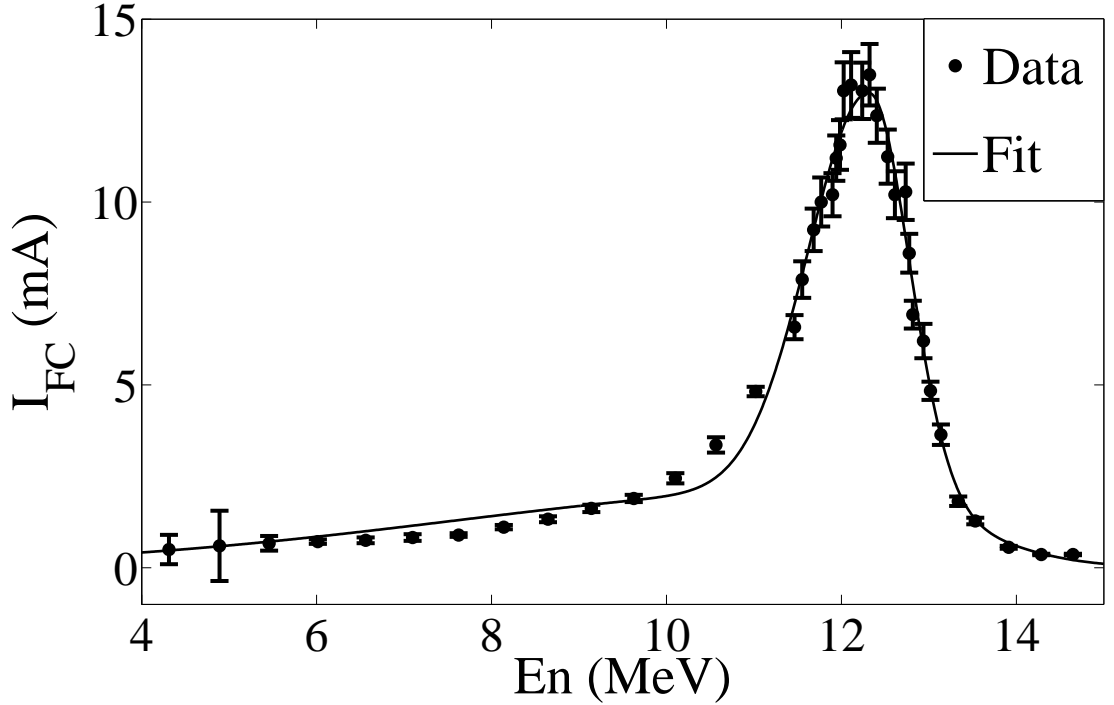
Figure 3.6: HRRL energy scan (dots) and a fit (line) using two skewed Gaussian distributions.

3.3 Positron Production Experiment

Positrons were produced using the HRRL located in the Beam Lab of the Physics Department. The electron beam of the HRRL was incident on positron production

Table 3.3: Scintillator Calibration Data.

Run Number	Faraday Cup Charge Area (nVs)	Mean of ADC Channel 9
3703	1201 ± 10	1126 ± 0.8
3705	777 ± 110	791.8 ± 0.6
3706	367.7 ± 2.3	242.1 ± 0.3

target T1 and the positrons produced downstream of T1 were transported to anni-hilation target T2, where they annihilate and created back to back 511 keV photon pairs. Two NaI detectors, shielded with Pb bricks, were placed horizontally and operated in coincidence with the electron gun pulse to detect 511 keV photon pairs from T2. The electron beam current of the HRRL was monitored by a scintillator placed between Q9 and Q10. The ROOT script used to calculate number (charge) of positrons (electrons) and the ratio of the two is given in the Appendix E.

3.3.1 The Electron Beam Current Measurement

A scintillator was placed between Q9 and Q10, as shown in Figure 3.7, to monitor the electron beam current. The electron beam current was changed incrementally to measure the correlation between the scintillator and the accelerated electron beam. The beam current was measured using FC1 and the output was integrated using an oscilloscope. The scintillator output was integrated using an ADC (CAEN Mod. V792). As the electron beam current was decreased, the signal observed on the oscilloscope decreased and the ADC measured less charge from the scintillator as shown in Figure 3.8. A linear fit to data resulted a linear relation

$$Q_{e^-}(i) = (0.0186 \pm 0.0028)i + 2.79 \pm 0.08 \text{ C}, \qquad (3.10)$$

where i is ADC channel number and Q is the accelerated electron beam charge. The fit is shown in Figure 3.9.

When running in coincidence mode, the electron beam current is sampled by the scintillator only when a coincidence event occurs causing a trigger that gates the
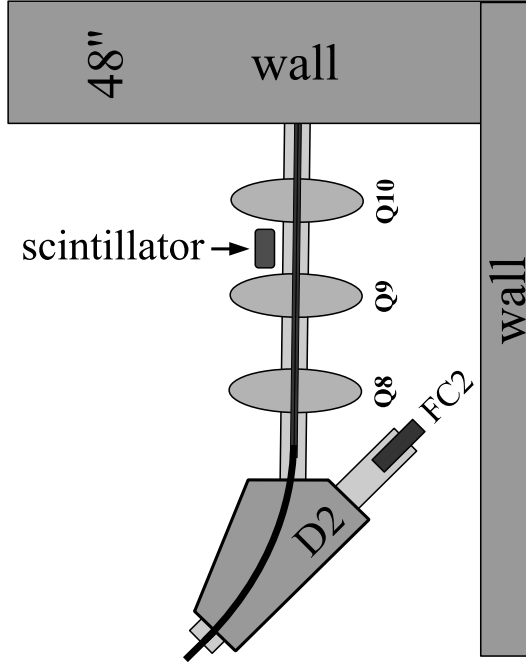
Figure 3.7: The electron beam monitor scintillator.

run No. 3706:
ADC mean at 242.1± 0.3.
scope inegral 7.35 ± 0.05 nC.

run No. 3705:
ADC mean at 791.6 ± 0.6.
scope inegral 15.5 ± 2.2 nC.

run No. 3703:
ADC mean at 1126.0± 0.8.
scope inegral 24.02 ± 0.2 nC.
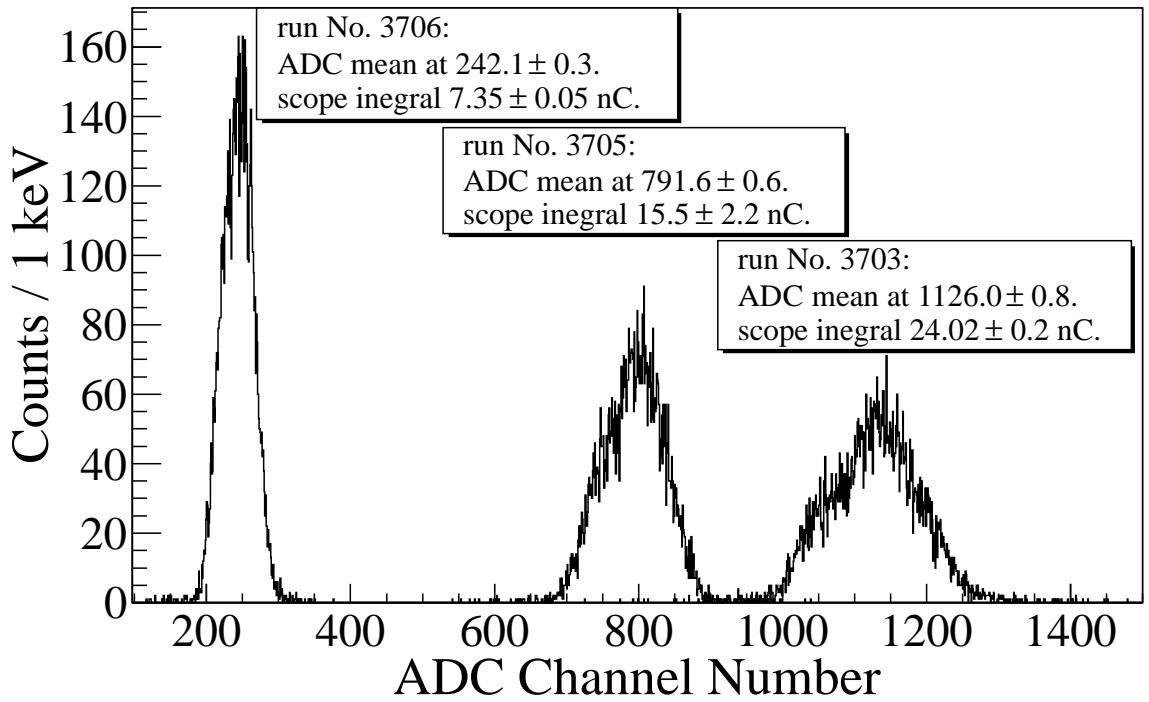
Figure 3.8: The beam monitor scintillator response for three beam currents. The mean of the ADC channel decreased linearly as the electron beam current was decreased. The electron beam current was measured using the Faraday cup at the end of the 0 degree beamline, FC1, and integrated using an oscilloscope.
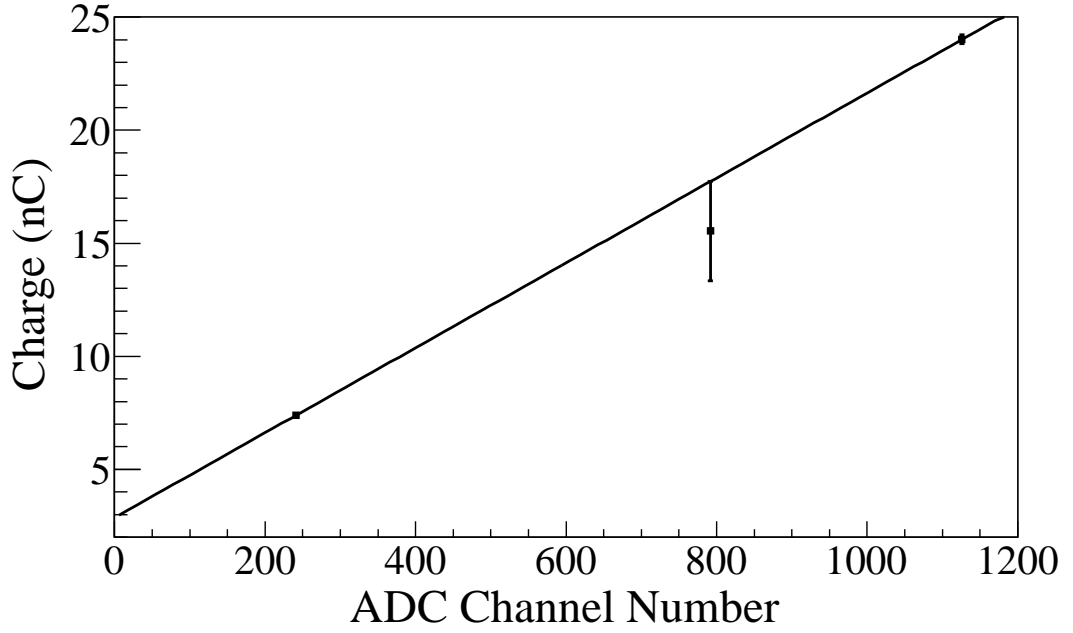
Figure 3.9: Fit of the accelerator beam current vs. the beam monitor scintillator's ADC channel.

ADC and measures the scintillator output for that positron coincidence event. The charge measured by the ADC is the total charge of the electron pulses that created the positron event. The number of beam pulses are counted using a scaler. The total charge on T1 for the entire run is estimated using

$$Q_{\mathrm{C}} = \left(\sum_i^N 0.0186i \times (\text{bin content}[i]) + 2.79 \right) \times \frac{(\text{\# of beam pulses})}{(\text{\# of events})}. \qquad (3.11)$$

3.3.2 NaI Detectors

The NaI detectors were calibrated using radioactive sources as mentioned in Chapter 2. However, in the positron production experiment conducted using the HRRL, the photon peak observed by the NaI detector was not at the channels corresponding the 511 keV energy region (according to the calibration with sources). A Na-22 source was placed between two NaI detectors to measure the spectrum when the RF was on, represented by dotted line (no electrons were fired from accelerator gun), and off, represented by dashed line in Fig 3.10. The solid line in Fig 3.10 represents

the photon spectrum created by 3 MeV positrons impinging on T2.

When the RF was on, no difference was observed for photon peaks created by the 3 MeV positrons and the 511 keV photon peak from Na-22 source. However, when the RF was off, the 511 keV photon peak from Na-22 source occupied a different position in the ADC spectrum. It seems the 511 keV peak would shift when the RF is turned on. The 511 keV peak in the right NaI detector was shifted to the right side of the spectrum by 17 channels when the RF was on as shown in Figure 3.10 (a) while in the left NaI detector the peak shifted to the left by 28 channels as shown if Figure 3.10 (b).

3.3.3   Positron Rate Estimation in AND Mode

The background subtracted and normalized photon energy spectra observed using two NaI detectors for 3.00 ± 0.07 MeV positrons are shown in Figure 3.11. Figure 3.11 (a) and (b) are the background subtracted spectrum with no coincidence or energy cut (OR mode). In OR mode, no coincidence between the two detectors is required. Figure 3.11 (c) and (d) illustrate events observed in coincidence and within an energy window of 511 ± 75 keV for both detectors (AND or coincidence mode). The measured positron rate using NaI detectors in AND mode was 0.25 Hz for 3.00 ± 0.07 MeV positrons when the HRRL was operated at 300 Hz repetition rate, 100 mA peak current, and 300 ns (FWHM) macro pulse length.

3.3.4   The Positron Production Runs

The annihilation target T2 is insertable into the beamline and placed inside a 6-way cross that has its horizontal sides vacuum sealed with 1 mil stainless steel windows. Positrons intercepting T2 thermalise, annihilate, and produce 511 keV photon pairs back-to-back. These photons are detected by two NaI detectors facing T2 and shielded with Pb bricks as shown in Figure 3.12. The background was measured by retracting T2 thereby allowing positrons to exit the beamline and be absorbed by the beam dump.
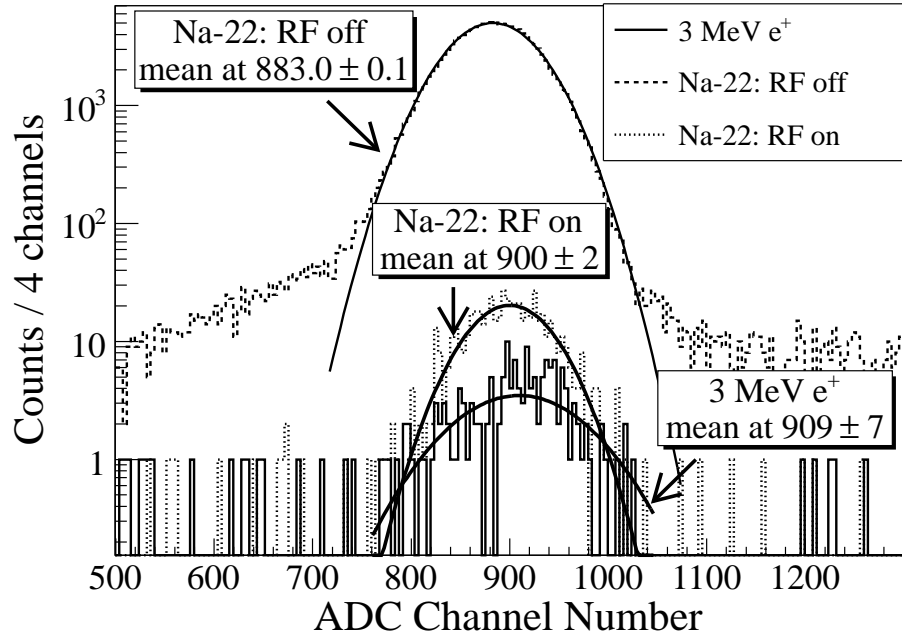
(a) Left NaI detector.
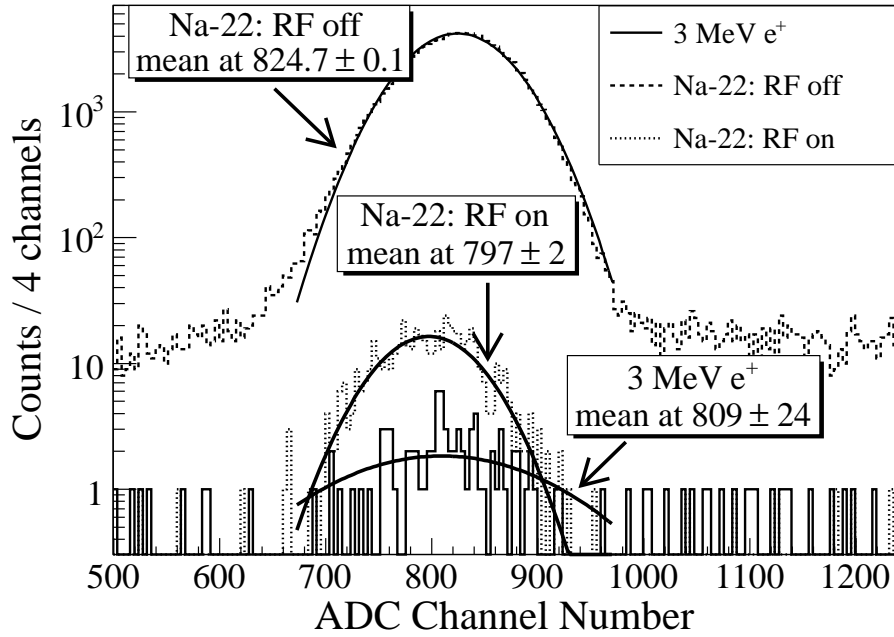
(b) Right NaI detector.

Figure 3.10: The 511 keV peak shift observed using NaI detectors when the accelerator RF was on. The spectra were taken with RF on (dotted line) and with RF off (dashed line). The solid line represents the photon spectrum created by 3 MeV positrons impinging on T2.
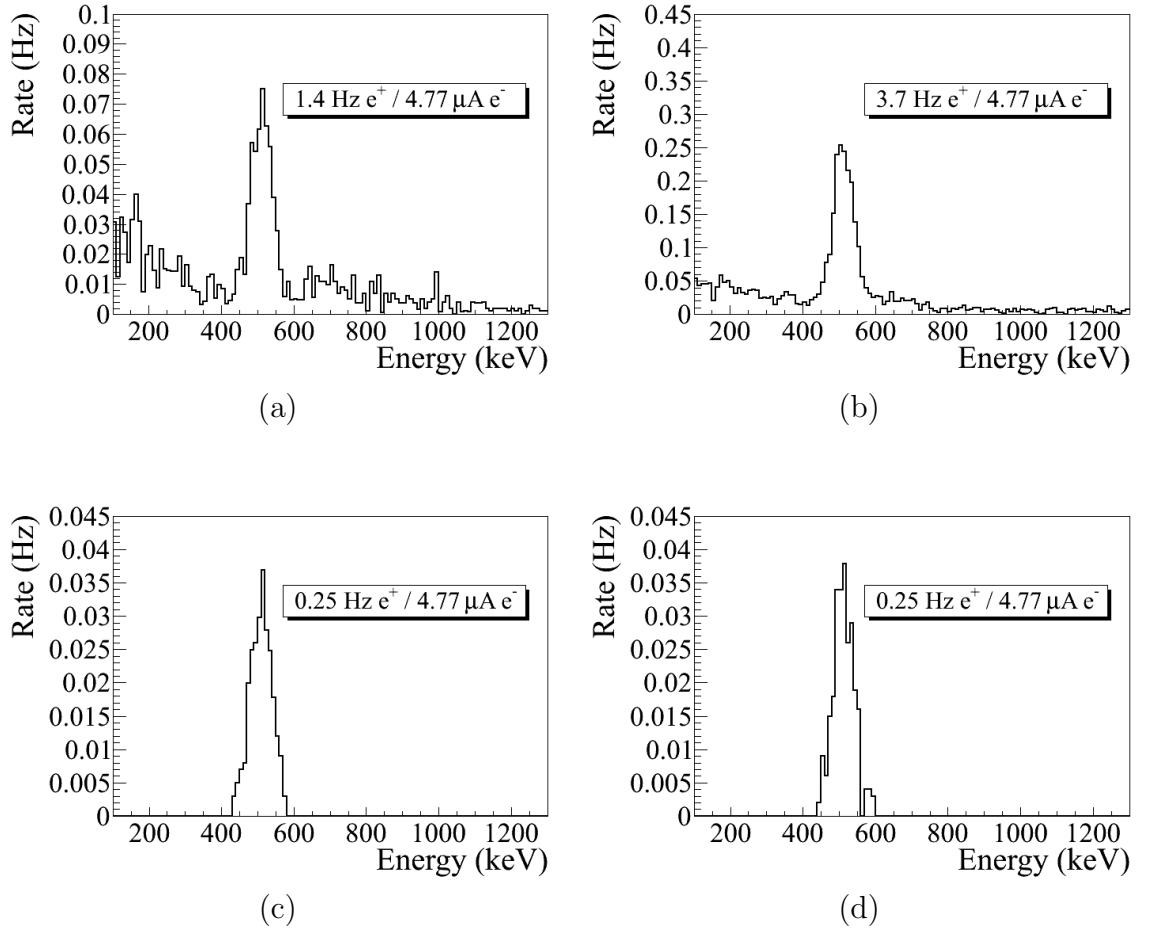
Figure 3.11: Photon spectrum using NaI detectors created by 3 MeV positrons incident on T2 after background subtraction. (a) and (b) are spectrum after background subtractions. (c) and (d) are the spectrum of events coincident in both detectors in 511 keV peaks.
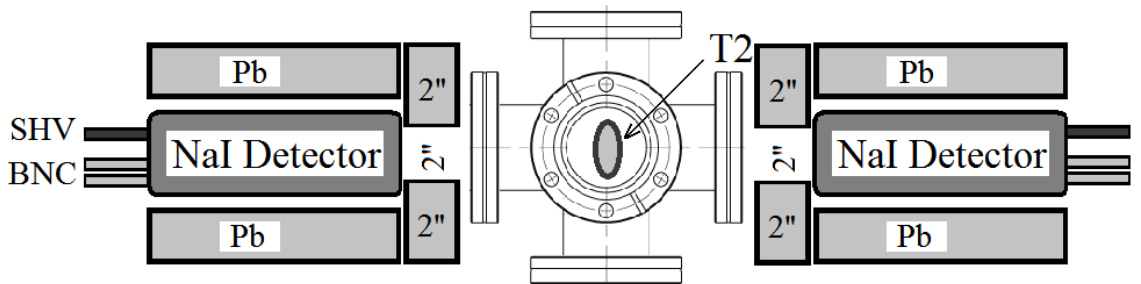
Figure 3.12: Positron detection system using T2 and NaI detectors.

As shown in Figure 3.13, a 511 keV peak was observed (solid line) when T2 was in. A permanent dipole magnet was placed on the beamline after Q10 to deflect charged particles on the accelerator side preventing them from entering the shielded cell. No peak was observed (dashed line) when T2 was in and the permanent magnet was used. Nor was any peak observed (doted dashed line) when both T2 and the permanent magnet were removed. Thus, one may argue that the observed peak is due to positrons annihilating in T2.

(a) Original spectrum on left NaI. (b) Original spectrum on right NaI.
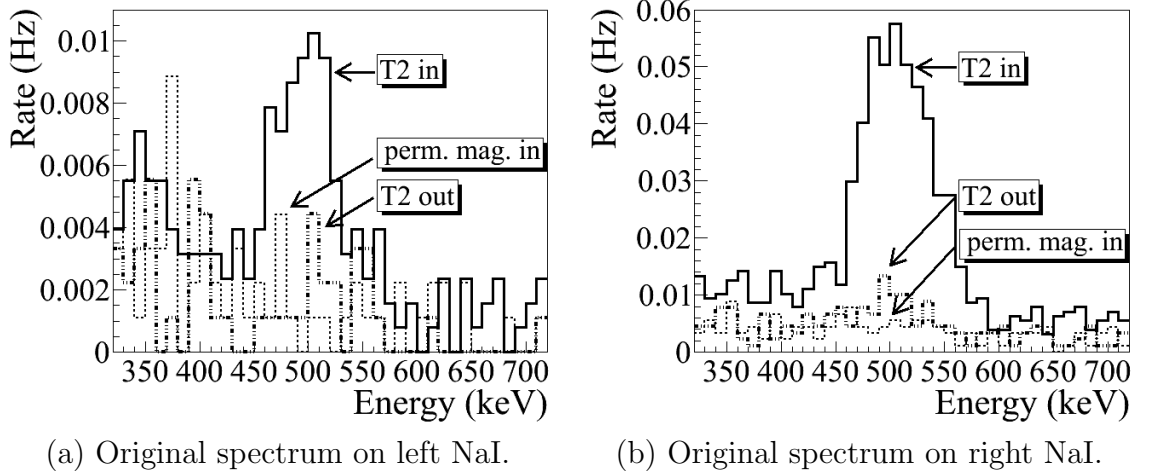
Figure 3.13: Photon spectrum when a permanent dipole magnet is inserted along with T2 (dashed line), dipole out and T2 in (solid line), and dipole removed and T2 out (dotted dashed line). The positron energy incident on T2 was 2.15 ± 0.06 MeV.

The normalized photon energy spectra observed by two NaI detectors are shown in Figure 3.14 when T2 was both in (signal) and out (background) of the beamline. Figure 3.14 (c) and (d) illustrate the events observed when 511 keV photons were required in both detectors. The signal is indicated by the solid line and background by dashed line.

3.3.5 Positron to Electron Ratio in AND Mode

Gaussian distributions were fit to the 511 keV photon peaks observed by the NaI detectors as shown in Figure 3.15. The fits result in $\sigma_{NaI,511} = 37.5 \pm 3.0$ keV. Events in the experiment were counted if they fell within a $2\sigma_{NaI,511}$ energy window
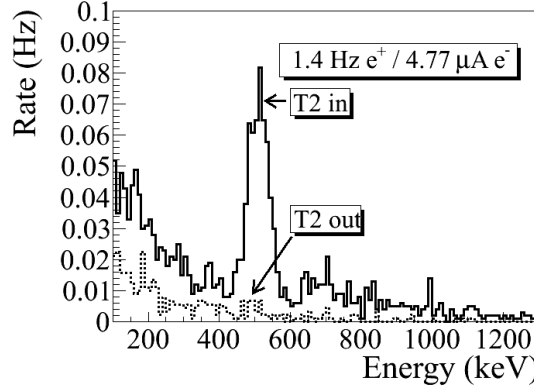
(a) Original spectrum on left NaI.
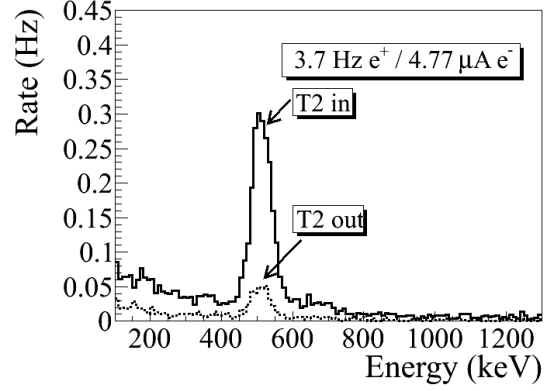
(b) Original spectrum on right NaI.
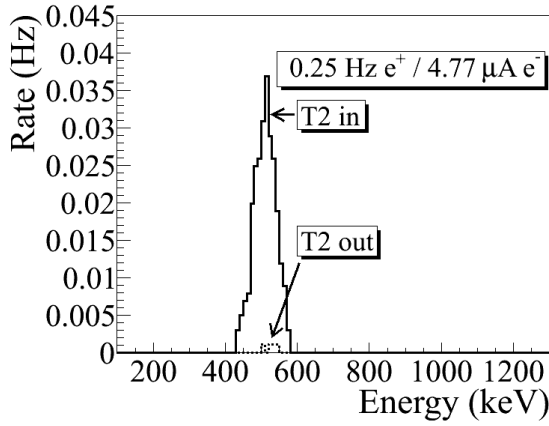
(c) Spectrum with cut on left NaI.
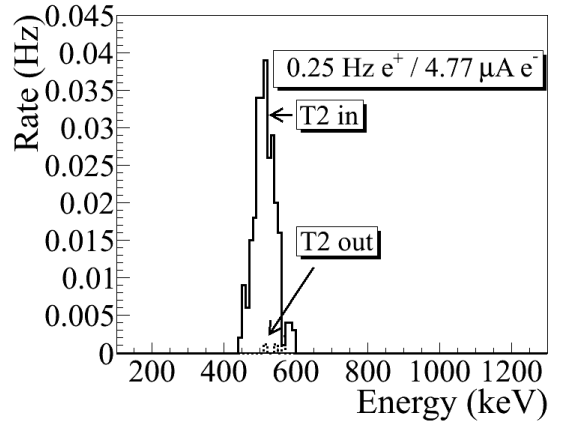
(d) Spectrum with cut on right NaI.

Figure 3.14: The time normalized spectra of photons created by 3 MeV positrons incident on T2. In the top row are original spectrum and in the bottom row are spectrum of incidents happened in the 511 keV peak coincidently in both detectors. The positron beam energy incident on the T2 was 3.00 ± 0.06 MeV.

Table 3.4: Positron to Electron Rate Ratio.

Energy	Positron to Electron Ratio
1.02 ± 0.03	$(1.7 \pm 0.6) \times 10^{-16}$
2.15 ± 0.06	$(8.6 \pm 1.5) \times 10^{-16}$
3.00 ± 0.07	$(8.52 \pm 0.54) \times 10^{-15}$
4.02 ± 0.07	$(3.11 \pm 0.31) \times 10^{-15}$
5.00 ± 0.06	$(3.32 \pm 0.89) \times 10^{-15}$

$(436-586$ keV) for both detectors. The ratios of positrons, detected using NaI detectors in coincidence mode, to the electrons impinging on T1 at different energies are given in Table 3.4 with statistical errors. The systematic errors are discussed in the next section and the results are plotted in Figure 3.17.

(a) Left NaI detector.

(b) Right NaI detector.
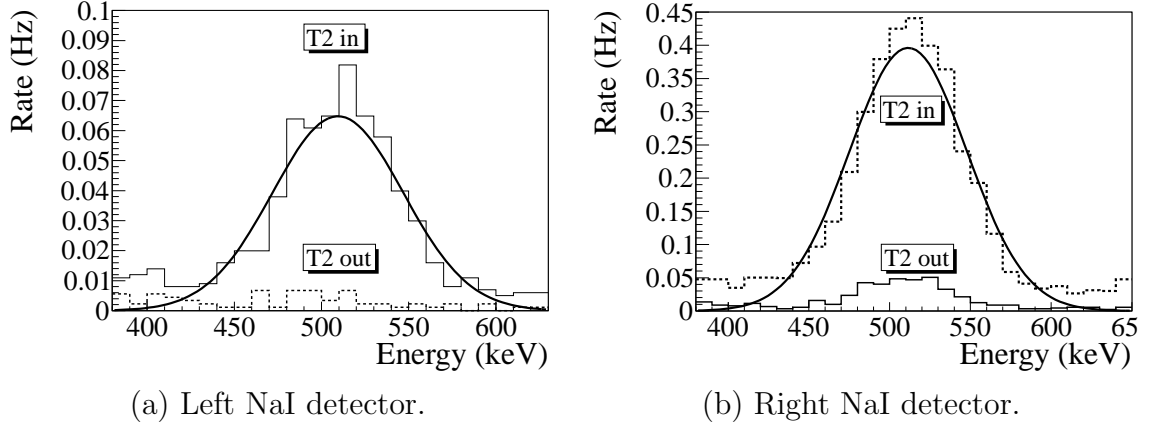
Figure 3.15: The spectrum measured with and without T2. The positron energy was 3 MeV.

3.3.6 Positron Rate Estimation in Software OR Mode

The ratio of 511 keV photons counted in software OR mode to the electrons incident on T1 are given in Table 3.5. In these runs listed in the table, a triple coincidence between NaI detectors and the gun pulse was required. In the software OR mode, there is no software coincidence required between two NaI detectors. In OR mode, left and right NaI detectors observe different 511 keV photon rates (see section 4.4 of Chapter 4 for the detailed analysis on the count asymmetry in NaI

Table 3.5: The Ratio of 511 keV Photons Measured in OR Mode to the Electrons Incident on T1 Measured in Different $\sigma_{NaI,511}$ Energy Windows.

1 $\sigma_{NaI,511}$ Cut			
Energy (MeV)	e^+/e^- on NaI Right	e^+/e^- on NaI Left	Asymmetry
1.02 ± 0.03	$(2.5 \pm 0.3) \times 10^{-15}$	$(0.0 \pm 0.0) \times 10^{-15}$	$96.0 \pm 2.8\%$
2.15 ± 0.06	$(8.5 \pm 0.6) \times 10^{-15}$	$(1.0 \pm 0.2) \times 10^{-15}$	$79.2 \pm 4.0\%$
3.00 ± 0.07	$(75.1 \pm 1.5) \times 10^{-15}$	$(14.2 \pm 0.6) \times 10^{-15}$	$68.2 \pm 1.3\%$
4.02 ± 0.07	$(42.0 \pm 1.2) \times 10^{-15}$	$(6.0 \pm 0.4) \times 10^{-15}$	$75.1 \pm 1.7\%$
5.00 ± 0.06	$(21.5 \pm 2.3) \times 10^{-15}$	$(4.0 \pm 1.0) \times 10^{-15}$	$68.5 \pm 7.0\%$
2 $\sigma_{NaI,511}$ Cut			
Energy (MeV)	e^+/e^- on NaI Right	e^+/e^- on NaI Left	Asymmetry
1.02 ± 0.03	$(2.9 \pm 0.3) \times 10^{-15}$	$(0.3 \pm 0.1) \times 10^{-15}$	$81.5 \pm 5.2\%$
2.15 ± 0.06	$(11.8 \pm 0.7) \times 10^{-15}$	$(1.4 \pm 0.2) \times 10^{-15}$	$79.0 \pm 3.4\%$
3.00 ± 0.07	$(98.0 \pm 1.7) \times 10^{-15}$	$(19.0 \pm 0.7) \times 10^{-15}$	$67.6 \pm 1.2\%$
4.02 ± 0.07	$(53.9 \pm 1.3) \times 10^{-15}$	$(8.1 \pm 0.5) \times 10^{-15}$	$73.9 \pm 1.5\%$
5.00 ± 0.06	$(28.6 \pm 2.6) \times 10^{-15}$	$(5.5 \pm 1.1) \times 10^{-15}$	$67.6 \pm 6.1\%$
3 $\sigma_{NaI,511}$ Cut			
Energy (MeV)	e^+/e^- on NaI Right	e^+/e^- on NaI Left	Asymmetry
1.02 ± 0.03	$(3.4 \pm 0.3) \times 10^{-15}$	$(0.4 \pm 0.1) \times 10^{-15}$	$78.4 \pm 5.1\%$
2.15 ± 0.06	$(13.4 \pm 0.7) \times 10^{-15}$	$(1.5 \pm 0.2) \times 10^{-15}$	$79.3 \pm 3.1\%$
3.00 ± 0.07	$(106.3 \pm 1.8) \times 10^{-15}$	$(21.4 \pm 0.8) \times 10^{-15}$	$66.5 \pm 1.1\%$
4.02 ± 0.07	$(58.9 \pm 1.4) \times 10^{-15}$	$(9.4 \pm 0.5) \times 10^{-15}$	$72.5 \pm 1.5\%$
5.00 ± 0.06	$(16.4 \pm 1.4) \times 10^{-15}$	$(2.9 \pm 0.6) \times 10^{-15}$	$70.0 \pm 5.6\%$

detectors). In the experiment, the upstream side of the T2 was facing the right NaI detector and the right NaI detected more 511 keV photons. An asymmetry was defined as

$$\text{Asymmetry} = \frac{N_r - N_l}{N_r + N_l} \times 100\%, \tag{3.12}$$

where N_r and N_l are the number of 511 keV photons detected by right and left NaI detectors respectively. The 511 keV photons are counted in 1, 2, and 3 $\sigma_{NaI,511}$ ($\sigma_{NaI,511} = 37.5 \pm 3.0$ keV) energy windows.

The errors given in Table 3.5 are statistical. Counting positrons in AND mode measures positron rates that are a factor of 10 lower than the OR mode rates. The

asymmetry tends to decrease as the positron energy increases. The average ratios are given in Table 3.6. In the table, the first error is systematic and second one is statistical. Section 4.4 explains the source of this asymmetry as being due to the positron annihilation depth in T2.

3.3.7   Positron Rate Estimation in Hardware OR Mode

The positron rate was also measured by running NaI detectors in OR mode. The photon spectra are shown in Figure 3.16 for 2.15 ± 0.06 MeV positrons incident on T2. Two NaI detectors were operated in hardware OR mode in these runs. The rate was 0.21 Hz for left and 0.35 Hz right NaI detectors in OR mode. However, when a software coincidence is required in both detectors by counting only the events that occur within the 511 keV peaks of both detectors, the rate dropped to 0.028 Hz.

(a) Left NaI detector.   (b) Right NaI detector.
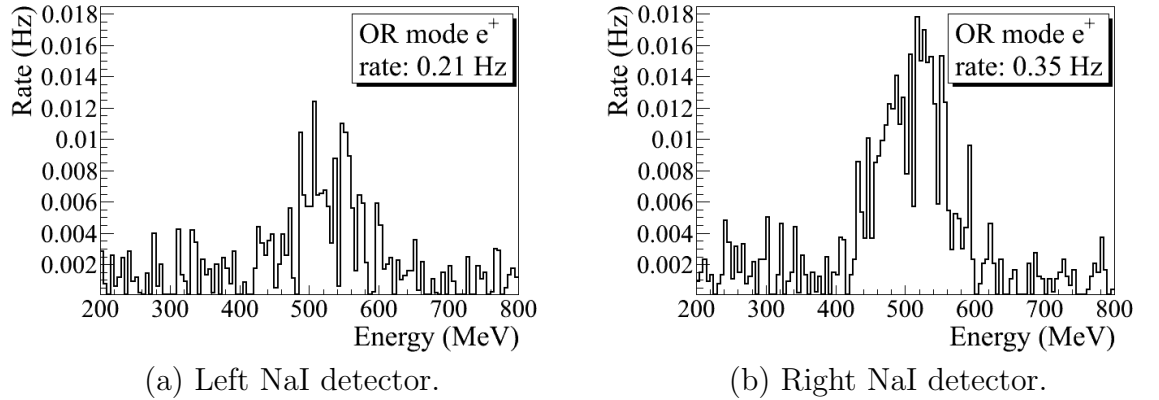
Figure 3.16: The photon rates for 2.15 ± 0.06 MeV incident positrons measured by running NaI detectors in OR mode. The rate was 0.21 Hz for left and 0.35 Hz right NaI detectors in OR mode while the rate in coincidence (AND) mode was 0.028 Hz.

3.4   Systematic Error Analysis for AND Mode Rate

The systematic errors in the positron production experiment could be introduced by the uncertainty in the magnetic fields and misalignment of the quadrupoles. These systematic errors are discussed in section 6 of Chapter 4. The positron and electron

Table 3.6: The Ratio of 511 keV Photons Measured in OR Mode to the Electrons Incident on T1.

Energy (MeV)	e^+/e^- on NaI Right	e^+/e^- on NaI Left	Asymmetry
1.02 ± 0.03	$(2.9 \pm 0.5 \pm 0.3) \times 10^{-15}$	$(0.3 \pm 0.2 \pm 0.1) \times 10^{-15}$	$85.3 \pm 9.4 \pm 5.2\%$
2.15 ± 0.06	$(11.2 \pm 2.5 \pm 0.7) \times 10^{-15}$	$(1.3 \pm 0.3 \pm 0.2) \times 10^{-15}$	$79.2 \pm 0.2 \pm 3.4\%$
3.00 ± 0.07	$(93.1 \pm 16 \pm 1.7) \times 10^{-15}$	$(18.2 \pm 3.7 \pm 0.7) \times 10^{-15}$	$67.4 \pm 0.9 \pm 1.2\%$
4.02 ± 0.07	$(51.6 \pm 8.7 \pm 1.3) \times 10^{-15}$	$(7.8 \pm 1.7 \pm 0.5) \times 10^{-15}$	$73.8 \pm 1.3 \pm 1.5\%$
5.00 ± 0.06	$(22.2 \pm 6.1 \pm 2.6) \times 10^{-15}$	$(4.1 \pm 1.3 \pm 1.1) \times 10^{-15}$	$68.7 \pm 1.2 \pm 6.1\%$

normalization in time can introduce systematic error as well. However, the uncertainty in run duration time is very small (0.1−0.2%) and can be ignored (the duration of positron production runs are around 500∼1000 seconds and the uncertainty is about 1 second). The uncertainty in the 511 keV peaks detected by the NaI detectors would also contribute to the systematic error.

Gaussian distributions were fit to the 511 keV photon peaks observed by the NaI detectors as shown in Figure 3.15 and the fits result in $\sigma_{NaI,511} = 37.5 \pm 3.0$ keV. Events in the experiment were observed in coincidence and within a $2\sigma_{NaI,511}$ energy window (436−586 keV) for both detectors. The systematic error of the 511 keV photon counts introduced by the uncertainty in the 511 keV peak is studied by counting the photons with $1\sigma_{NaI,511}$ (473.5−548.5 keV) and $3\sigma_{NaI,511}$ (398.5−623.5 keV) energy windows. The positron to electron rate ratio for different energy windows are given in Table 3.7. The results are plotted in Figure 3.17.

Table 3.7: Positron to Electron Rate Ratio: Systematic Error Introduced by The Uncertainty of The 511 keV Peak.

Energy (MeV)	Positron to Electron Ratio Energy Window: $2\sigma_{NaI,511}$	Positron to Electron Ratio Energy Window: $3\sigma_{NaI,511}$	Positron to Electron Ratio Energy Window: $1\sigma_{NaI,511}$
1.02 ± 0.03	$(1.7 \pm 0.6) \times 10^{-16}$	$(1.7 \pm 0.6) \times 10^{-16}$	$(0.5 \pm 0.4) \times 10^{-16}$
2.15 ± 0.06	$(8.6 \pm 1.5) \times 10^{-16}$	$(9.2 \pm 2.0) \times 10^{-16}$	$(3.0 \pm 0.9) \times 10^{-16}$
3.00 ± 0.07	$(8.52 \pm 0.54) \times 10^{-15}$	$(9.90 \pm 0.58) \times 10^{-15}$	$(4.20 \pm 0.35) \times 10^{-15}$
4.02 ± 0.07	$(3.11 \pm 0.31) \times 10^{-15}$	$(3.66 \pm 0.34) \times 10^{-15}$	$(2.07 \pm 0.26) \times 10^{-15}$
5.00 ± 0.06	$(3.32 \pm 0.89) \times 10^{-15}$	$(3.55 \pm 0.92) \times 10^{-15}$	$(1.66 \pm 0.63) \times 10^{-15}$
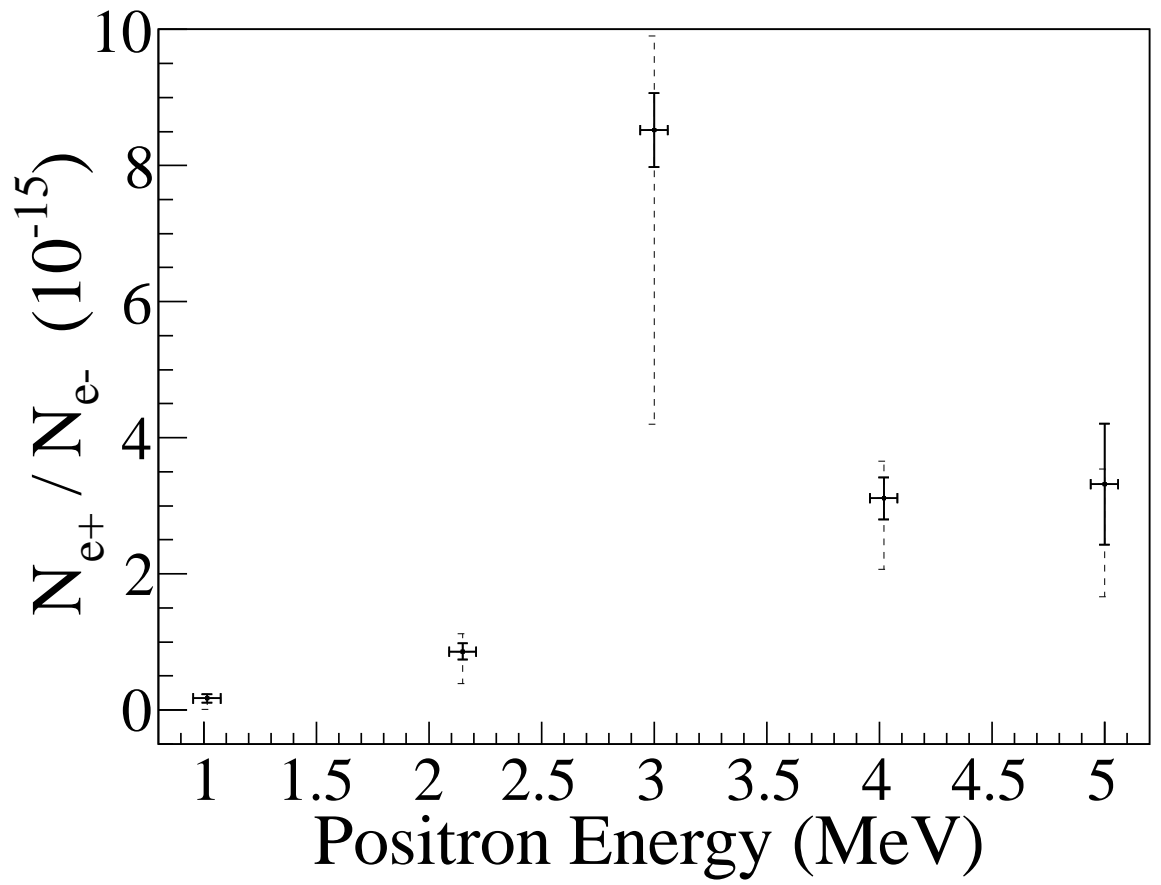
Figure 3.17: The ratios of positrons detected by NaI detectors in coincidence mode to the electrons impinging T1. The solid error bars are statistical and the dashed ones are systematic.

Chapter 4

Simulation

The ratios of positrons to the electrons impinging the tungsten production target, T1, was substantially smaller after they traversed the beam line than what was produced at the target (10^{-15} instead of 10^{-3}). Simulations were performed using G4beamline to better understand the losses from the transportation of positrons to the experimental cell. "G4beamline is a particle tracking and simulation program based on the GEANT4 [17] toolkit that is specifically designed to easily simulate beamlines and other systems using single-particle tracking [18]." A sample G4beamline script for positron generation using the new HRRL beamline is given in the appendix F.

The simulation predicts that at least one positron per 1000 incident 10 MeV electrons is produced using a 2 mm thick tungsten target. The simulation revealed that the number of electrons decreased by orders of magnitude as they were transported through some of the beamline magnets. As a result of this beam loss, the simulation was divided into three steps to increase the beam line simulation efficiency. Each step generates particles at different locations along the beamline where the beam loss was found to be substantial. While the first simulation step used the measured electron energy profile, subsequent steps would generate particles based on the particle phase space observed at the end of previous step. The method decreased the simulation time so a sample of more than one million events could be produced within a single day.

The first step in the simulation generated an electron beam with the energy distribution observed in the experiment, see Figure 3.6. The electrons were focused by three quadrupoles onto the positron production target T1 (see Figure 2.2). Electrons

traversing T1 produced bremsstrahlung photons of sufficient energy to produce e^+e^- pairs that would escape the downstream side of the target and be collected by a second quadrupole triplet. The second step simulated the collection and transportation of positrons exiting T1 to the entrance of the first dipole D1. The last step transported positrons from the entrance of D1 all the way to the annihilation target T2, the interactions of positrons with T2, and the detection of the resulting 511 keV photon pairs.

The two targets (T1 and T2) were positioned at different angles with respect to the incident beam momentum vector. The beamline coordinate system aligns the z-axis to point along the incident electrons momentum vector and the x-axis along the horizontal plane. The positron production target, T1, was placed such that the upstream side of T1 was facing vertically down at a 45° angle with respect to the vertical(rotated 45° counter clockwise about x-axis). The positron conversion target, T2, was rotated about two different axes. The first rotation positioned the upstream side of the target so it was facing down by 45° (rotated 45° clockwise about x-axis like T1). The second rotation was 45° about y-axis. As a result, target T2's upstream face was directed towards the beam right NaI detector.

4.1   Step 1 - The Electron Beam Generation and Transportation to T1

In the first simulation step, an electron beam was generated with an energy distribution that was observed in the experiment. The emittance, the Twiss parameters, and the energy distribution of the electron beam were measured experimentally. The energy distribution of the electron beam is shown in Figure 3.6. The distribution was fit using two skewed Gaussian distributions. The fit parameters given in Table 3.2 were used by the simulation to generated electrons.

A series of virtual detectors were placed along the beamline to sample the beam. As an example, three virtual circular detectors and T1 are shown in Figure 4.1. The

electron beam was detected by a virtual detector DUPT1 (Detector UPstream of
T1) placed 25.52 mm upstream of T1. Positrons, electrons, and photons generated
during the interaction of the electron beam with T1 were observed by virtual detectors
DT1 (Detector of T1) and DDNT1 (Detector DowNstream of T1) placed 25.52 mm
downstream of T1.
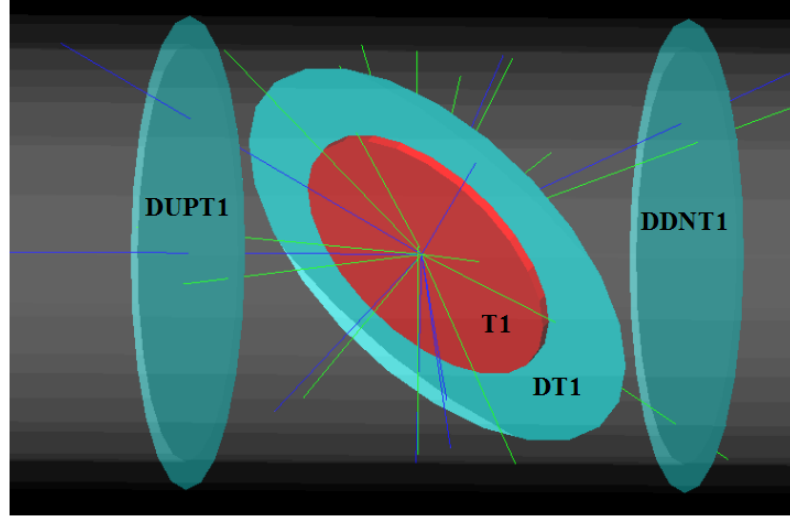
Figure 4.1: The T1 positron target and virtual detectors used in the simulation.
DUPT1 is a virtual detector located upstream of T1 to detect the incoming electron
beam. DDNT1 is a virtual detector downstream of T1. DT1 is a virtual detector
that is placed right after T1 and parallel to it.

4.1.1 The Positron Beam on DDNT1

In the first step, 1.38×10^{10} electrons were generated with the energy distribution
shown by the dotted-dashed line in Figure 4.2. These electrons were transported to
T1 where they produced photons that produced the positron distribution shown by
the solid the line in Figure 4.2 by pair-production. The dashed line is the electron
energy distribution observed by DDNT1. The simulation result using 1.38×10^7 elec-
trons incident on T1 is drawn in Figure 4.2. The incident electrons were detected by
the virtual detector DUPT1 and downstream positrons and electrons were detected

by DDNT1. As shown in Figure 4.2, the electrons pass through T1 loosing approximately 4 MeV while the positrons escape the downstream side of T1 with a mean energy of about 3 MeV. The beam line was set to transport positrons with this mean energy as a result of this prediction.
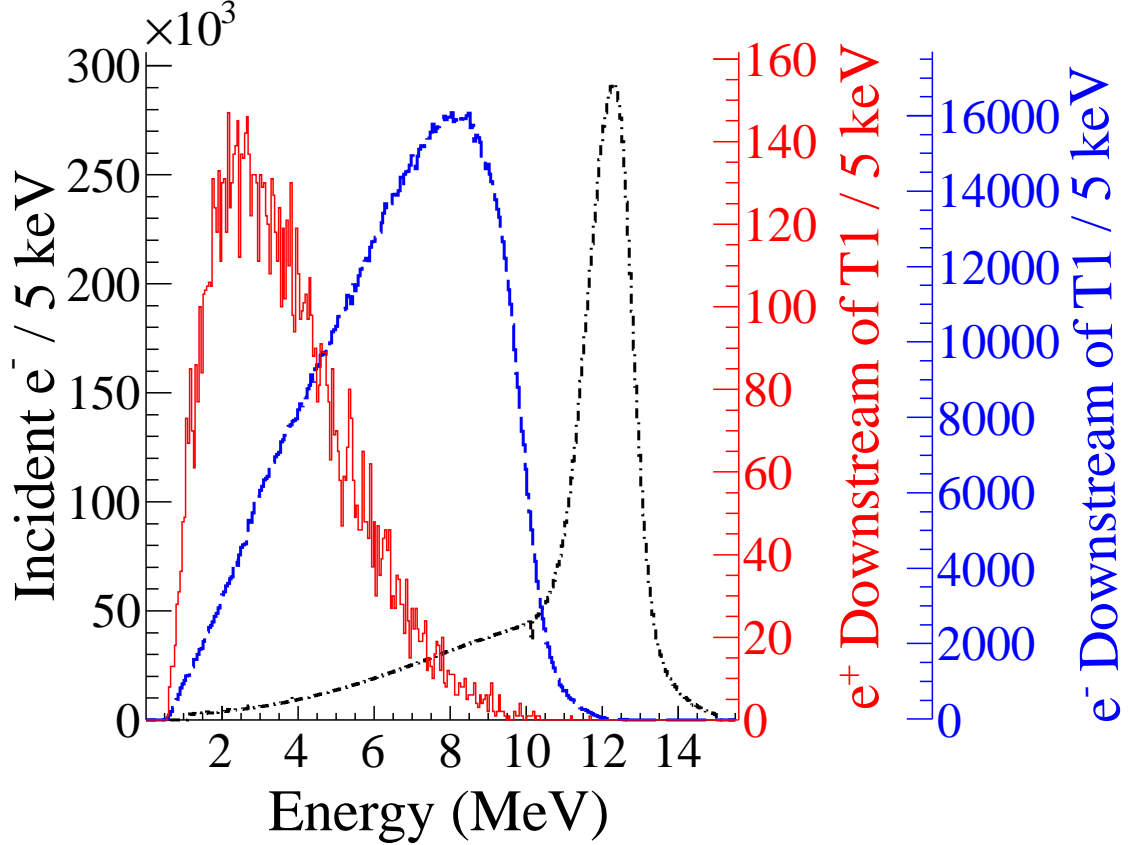
Figure 4.2: The incident electron energy distribution (dotted dashed line), the distribution of electrons after T1 (dashed line), and the distribution of positrons produced (solid line). The incident electron distribution counts were weighted by 0.001.

The positron spatial and angular distribution detected by DDNT1 is shown in Figure 4.3. The y vs. x spatial distribution of the beam is shown in Figure 4.3 (e) and Figure 4.3 (f). As can be seen from Figure 4.3 (b) and (d), the y spatial distribution and divergence, defined in equation 1.5, of the positron beam have a sharp drop in counts in the region between -25.8 mm and -27.2 mm from the beam center. Figure 4.4 shows the geometry and location of T1 and DDNT1. If the size of T1 were to be increased, it would eventually intersect with DDNT1 at a distance between
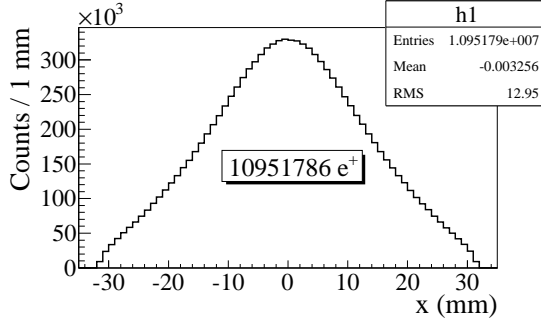
(a) x projection.
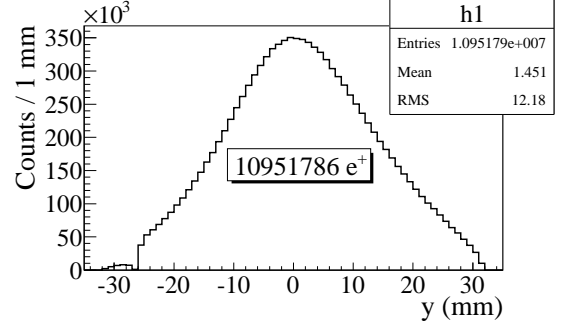
(b) y projection.
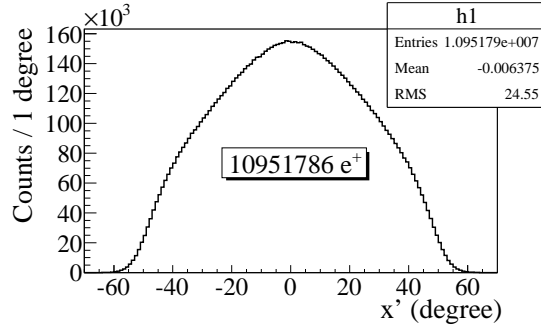
(c) x projection of the divergence.
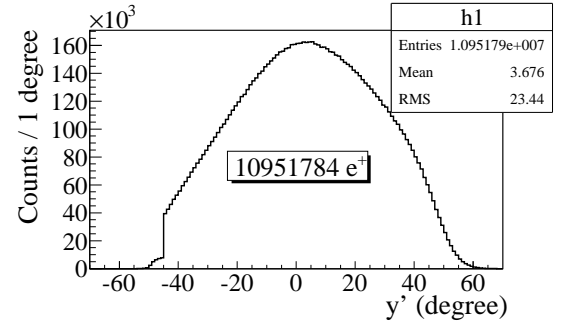
(d) y projection of the divergence.
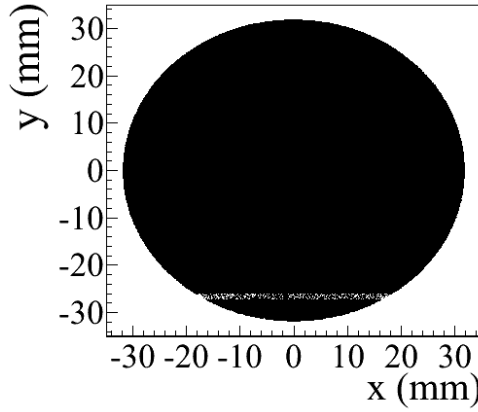
(e) The transverse beam profile.
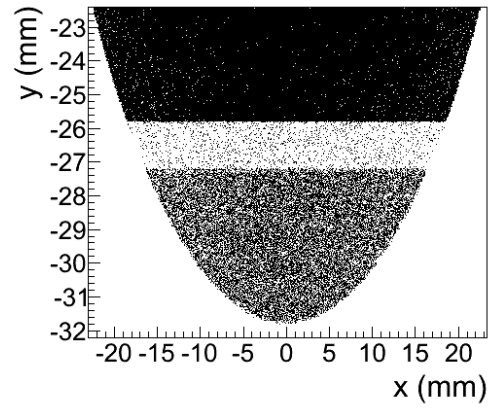
(f) Zoom in of (e).

Figure 4.3: The transverse beam projections and angular distributions of positrons detected. The virtual detector diameter is 30 mm while the beam pipe is only 24 mm.

25.8 mm and 27.2 mm from the beam center, *i.e.* the edge of the T1 is facing this 1.4 mm wide low count area.
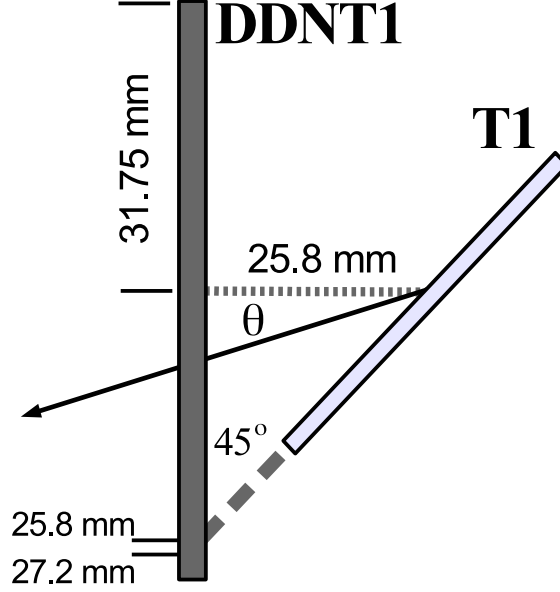
Figure 4.4: The geometry of the target T1 and the virtual detector DDNT1.

As shown in Figure 4.5, the y distribution count decreases at $\theta = 45°$. Positrons were emitted from both the downstream and upstream side of T1. Positrons from the downstream side of T1 intersected the detector at angles below 45° while positrons from the upstream side of T1 begin to hit the detector at angles beyond 45°. Neither positrons upstream nor downstream of T1 traveled to the 1.4 mm wide low count area. Only positrons created on the edge of T1 reached the low count area between 25.8 mm $< x <$ 27.2 mm. As a result, the counts in this area are comparatively lower.

(a) y' *vs.* y.

(b) y' *vs.* y zoom.
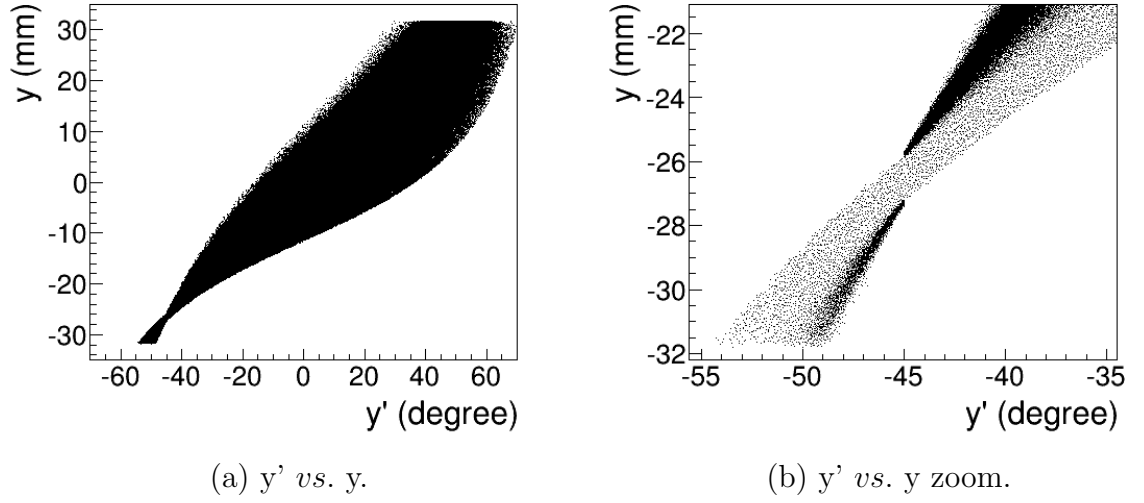
Figure 4.5: The positron beam y' *vs.* y detected by DDNT1.

4.1.2 The Positron Beam on Virtual Detectors DQ4 and DD1

The positron beam energy distributions at the entrance of Q4 observed by virtual detector DQ4 is shown in Figure 4.6. The distribution of positron energies observed leaving the downstream side of the production target T1 as observed by virtual detector DD1UP are also shown. The ratio of positrons leaving the target T1 and entering the first quadrupole indicate that nearly 90% of the positrons are lost. The large positron divergence is responsible for this loss. The median positron energy does not change suggesting that the beamline simulation is tuned to transport the optimal number of positrons emitted by the positron production target, T1.

4.2 Step 2 - The Transportation of The Positron Beam from DDNT1 to The Entrance of The First Dipole

The simulation's second step was designed to predict the amount of beam loss that would result when the positron beam is transported from the entrance of Q4 to
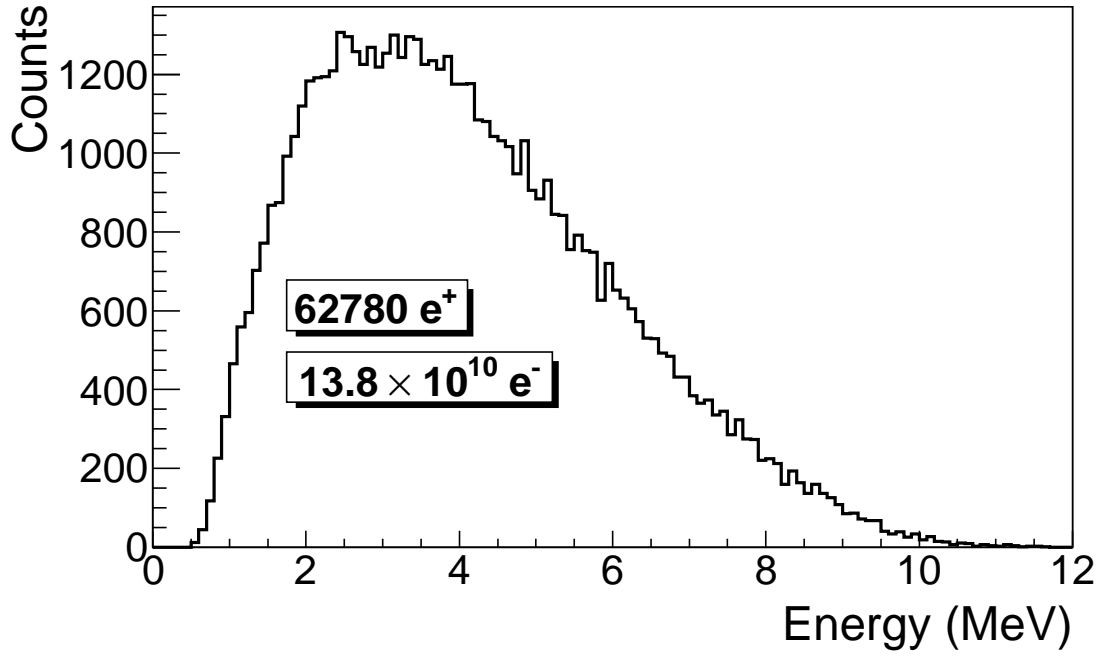
(a) The positron energy distribution on DQ4.
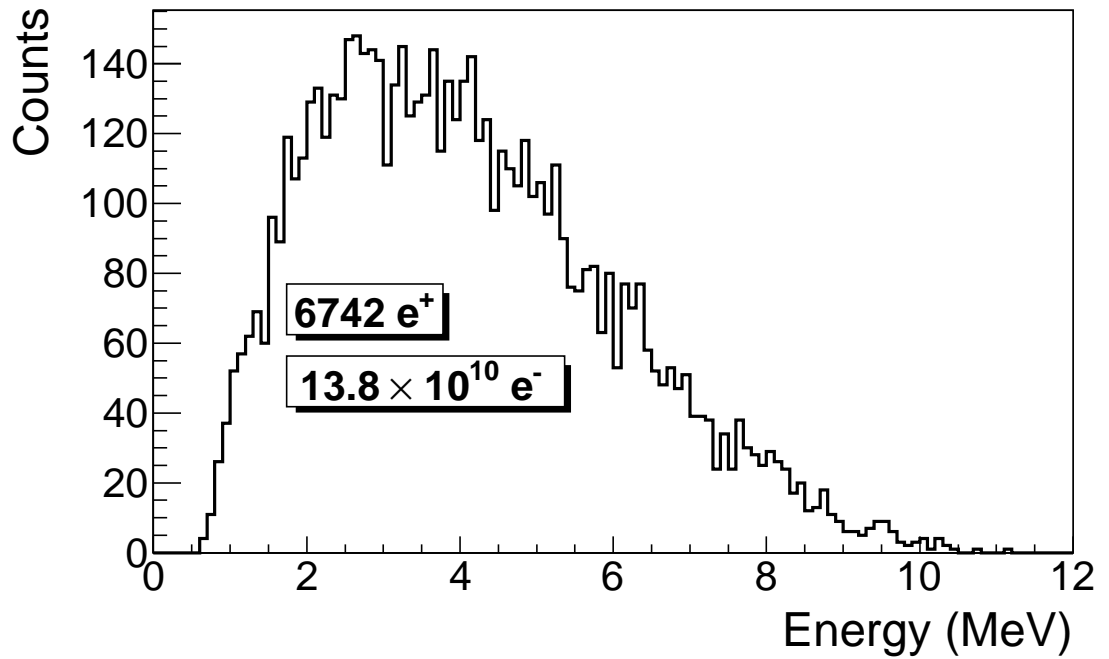
(b) The positron energy distribution on DD1.

Figure 4.6: The positron beam energy distribution detected downstream of T1 just before entering the first quadrupole (a) and after leaving the production target upstream of this quadrupole (b).

the entrance of the first energy selecting dipole D1. The beam observed on detector DDNT1 in step 1 was used to generate positrons directed towards the entrance of the quadrupole Q4. At detector DDNT1, the higher energy positrons tend to have smaller polar angles and are closer to the beam center. Positrons were generated in 1 keV/c momentum bins with different weights, spatial, and angular distributions to reproduce the distributions observed in step 1. Figure 4.7 illustrates the quadrupole triplet system and the dipole magnet D1 used in the beamline. Positrons generated at DDNT1 are transported to the entrance of D1 through this quadrupole triplet system. The virtual detectors were placed at the entrance of Q4 (DQ4) and D1 (DD1UP) to track the positrons. The simulation predicts that the number of positrons decreases by a factor of ten as they travel through the quad triplet system to the entrance of the first Dipole D1, see Table 4.2.
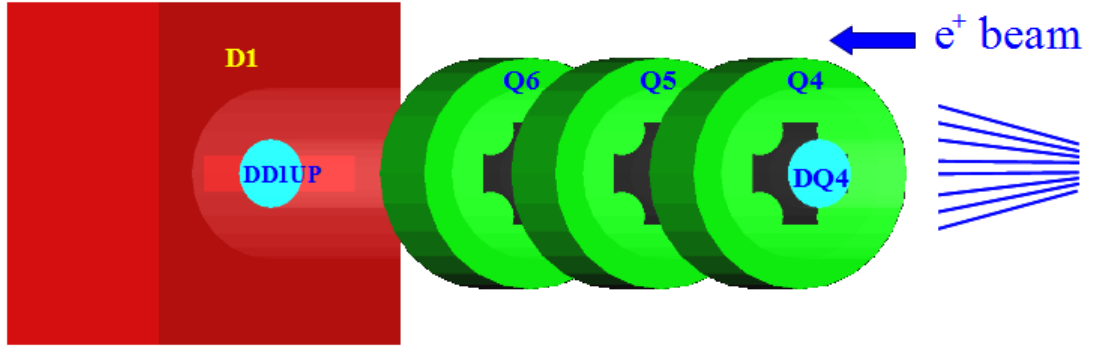
Figure 4.7: The generation and transportation of the positron beam in step 2. The virtual detectors were used to track the positrons.

4.3 Step 3 - The Transportation of Positrons from the Entrance of The First Dipole to T2 and The Detection of 511 keV Photons

In this step, the positron beam was generated at the entrance of the first dipole D1 and observed using virtual detector DD1UP. The beam was deflected 45° by D1 and passed through the energy slit. The positrons diverged along the horizon according to their energy when traversing D1's magnetic field. The energy slit constrained the spatial distribution of the beam by blocking the beam using a 34.8 mm wide gap oriented vertically. Quadrupole Q7, located after the energy slit, was set to 3.5 A (similar to the experiment) in order to focus the beam before it enters a second dipole, D2. The beam was deflected another 45° by D2 and sent through three quadrupoles towards the annihilation target T2 located at the end of the beamline as shown in Figure 4.8.
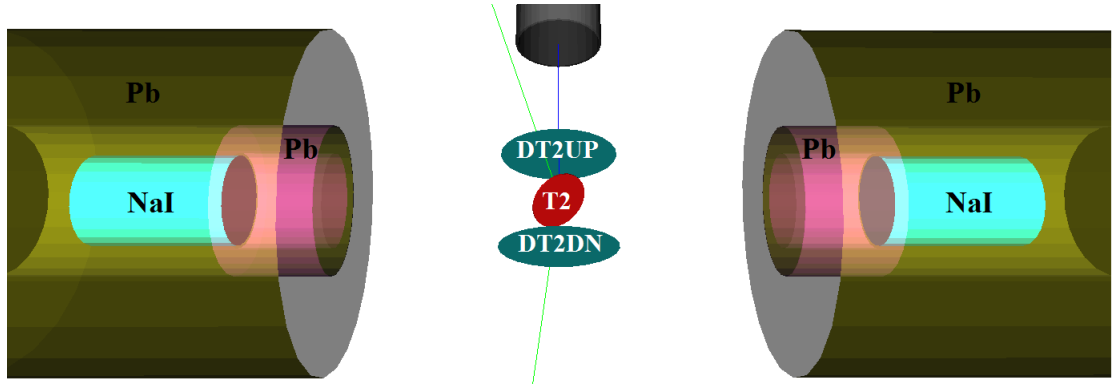
Figure 4.8: T2 and virtual detectors located upstream (DT2UP) and downstream (DT2DN) of T2 are shown at the center of the figure. NaI detectors and Pb shielding are located horizontally on both sides.

As shown in Figure 4.8, two virtual, circular detectors DT2UP and DT2DN with a 48 mm diameter (48 mm is the inner diameter of the beam pipe) were placed upstream and downstream of T2 to detect positrons. Two other virtual detectors, DT2L and DT2R (not shown) with the same diameters as the annihilation target T2 were placed on the left and right side of the beam and parallel to T2 to detect positrons. Two

additional virtual detectors were placed horizontally at the locations of NaI detectors, which were 170 mm away from the beamline center, to detect photons. Two-inch-thick Pb bricks with 2-inch diameter circular openings were positioned between T2 and the NaI virtual detectors. Each detector was surrounded by $2''$ of Pb. When a positron annihilates inside T2, two back-to-back 511 keV photons are produced. An event is registered in the simulation when both NaI detectors observe a 511 keV photon.

4.3.1 Positrons Detected by The Detection System

The photons observed by each NaI detector are subject to the detector efficiency. The detector efficiency chart (shown in Figure 4.9), obtained from Saint-Gobain Crystals [19], indicates that the NaI crystal used in this experiment has an efficiency of 68% for 511 keV photons. If two detectors are operated in coincidence mode, the detection efficiency of the system is $68\% \times 68\% = 46.24\%$.

Figure 4.10 shows the number of 511 keV photon pairs detected in coincidence mode (multiplied by 46.24%) and overlaid with the positrons detected on DDNT1. In step 3 of the simulation, the quadrupole current for Q7 was simulated for 0, 3.5, and 10 A to study the effect of Q7 on the positron energy distribution. As shown in Figure 4.10, the shape of the predicted positron energy distribution more closely resembling the one observed in the experiment when Q7 was set to the value used in the actual experiment, 3.5 A. Fewer positrons are predicted to reach T2 when the Q7 currents are 0 and 10 A. The simulation's prediction for the experiment based on the beamline parameters used during the experiment are given in Table 4.1 as the ratio of the number of e^+ detected in coincidence mode by NaI detectors to the number of e^- incident on T1 for the measured positron energies. The values in Table 4.1 are compared with the experiment in the next chapter.

The remaining sections of this chapter use the above simulation to investigate beam loss, an observed asymmetry in the photon detectors, and systematic errors. Understanding the source of the beam loss through the beam line was critical to
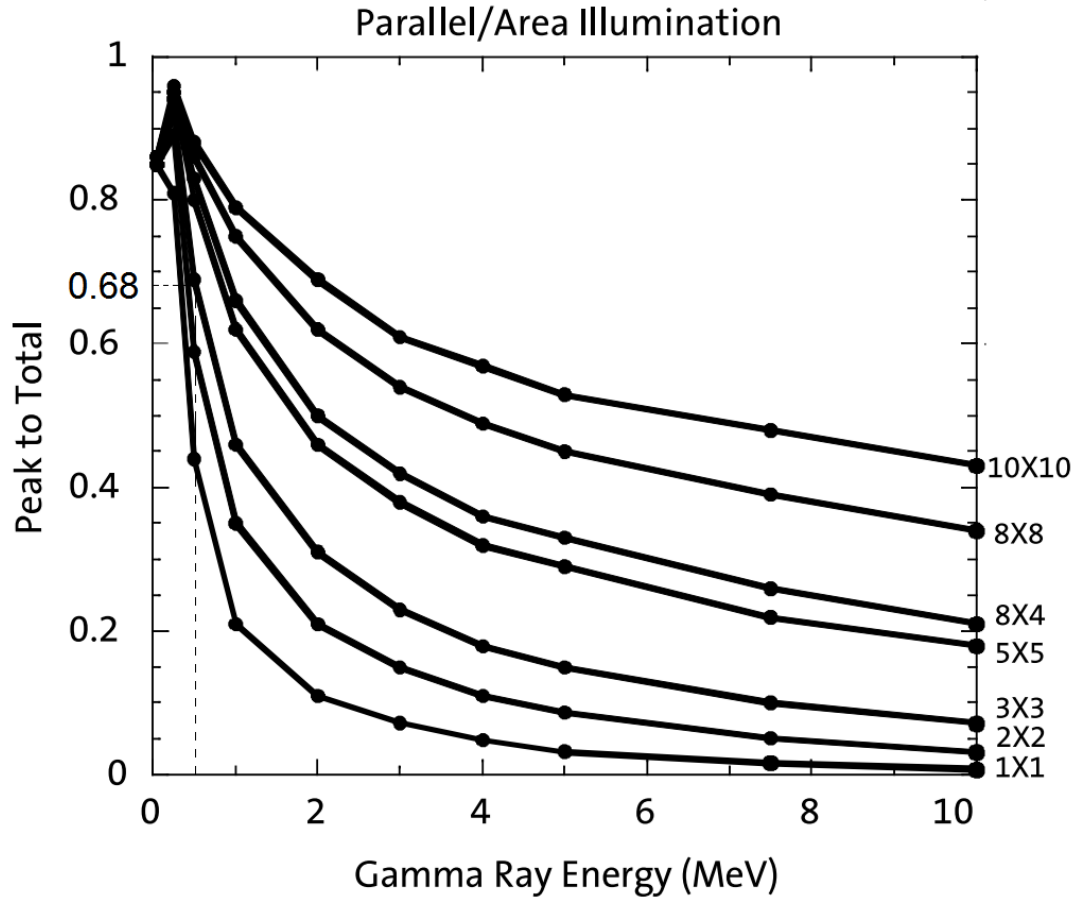
Figure 4.9: NaI detector efficiency obtained from Saint-Gobain Crystals [19]. The lines corresponding to the different crystal sizes (in inches) are shown on the right side of the figure.

Table 4.1: Positron to Electron Ratio Estimated by the Simulation.

Energy (MeV)	Positron to Electron Ratio
1.02 ± 0.03	$(8.90 \pm 5.1) \times 10^{-17}$
2.15 ± 0.06	$(10.10 \pm 0.06) \times 10^{-15}$
3.00 ± 0.07	$(9.96 \pm 0.06) \times 10^{-15}$
4.02 ± 0.07	$(9.67 \pm 0.03) \times 10^{-15}$
5.00 ± 0.06	$(7.80 \pm 0.05) \times 10^{-15}$
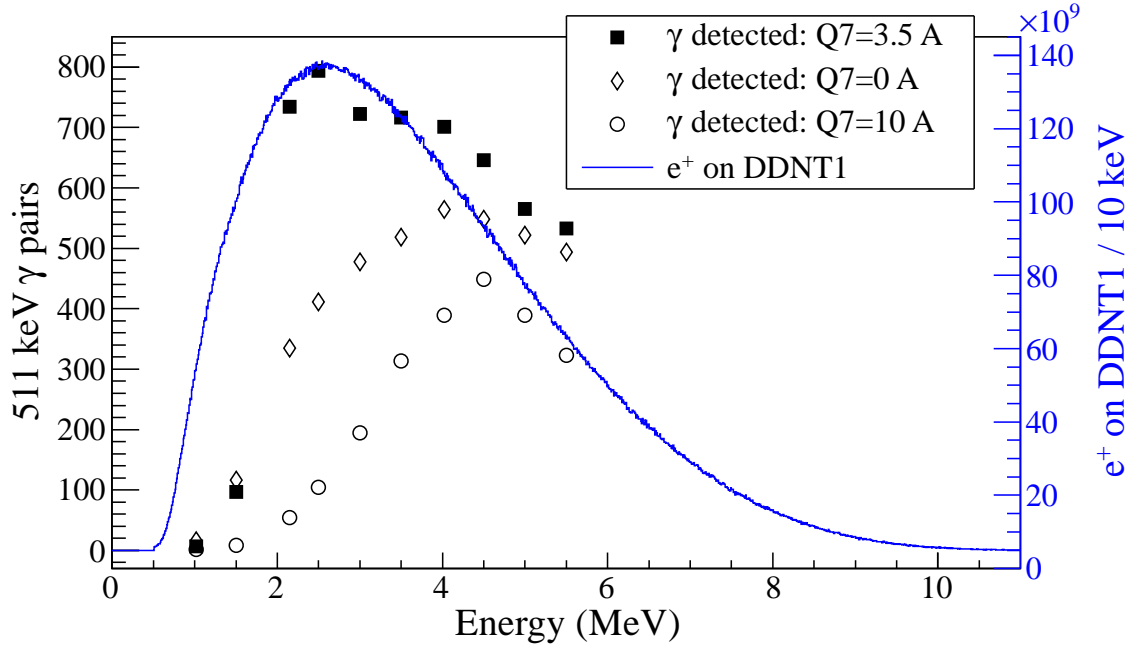
Figure 4.10: Positrons detected on virtual detector DDNT1 and 511 keV photon pairs detected by the NaI detectors in coincidence mode when Q7 set to 0 A, 3.5 A and 10 A.

evaluating the veracity of the data. The large discrepancy of nine orders of magnitude between the observed positron production rate and the expected rate was difficult to believe. As quantified in the sections below, the poor beam quality from a medical linac combined with a poor positron collection system has a large negative impact on the efficiency of producing positrons from electrons. There is also an indication that the beam line alignment plays an even more important role than one might naively expect. The following sections attempt to explains these effects as well as investigate their impact on the systematic error.

4.3.2   Beam Loss Study

The three step simulation method described in the previous section was used to predict the amount of beam loss at several locations along the beam line. Table 4.2 quantifies these predictions. In particular, columns 2 and 3 in Table 4.2 represent the number of positrons that would need to be generated in order to observe the

number of positrons in the remaining columns. The number of 511 keV photon pairs detected by NaI detectors in coincidence mode is shown in the last column of Table 4.2. The number of positrons observed by virtual detectors which were placed along the beamline and 511 keV photon pairs detected are shown in Figure 4.11.
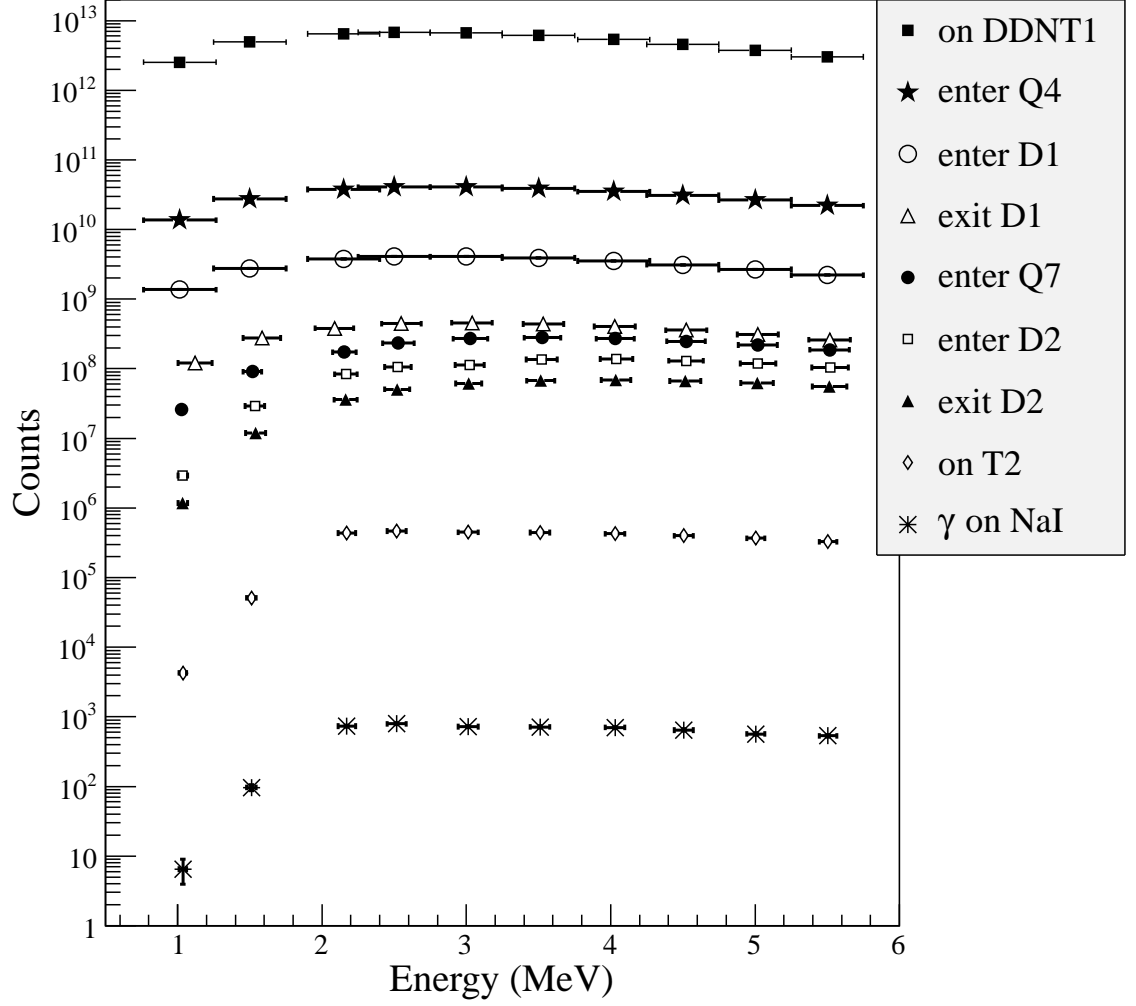
Figure 4.11: Predicted number of positrons transported. Solid squares: positrons incident on DDNT1. Stars: positrons entered Q4. Hollow circles: positrons entered D1. Hollow triangles: positrons exited D1. Solid circles: positrons entered Q7. Hollow squares: positrons entered D2. Solid triangles: positrons exited D2. Hollow diamonds: positrons incident on DT2UP. Asterisks: 511 keV photons detected by NaI detectors in coincidence mode.

The simulation's beam loss prediction between the positron production target, T1, and the first collection quadrupole, Q4, may be compared to a simple solid angle

Table 4.2: Simulation of 7.253×10^{16} Electrons Incident on the T1: The Number of Positrons Transported and the Number of 511 keV Photons Detected in Coincidence Mode.

Energy (MeV)	e^+ on DDNT1	e^+ enter Q4	e^+ enter D1	e^+ exit D1	e^+ enter Q7	e^+ enter D2	e^+ exit D2	e^+ reach T2	511 keV γ by NaI detectors
1.02 ± 0.25	2.5×10^{12}	1.4×10^{10}	1.4×10^{9}	1.2×10^{8}	2.6×10^{7}	2.7×10^{6}	1.2×10^{6}	4.3×10^{3}	7
1.50 ± 0.25	4.9×10^{12}	2.7×10^{10}	2.8×10^{9}	1.8×10^{8}	9.1×10^{7}	2.7×10^{7}	1.2×10^{7}	5.1×10^{4}	97
2.15 ± 0.25	6.5×10^{12}	3.8×10^{10}	3.8×10^{9}	3.8×10^{8}	1.7×10^{8}	7.8×10^{7}	3.6×10^{7}	4.4×10^{5}	734
2.50 ± 0.25	6.8×10^{12}	4.1×10^{10}	4.1×10^{9}	4.4×10^{8}	2.3×10^{8}	1.1×10^{8}	5.0×10^{7}	4.6×10^{5}	794
3.00 ± 0.25	6.6×10^{12}	4.1×10^{10}	4.1×10^{9}	4.6×10^{8}	2.7×10^{8}	1.3×10^{8}	6.1×10^{7}	4.5×10^{5}	723
3.50 ± 0.25	6.1×10^{12}	3.9×10^{10}	3.9×10^{9}	4.4×10^{8}	2.8×10^{8}	1.4×10^{8}	6.7×10^{7}	4.4×10^{5}	716
4.02 ± 0.25	5.3×10^{12}	3.5×10^{10}	3.5×10^{9}	4.1×10^{8}	2.7×10^{8}	1.4×10^{8}	6.9×10^{7}	4.3×10^{5}	702
4.50 ± 0.25	4.6×10^{12}	3.1×10^{10}	3.1×10^{9}	3.6×10^{8}	2.5×10^{8}	1.3×10^{8}	6.7×10^{7}	4.0×10^{5}	646
5.00 ± 0.25	3.8×10^{12}	2.7×10^{10}	2.7×10^{9}	3.1×10^{8}	2.2×10^{8}	1.2×10^{8}	6.2×10^{7}	3.6×10^{5}	566
5.50 ± 0.25	3.0×10^{12}	2.2×10^{10}	2.2×10^{9}	2.6×10^{8}	1.9×10^{8}	1.0×10^{8}	5.6×10^{7}	3.3×10^{5}	533

argument to demonstrate the veracity of the prediction. As shown in Table 4.2, the positron energy distribution is divided into 10 bins. Positrons were detected at both detector DDNT1 (28.5 mm downstream T1) and detector DQ4 (484.4 mm downstream T1). The ratio of positrons detected by DDNT1 to those detected by DQ4 is about 157. The solid angle that the entrance of Q4 makes with respect to T1, if one assumes that T1 is a point source of positrons is about 0.6π steradians. The distance between T1 and the virtual detector DQ4 is 484.4 mm and the radius of DQ4 is 24 mm. The solid angle of the DQ4 is $\Omega_{Q4} = \frac{\pi r^2}{d^2} = \frac{\pi 24^2}{484.4^2}$ steradians. Positrons make up a cone with a 45° half angle, which is $\Omega_{beam} = 0.6\pi$ steradians in solid angle. The ratio of the two solid angles, $\Omega_{Q4}/\Omega_{beam}$, is 1:244, *i.e.* 1 out of 244 positrons makes it from T1 to DQ4, assuming that the positron beam is isotropic inside the cone. However, the positron beam peaks at a smaller angle as shown in Figure 4.3 (c) and (d), and as a result more positrons are transported from DDNT1 to DQ4 which may result in a ratio closer to 1:157.

The first dipole is another region where substantial beam loss is predicted by the simulation. The positron counts dropped one order of magnitude when positrons are transported from the entrance of D1 to the exit of D1. This could be explained by beam scraping on the vacuum chamber. The width of the dipole chamber is 18 mm and the beam pipe diameter is 48 mm. Positrons scraping on the top and bottom of the chamber would be lost. When the dipole was set to transport 3 MeV positrons, positrons having an energy range between 2.8 MeV and 3.3 MeV are transported to the exit D1 as shown in Figure 4.12. This small energy range of 0.5 MeV is only one tenth of the full range subtended somewhat uniformly by the positrons and could easily explain the order of magnitude drop in the number of positrons that traverse the first dipole.

Table 4.3: The Positron Beam Loss along the Beamline When Dipoles Set to Transport 3 MeV Positrons.

Beam Sample Locations	Absolute Counts	Relative Counts
e$^+$ on DDNT1	6.6×10^{12}	9.4×10^{10}
e$^+$ enter Q4	4.1×10^{10}	5.8×10^{7}
e$^+$ enter D1	4.1×10^{9}	5.8×10^{6}
e$^+$ exit D1	4.6×10^{8}	6.6×10^{5}
e$^+$ enter Q7	2.7×10^{8}	3.8×10^{5}
e$^+$ enter D2	1.3×10^{8}	1.9×10^{5}
e$^+$ exit D2	6.1×10^{7}	8.7×10^{4}
e$^+$ on T2	4.4×10^{5}	6.3×10^{2}
e$^+$ annihilated in T2	2.5×10^{5}	3.6×10^{2}
511 keV photons on NaI	723	1
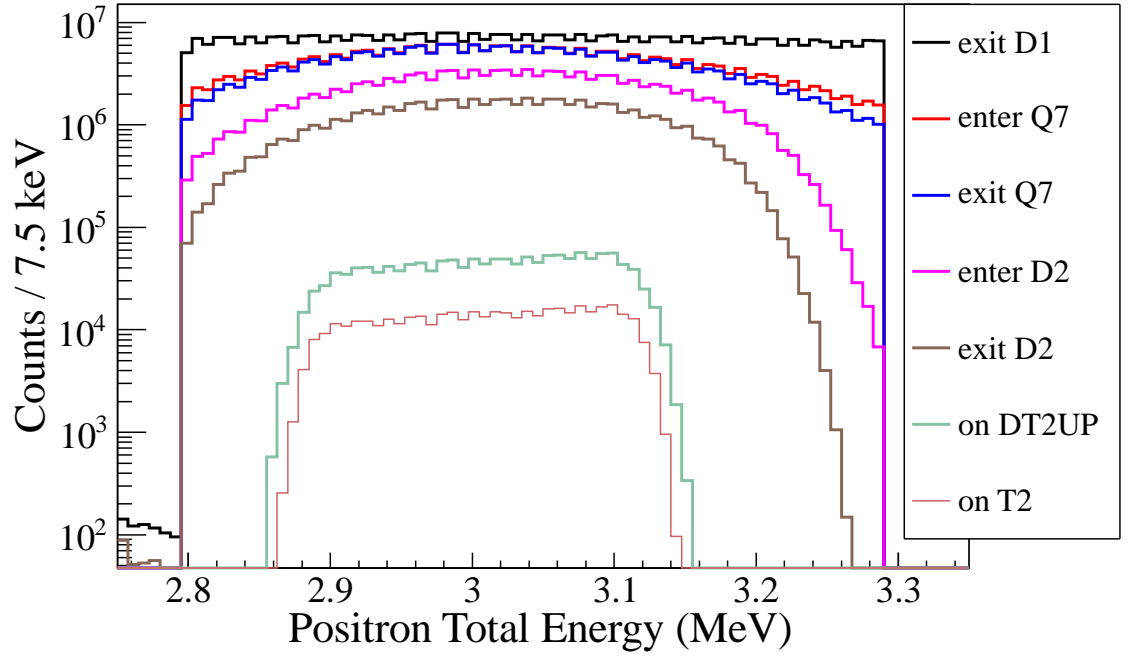
Figure 4.12: Energy distribution of positrons transported when dipoles were set to bend 3 MeV positrons along the beamline.

Table 4.4: Number of 511 keV photons observed by the NaI detectors.

T2 Placement	Exp.	Perp. to Beam	Face Down	Face Down	Face Down	Face Down
Energy	3 MeV	3 MeV	3 MeV	1 MeV	6 MeV	10 MeV
NaI Right	18085	7610	7160	10315	6209	4436
NaI Left	12798	7651	7114	10254	6111	4487
NaI Top Right	7050	7580	12964	12371	14698	10636
NaI Bottom Left	7084	7609	18563	20238	15989	10239
NaI Top	12687	7599	14810	14332	16131	11479
NaI Bottom	18008	7609	18874	20193	16950	11181
NaI Top Left	14632	7656	12818	12268	14812	10735
NaI Bottom Right	18764	7623	18415	20197	16004	10317

4.4 Analysis of the Photon Count Asymmetry in NaI Detectors

The beam right NaI detector observed higher rates that the beam left detector in both the experiment and the simulation. Eight virtual NaI detectors were placed as shown in Figure 4.13 to study this count asymmetry. The orientation of T2 with respect to the incident positron beam was simulated for three cases. In the first case, the photon count rate was predicted by the simulation when the T2 is perpendicular to the beam (its area vector is parallel to the beam). In the second case, T2 was rotated clockwise (starting with the T2 location in the first case) about the x-axis (the axis pointing beam left) by 45° making the upstream side of T2 face downward as shown in Figure 4.13 (a). In the third case, T2 was rotated clockwise about the y-axis (axis points beam up) by 45° so it is facing the beam right NaI detector as shown in Figure 4.13 (b). The setup in the third case is similar to the setup in the experiment and the simulation described in the beginning of this chapter.

The 511 keV photon counts observed by eight virtual NaI detectors for one million positrons are given in Table 4.4 for each configuration. When T2 was placed perpendicular to the incoming positron beam, the 511 keV photons created inside T2 have the same probability to escape from T2 and reach any one of the detectors. As
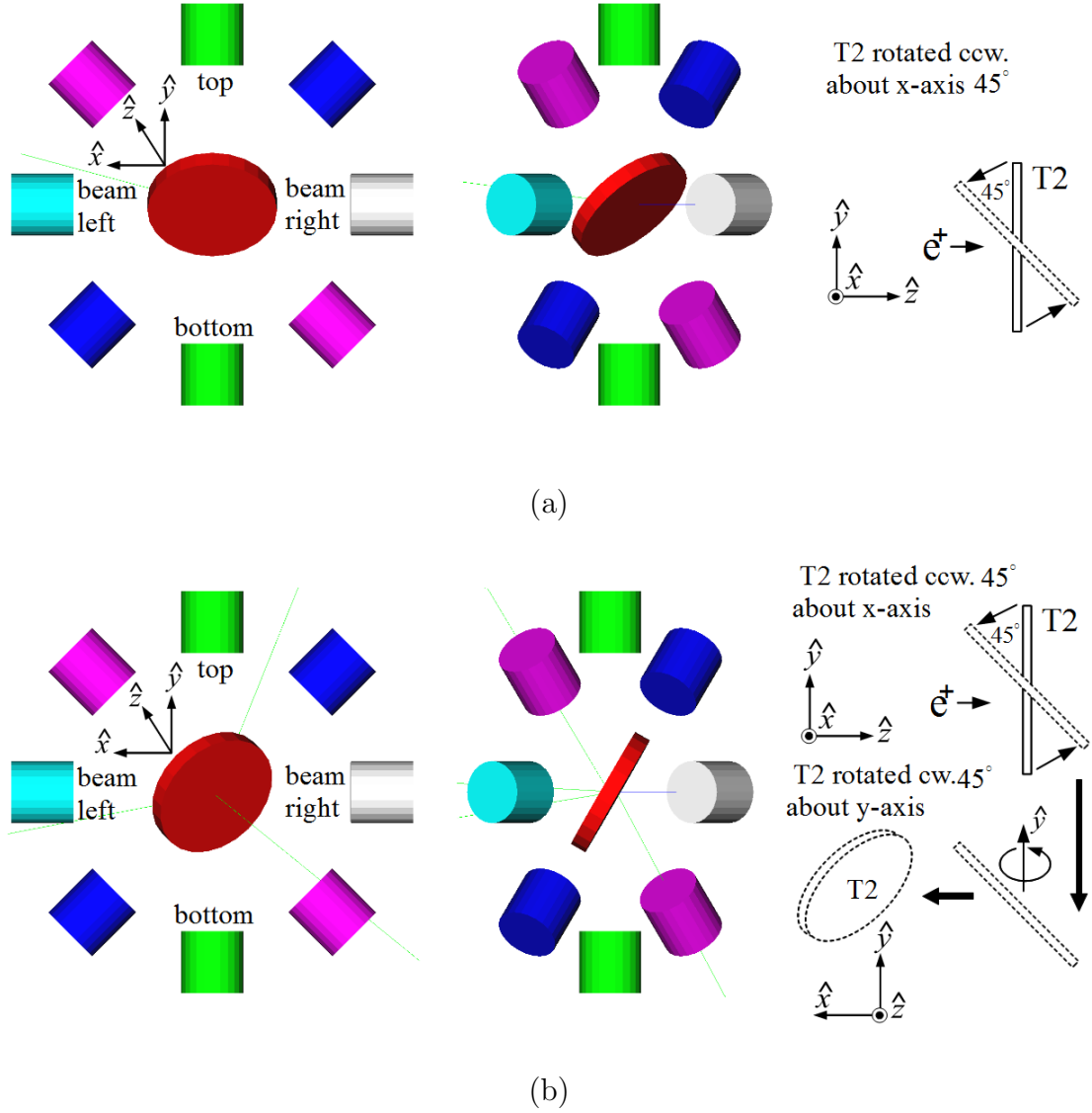
Figure 4.13: NaI detector locations around T2. The positron beam (blue line) is traveling along the z-axis (into the paper in the right figures). (a) T2 was rotated counter-clockwise about the x-axis by 45° positioning the upstream side of the T2 such that it faces the bottom NaI detector. (b) T2 was positioned as in the experiment. It was first rotated to the position as in (a), then it was rotated clockwise about the y-axis by 45°, positioning the upstream side of the T2 such that it faces the beam right NaI detector.

shown in the third column of Table 4.4, all eight detectors observed a similar number of photons. In a separate simulation, T2 was positioned as in the first case and impinged by 1, 3, 6, 10 MeV positrons. The average distance traveled by positrons inside T2 before annihilation was 0.0847 ± 0.0001, 0.3006 ± 0.0004, 0.511 ± 0.001, 0.564 ± 0.008 mm for the four energies respectively. In another GEANT4 simulation, T2 was positioned according to the second case and two virtual NaI detectors were placed on both the top and the bottom of T2. The bottom detector observed more photons than the top one when 511 keV photons were generated 0.3006 mm inside T2 isotropically. Photons are more likely to reach the bottom detector because they would travel through a thinner layer of tungsten to reach it.

In the second case, shown in Figure 4.13 (a), the left and the right NaI detectors had the lowest counts for 3 MeV positrons as shown in the fourth column of Table 4.4. There is less detection probability for a photon traversing T2 in the radial direction towards the left/right detectors than the top/bottom surfaces of T2 due to the amount of material. The average distance traveled by 3 MeV positrons inside T2 before annihilation was 0.3006 ± 0.0004 mm. In this case, positrons annihilated near the upstream face of T2. For this reason, the bottom, bottom right, and bottom left NaI detectors (facing the upstream side of T2) observed more photons than the top, top right, and top left as shown in the fourth column of Table 4.4.

The lower the positron beam energy, the shorter the annihilation depth, and the bigger asymmetry in the counts. As shown in the fourth and fifth columns of Table 4.4, more/less 511 keV photons were observed on the bottom/top detectors with the 1 MeV positron beam than with the 3 MeV. As the positron beam energy increases, as shown in the sixth and seventh columns of Table 4.4, the top and bottom detectors observed a similar number of photons, because positrons annihilate more uniformly inside T2 and the asymmetry in the counts decreases. With the increasing positron beam energy, fewer positrons were annihilated inside T2 and more penetrated through which was shown in the top two rows of Table 4.4.

For the third case, shown in Figure 4.13 (b), the top right and left bottom detectors observed the lowest counts, because a photon would need to travel in the radial

direction to reach these two detectors as shown in the second column of Table 4.4. The right, bottom and bottom right (facing upstream face of T2) observed more photons than the left, top, top left.

According to the simulation, the asymmetry in the photon counts was due to the average positron annihilation depth and the photon attenuation inside T2. Low energy positrons tend to annihilate and produce photon pairs near the incident surface. The created photons are more likely to be detected from the incident surface. In the experiment and the simulation, the right NaI detector was facing the upstream side of T2 and observed more 511 keV photons than the left.

4.5 Quadrupole Triplet Collection Efficiency Study

A G4beamline simulation was carried out to study the collection efficiency of the second quadrupole triplet (Q4, Q5, and Q6). The second quadrapole triplet magnets were set to the similar setting as in the experiment. In this simulation, 5,475,869,400 positrons were generated at DDNT1 and transported to DD1 to study the quadrupole triplet positron collection and transportation efficiency. Six quadrupole current settings of the triplet system were simulated as shown in Table 4.5. For different quadrupole current settings, no significant differences were observed in the number of positrons, transverse beam profiles, and momentum distributions. The ratio of positrons generated at DDNT1 to the ones that enter D1 is 1525:1.

4.6 Systematic Errors Study using Simulation

Different sources of systematic errors in the positron production experiment was studied using G4beamline simulation. The power supply of the magnets might fluctuate ± 0.1 A which will change the magnetic field strength of the magnets. The misalignment of the magnets would also contribute to the systematic error of the

Table 4.5: Quadrupole Triplet System Collection and Transportation Efficiency Data.

Q4	Q5	Q6	Entries	x	σ_x	y	σ_y	P_x	σ_{Px}	P_y	σ_{P_y}	P_z	σ_{P_z}
A	A	A		mm	mm	mm	mm	MeV	MeV	MeV	MeV	MeV	MeV
-1	2	-1	3587220	-0.005	12	0.030	12	3.0×10^{-5}	0.0461	-0.00216	0.04553	3.848	1.875
-2	4	-2	3591423	-0.012	12	0.049	12	2.2×10^{-5}	0.0461	-0.00211	0.04554	3.848	1.875
1	-2	1	3591509	-0.009	12	0.040	12	-1.5×10^{-5}	0.0462	-0.00216	0.04557	3.849	1.876
1	2	1	3589854	-0.005	12	0.034	12	-1.8×10^{-5}	0.0462	-0.00216	0.04556	3.849	1.876
2	-4	2	3592977	-0.007	12	0.032	12	-3.3×10^{-6}	0.0462	-0.00217	0.04549	3.849	1.876
2	4	2	3589495	-0.004	12	0.033	12	3.0×10^{-6}	0.0462	-0.00218	0.04554	3.849	1.875

experiment.

4.6.1 Systematic Error Created by The Uncertainty in The Magnetic Fields Strength of The Magnets

The field strength of the magnets are dependent on the current provided by the power supply. The uncertainty of the magnet power supply is 0.1 A. Systematic errors for the positron counts were estimated by carrying out simulations with different magnetic field settings as shown in Table 4.6.

The magnet settings are indicated in the top three rows of Table 4.6. The transported positron energy is given by the first column. The 511 keV photon pairs counted in coincidence mode (*i.e.* the original count multiplied by 46.42%) for different magnet settings are given in the corresponding columns below. The "Max"/"Min" in the table refers to the Maximum/Minimum magnetic field strength when the magnet coil current is at $I_{\max}/I_{\min}$, where $I_{\max} = I_{\text{def}} + 0.1$ A and $I_{\min} = I_{\text{def}} - 0.1$ A. "def" refers to the default magnetic field strength of the magnet.

The average counts and fractional errors are shown in the last two columns of Table 4.6. The fractional error in the 511 keV photon pair counts is calculated by dividing the standard deviation of counts by the counts in default magnet setting, *i.e.* $\frac{\text{standard deviation of counts}}{\text{counts in default setting}}$.

4.6.2 Systematic Error Introduced by The Misalignment of The Magnets and The Uncertainty in The Electron Beam

The misalignment of the magnets are one of the main sources of systematic error. The 0 and 90 degree beamlines were aligned with a laser beam, while the 45 degree beamline was placed without any reference laser. Therefore, a misalignment was most likely to occur at the 45 degree beamline. The misalignment was estimated to be 5 mm. To study the effect of misalignments from different sources, beam line

Table 4.6: Systematic Error Study: Counts of 511 keV Photon Pairs for Different Magnet Settings.

D1	Max	Min	Max	Min	Max	Max	Min	Min	Def		
Q7	Def	Def	Def	Def	Max	Min	Min	Def	Def		
D2	Max	Min	Def	Def	Def	Def	Def	Def	Def		
Energy (MeV)										Average	Fractional Error
0.765 1.265	12	2	3	1	1	3	3	0	6	4	57.3 %
1.25 - 1.75	95	75	70	86	85	92	129	86	97	90	17.6 %
1.85 - 2.35	674	724	737	769	686	747	803	681	734	728	5.8 %
2.25 - 2.75	781	755	753	759	772	963	794	763	794	793	8.3 %
2.75 - 3.25	739	737	765	752	738	698	738	757	723	739	2.7 %
3.25 - 3.75	713	699	747	712	707	751	718	705	716	719	2.5 %
3.77 - 4.27	690	708	715	676	704	658	706	715	701	697	2.7 %
4.25 - 4.75	627	666	634	646	635	675	637	653	646	646	2.5 %
4.75 - 5.25	558	595	594	603	606	688	582	582	566	597	6.7 %
5.25 - 5.75	513	536	535	522	525	535	518	544	533	529	1.9 %

elements were shifted as shown in Table 4.7. The measured positron to electron ratios were given as well. Among the different sources, the systematic error produced when the first dipole, D1, is misaligned appears to have the largest impact.

Table 4.7: Positron to Electron Ratio When a Single Beamline Element Is Misaligned and the Percent Error Compared to the Ratio When No Misalignment.

Energy (MeV)	45 degree line moved to beam right by 3 mm	percent error
1.02 ± 0.03	$(8.3 \pm 3.4) \times 10^{-17}$	-6.7 %
2.15 ± 0.06	$(7.4 \pm 0.3) \times 10^{-15}$	-26.7 %
3.00 ± 0.07	$(8.1 \pm 0.3) \times 10^{-15}$	-18.7 %
4.02 ± 0.07	$(8.2 \pm 0.3) \times 10^{-15}$	-15.2 %
5.00 ± 0.06	$(7.2 \pm 0.3) \times 10^{-15}$	-7.7 %
Energy (MeV)	D1 raised up by 5 mm	percent error
1.02 ± 0.03	$(3.2 \pm 5.7) \times 10^{-17}$	-64.0 %
2.15 ± 0.06	$(6.1 \pm 0.9) \times 10^{-15}$	-39.6 %
3.00 ± 0.07	$(7.2 \pm 1.0) \times 10^{-15}$	-27.7 %
4.02 ± 0.07	$(5.5 \pm 0.9) \times 10^{-15}$	-43.1 %
5.00 ± 0.06	$(4.8 \pm 0.8) \times 10^{-15}$	-38.5 %
Energy (MeV)	D2 lowered down by 5 mm	percent error
1.02 ± 0.03	$(1.6 \pm 2.3) \times 10^{-17}$	-82.0 %
2.15 ± 0.06	$(6.9 \pm 1.0) \times 10^{-15}$	-31.7 %
3.00 ± 0.07	$(8.6 \pm 1.1) \times 10^{-15}$	-13.7 %
4.02 ± 0.07	$(6 \pm 0.9) \times 10^{-15}$	-38.0 %
5.00 ± 0.06	$(7.7 \pm 1.0) \times 10^{-15}$	-1.3 %
Energy (MeV)	detectors moved up by 3 mm, downstream by 3 mm, and right by 3 mm	percent error
1.02 ± 0.03	$(9.6 \pm 8.1) \times 10^{-17}$	7.9 %

Table 4.7 – *Continued from previous page*

Energy (MeV)		percent error
2.15 ± 0.06	$(7.4 \pm 1.0) \times 10^{-15}$	-26.7 %
3.00 ± 0.07	$(8.2 \pm 1.1) \times 10^{-15}$	-17.7 %
4.02 ± 0.07	$(9.6 \pm 1.2) \times 10^{-15}$	-0.7 %
5.00 ± 0.06	$(7.7 \pm 1.0) \times 10^{-15}$	-1.3 %
Energy (MeV)	T2 moved up by 3 mm, downstream by 3 mm, and right by 3 mm	percent error
1.02 ± 0.03	$(6.4 \pm 6.6) \times 10^{-17}$	-28.1 %
2.15 ± 0.06	$(7.7 \pm 1.0) \times 10^{-15}$	-23.8 %
3.00 ± 0.07	$(7.9 \pm 1.1) \times 10^{-15}$	-20.7 %
4.02 ± 0.07	$(7.9 \pm 1.0) \times 10^{-15}$	-18.3 %
5.00 ± 0.06	$(7.7 \pm 1.0) \times 10^{-15}$	-1.3 %
Energy (MeV)	T2 rotated c.w. about x-axis by 5° and c.c.w. about y-axis by 5°	percent error
1.02 ± 0.03	$(6.4 \pm 6.6) \times 10^{-17}$	-28.1 %
2.15 ± 0.06	$(7.2 \pm 1.0) \times 10^{-15}$	-28.7 %
3.00 ± 0.07	$(6.4 \pm 0.9) \times 10^{-15}$	-35.7 %
4.02 ± 0.07	$(7.2 \pm 1.0) \times 10^{-15}$	-25.5 %
5.00 ± 0.06	$(6.1 \pm 0.9) \times 10^{-15}$	-21.8 %

There are many combinations of magnet misalignments (Q1−Q10, D1, and D1), the "worst case scenario" is considered here to estimate the largest source of systematic error. A "worst case scenario" was created by misaligning the beamline as given in Table 4.8. The results is given in Table 4.9 in terms of the ratio of the number of e^+ detected in coincidence mode by NaI detectors to the number of e^- incident on the T1. Beam line misalignments far beyond what can be reasonably argued indicate drops in positron rate dropped by 60% to 80%. A more realistic misalignment of beamline elements dropped this rate around 20%. Since the chance of the beamline misalignment is large, the systematic error of the simulation is argued to be at least

Table 4.8: Misalignment of The Beam in The Worst Case Scenario.

Beam Element	Placement
D1	raised up by 5 mm
D2	lowered down by 5 mm
45 degree line	shifted to beam right by 3 mm
NaI detectors	raised up by 3 mm, moved 3 mm beam downstream and 3 mm to beam right
T2	raised up by 3 mm, moved 3 mm beam downstream and 3 mm to beam right, rotated clockwise 5° about x-axis and counter clockwise 5° about y-axis

Table 4.9: Positron to Electron Ratio Predicted When Beamline is Misaligned as Given in Worst Case Scenario and the Percent Error Compared to the Ratio When No Misalignment.

Energy (MeV)	Positron to Electron Ratio	percent error
1.02 ± 0.03	$(3.4 \pm 3.5) \times 10^{-18}$	-61.8 %
2.15 ± 0.06	$(1.79 \pm 0.50) \times 10^{-15}$	-83.2 %
3.00 ± 0.07	$(3.39 \pm 0.68) \times 10^{-15}$	-66.9 %
4.02 ± 0.07	$(3.14 \pm 0.66) \times 10^{-15}$	-67.9 %
5.00 ± 0.06	$(2.82 \pm 0.62) \times 10^{-15}$	-64.1 %

around 20%.

Chapter 5

Conclusions and Suggestions

A new High Repetition Rate Linac (HRRL) beamline located in ISU's Physics Department beam lab has been successfully reconstructed to produce and transport positrons to the experimental cell. The electron beam energy profile and emittance of the HRRL were measured using a Faraday cup and an OTR based diagnostic system. The positron production rate was measured for positron energies between 1 and 5 MeV. The results are shown in Figure 5.1 along with the prediction made by a GEANT4 simulation of the beamline.

The production of positrons using an electron linac was done in several steps. First, positrons are emitted from the downstream side of a tungsten target (T1) when electrons impinge on the upstream side and produce photons of sufficient energy to pair produce within the tungsten target. Positrons escaping the downstream side of the target were collected by the quadrupole triplet. The positrons are then deflected by two dipoles in order to measure the positron rate as a function of the positron energy. Positrons that traversed the two dipoles would annihilate in a second tungsten target (T2) producing back-to-back 511 keV photons that were measured using two NaI detectors. The positron rate was measured by requiring a coincidence between both NaI detectors and the electron beam pulse.

The positron beam creation, beam loss in the transportation, and detection process were studied using the simulation package G4beamline and compared to this experiment. The simulated e^+/e^- ratios are shown in Figure 5.1 for the energies measured in this experiment. The simulation includes electron beam generation with the measured electron energy profile, beam losses during transportation, positron annihilation in the tungsten target (T2), and the detection of 511 keV photons in

coincidence by the two NaI detectors. While the simulation result agrees with the experiment in that the peak energy distribution is near 3 MeV, it predicts a higher positron to electron ratio as shown in Figure 5.1.

The simulation was used to study the systematic errors in the experiment. The simulation predicts that a realistic misalignment of the beamline can reduce the e^+/e^- ratios by 20% to 30%. In the worst case scenario, the ratios dropped by 60% to 80%. The systematic errors in the experiment bring it into agreement with the simulation.

The ratio of the positrons contained within the 90 degree beampipe to the 511 keV photons detected in coincidence mode when the dipoles were set to bend 3 MeV positrons is predicted to be 1655:1 by the simulation. The ratio of the positrons on T2 to the 511 keV photons is 620:1 under the same conditions as above. The 3 MeV positron rate measured in the experiment was 0.25 ± 0.2 Hz when the HRRL was operated at a 300 Hz repetition rate, 100 mA peak current, and 300 ns (FWHM) RF macro pulse length. Based on this simulation, a measured 0.25 ± 0.02 Hz coincidence rate by the NaI detectors would correspond to a 155 ± 12 Hz positron rate incident on T2.

In the simulation, the number of positrons collected was insensitive to the quadrupole triplet collection field setting (see section 4.5). The ratio of solid angles subtended by the quadrupole (Q4) and dipole (D1) entrance windows approximated the ratios of positron transported. Quadrupoles focus in one plane and defocus in the other. Thus, one can only collect positrons in one plane while loses occur in the other. Solenoids, on other hand, focus in both planes. A solenoid may be a better option to improve the collection efficiency. Positioning the target T1 at the entrance of the solenoid may be the optimal choice for capturing positrons.
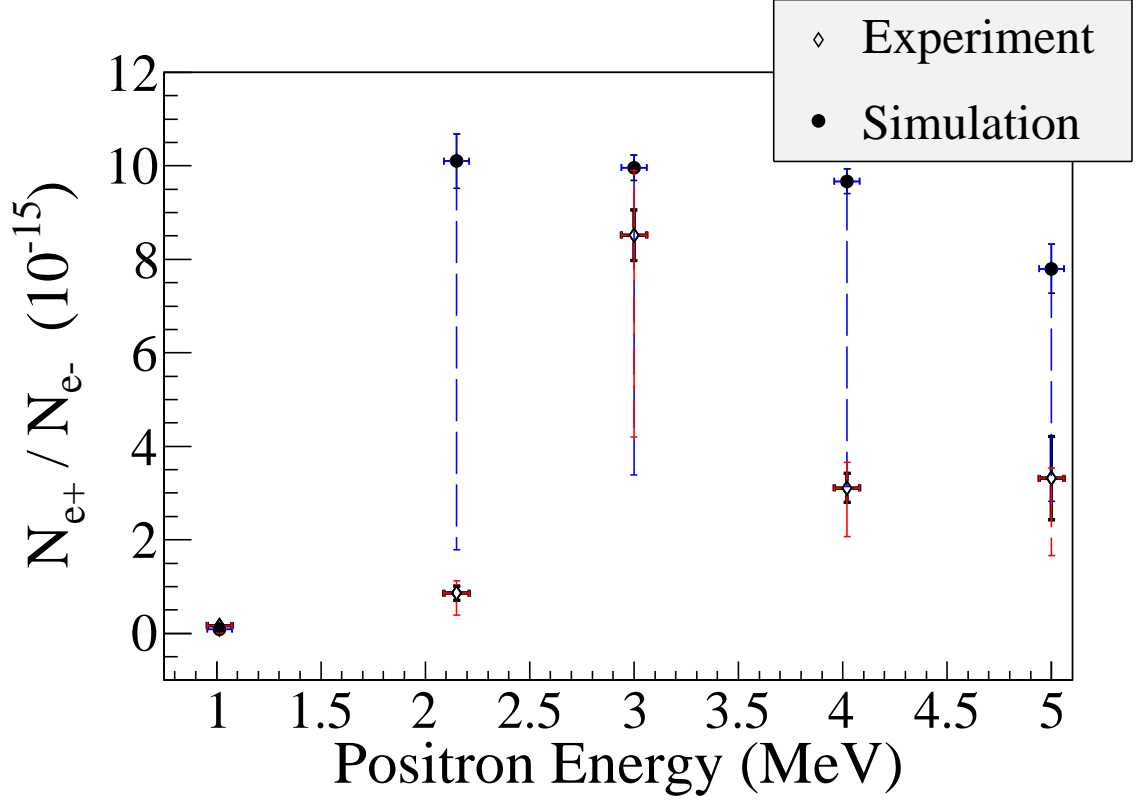
Figure 5.1: Ratio of positrons detected to electrons measured in the experiment (hollow diamond) and simulation (full circle) in coincidence mode. The black solid error bars are statistical and dashed ones are systematic. The systematic errors of experimental measurement are discussed in section 3.4 of Chapter 3 (red dashed lines). The systematics were also studied with simulation (red dashed lines) and described in section 4.6 of Chapter 4.

References

[1] G. Moortgat-Pick, T. Abe, G. Alexander, B. Ananthanarayan, A.A. Babich, V. Bharadwaj, D. Barber, A. Bartl, A. Brachmann, S. Chen, J. Clarke, J.E. Clendenin, J. Dainton, K. Desch, M. Diehl, B. Dobos, T. Dorland, H.K. Dreiner, H. Eberl, J. Ellis, K. Flttmann, H. Fraas, F. Franco-Sollova, F. Franke, A. Freitas, J. Goodson, J. Gray, A. Han, S. Heinemeyer, S. Hesselbach, T. Hirose, K. Hohenwarter-Sodek, A. Juste, J. Kalinowski, T. Kernreiter, O. Kittel, S. Kraml, U. Langenfeld, W. Majerotto, A. Martinez, H.-U. Martyn, A. Mikhailichenko, C. Milstene, W. Menges, N. Meyners, K. Mnig, K. Moffeit, S. Moretti, O. Nachtmann, F. Nagel, T. Nakanishi, U. Nauenberg, H. Nowak, T. Omori, P. Osland, A.A. Pankov, N. Paver, R. Pitthan, R. Pschl, W. Porod, J. Proulx, P. Richardson, S. Riemann, S.D. Rindani, T.G. Rizzo, A. Schlicke, P. Schler, C. Schwanenberger, D. Scott, J. Sheppard, R.K. Singh, A. Sopczak, H. Spiesberger, A. Stahl, H. Steiner, A. Wagner, A.M. Weber, G. Weiglein, G.W. Wilson, M. Woods, P. Zerwas, J. Zhang, and F. Zomer, "Polarized Positrons and Electrons at the Linear Collider", *Phys. Rept.*, **460**, 131-243 (2008).

[2] S. Chemerisov. and C.D. Jonah, "Generation of High Intensity Thermal Positron Beams Using A 20-MeV Electron Linac", in *AIP Conference Proceedings*, **1160**, Newport News, Virginia, 2009, pp. 87-93.

[3] Richard Ley, "Positron production using accelerators", in *Hyperfine Interactions*, **109**, Kluwer Academic Publishers, Newport News, Virginia, 1997, pp. 167-180.

[4] Positron Spectrometer Laboratory at North Carolina State University, *http://www.ne.ncsu.edu/nrp/ips.html*, Intense Positron Beam, 2013-12-05.

[5] H.W. Koch and J.W Motz, "Bremsstrahlung Cross-Section Formulas and Related Data", *Rev. Mod. Phys.*, **31**, 920-955 (1959).

[6] K.S. Krane, *Introductory Nuclear Physics*, John Wiley & Sons, New York, 1988.

[7] NIST, *http://physics.nist.gov/cgi-bin/Xcom/xcom2*, NIST XCOM, 2013-05-03.

[8] M. Conte, and W.W. Mackay, *An Introduction to The Physics of Particle Accelerators*, World Scientific, New York, 2008.

[9] V.L Ginzburg and I.M. Frank, "On The Transition Radiation Theory", *Sov. Phys. JETP*, **16**, 15 (1964).

[10] K.T. McDonald and D.P. Russell, "Methods of Emittance Measurement", *Fron. of Par. Beams Obser. Diag. and Cor.*, **08544**, 1 (1988).

[11] Y. Kim, A. Andersson, M. Dach, R. Ganter, C. Gough C. Hauri, R. Ischebeck, F. Le Pimpec, M. Paraliev, M. Pedrozzi T. Schietinger, V. Schlott, B. Steffen, and A.F. Wrulich, "Low Thermal Emittance Measurements at the Low Emittance Gun (LEG) Test Facility", in *Proc. FEL2008*, **1160**, Gyeongju, Korea, 2008, pp. 110-113.

[12] D.F.G. Benedetti,B. Buonomo, and D. Filippetto, "Emittance Measurement of The DAFNE Linac Electron Beam", *Tech. Rep., DAFNE Tech. Not.*, Frascati, Italy (2005).

[13] S.Y. Lee, *Accelerator Physics*, 2nd ed., World Scientific, Singapore, 2004.

[14] Danfysik, *http://www.danfysik.com/system-5000/27083*, 2013-11-30.

[15] B. Gitter, "Optical Transition Radiation", *Tech. Rep.*, Los Angeles, USA, 1992.

[16] Thorlabs, Inc., *http://www.thorlabs.us/*, 2013-08-08.

[17] CERN, *http://geant4.cern.ch/*, 2013-08-08.

[18] Muons, Inc., *http://public.muonsinc.com/*, 2013-08-08.

[19] Saint-Gobian, *http://www.detectors.saint-gobain.com*, Saint-Gobian Crystals Technical Information Notes, 2013-06-11.

[20] F.J. Decker, "Beam Distribution Beyond RMS", in *6th Workshop on Beam Instrumentation*, Vancouver, Canada, (1994). pp. 1-7.

[21] The MathWorks, Inc., *http://www.mathworks.com/*, 2013-10-31.

[22] *http://www.ionbeams.com/*, ISYS Ion Beam Systems Inc., 2013-11-23.

Appendix A

The Electron Beam Energy Scan

A.1 Measured Data

The HRRL electron beam energy was scanned using a dipole magnet by bending the electron beam by 45° to a Faraday cup. The dipole magnet coil current and the electron beam current observed with the Faraday cup are given in the following table.

Table A.1: HRRL Electron Beam Energy Scan Using Dipole.

Dipole Magnet Coil Current (A)	Faraday Cup Current (mA)	Electron Beam Energy (MeV)
8.0	0.50	4.3119
9.0	0.60	4.8896
10.0	0.67	5.4570
11.0	0.72	6.0141
12.0	0.75	6.5610
13.0	0.83	7.0975
14.0	0.90	7.6238
15.0	1.11	8.1399
16.0	1.33	8.6456
17.0	1.62	9.1411
18.0	1.90	9.6262
19.0	2.45	10.1012
20.0	3.36	10.5658

Continued on next page

Dipole Magnet Coil Current (A)	Faraday Cup Current (mA)	Electron Beam Energy (MeV)
21.0	4.82	11.0201
22.0	6.58	11.4642
22.2	7.88	11.5518
22.5	9.24	11.6824
22.7	10.00	11.7690
23.0	10.20	11.8980
23.1	11.20	11.9408
23.2	11.56	11.9836
23.3	13.04	12.0262
23.5	13.20	12.1111
23.8	13.04	12.2377
24.0	13.48	12.3216
24.2	12.36	12.4050
24.5	11.24	12.5295
24.7	10.20	12.6119
25.0	10.28	12.7348
25.1	8.60	12.7756
25.2	6.92	12.8162
25.5	6.20	12.9376
25.7	4.84	13.0180
26.0	3.64	13.1378
26.5	1.82	13.3354
27.0	1.28	13.5305
28.0	0.56	13.9129
29.0	0.36	14.2850

Table A.1 – *Continued from previous page*

Dipole Magnet Coil Current (A)	Faraday Cup Current (mA)	Electron Beam Energy (MeV)
30.0	0.36	14.6469

A.2   MATLAB Script - Asymmetric Gaussian Fit to Energy Distribution

The main script "EnFitAssymGaus.m" loads data and calls function "Assym-GauDevSum.m" for super Gaussian fit function. Once fit results obtained, It plots the data and the super Gaussian fit.

A.2.1   Subscript "EnFitAssymGaus.m"

```
clear
clc
load En_vs_I_26Apr2012.txt;
I = En_vs_I_26Apr2012(:,2);
En  = En_vs_I_26Apr2012(:,3);
En_er = En*0.01;
I_er = En_vs_I_26Apr2012(:,4);
[NumPoints, row] =  size(En);
a(1) = 1*max(I);
a(2) = 1.*mean(En);
a(3) = 1*std(En);
a(4) = 1*std(En);
a(5) = 0.3*max(I);
a(6) = 0.9*mean(En);
```

```
a(7) = 0.87*std(En);
a(8) = 0.5*std(En);
%------------------------ Fit ------------------------
opts = optimset('TolX',1e-4,'MaxFunEvals',10000,'MaxIter',10000,
'Display','on');
[par,fval,flag,err] = fminsearch(@Assym_Gau_over_linear_devsum,a,
opts,En,I);
%-----------------------------------------------------
sigma = (par(3)+ par(4))/2;
Es = ( par(4) -par(3) )/( par(3)+par(4) );
rms = sigma*sqrt(1+(2-8/pi)*Es^2);
skew = Es*sqrt(8/pi)*(1+(16/pi-5)*Es^2);
sigma2 = (par(7)+ par(8))/2;
Es2 = ( par(8) -par(7) )/( par(7)+par(8) );
rms2 = sigma2*sqrt(1+(2-8/pi)*Es2^2);
skew2 = Es2*sqrt(8/pi)*(1+(16/pi-5)*Es2^2);
%plot(En,I), hold on;
Ene=4:0.01:15;
Mom=sqrt(Ene.^2-0.510998910^2);
%[Ene',Mom']
[row,col] = size(Ene);
signe = sign(Ene-par(2));
signe2 = sign(Ene-par(6));
%signe
%size(signe)
set(axes,'FontSize',16)
errorbar(En,I,I_er,'MarkerSize',30,'Marker','.','LineStyle','none',...
    'LineWidth',3,...
    'DisplayName','Data Points',...
    'Color',[0 0 0]);
```

```matlab
hold on
for i=1:col
Gau_fit(i)=par(5)*exp( -0.5*((Ene(i)-par(6))/(sigma2*(1+signe2(i)
*Es2)))).^2) + par(1)*exp( -0.5*((Ene(i)
-par(2))/(sigma*(1+signe(i)*Es)))).^2);
end
plot(Ene,Gau_fit,'k','LineWidth',2); %plot fit
legend('Data', 'Fit');
%set(legend,'Position',[0.34 0.68 0.1 0.1]);
set(legend,'FontSize',40);
set(legend,'FontName','Times New Roman');
hy = ylabel('I_{FC} (mA)','FontSize',40,'FontName','Times New Roman');
hx = xlabel('En (MeV)','FontSize',40,'FontName','Times New Roman');
fit=title({'Electron Beam Energy Spread';'at 12 MeV'});
set(fit,'FontSize',32,'FontWeight','bold','FontName','Times New
Roman');
%axis([0 0.55 2.6 3.65]); %axis([xmin xmax ymin ymax])
%Create axes
%axes('FontSize',40,'FontName','Times New Roman');
%delete('Gaussian_fit.png')
%saveas(fit,'Gaussian_fit.pdf','pdf');
saveas(fit,'Gaussian_fit.eps','epsc');
saveas(fit,'Gaussian_fit.png','png');
drawnow
fprintf('\n\n total events = %.f\n',sum(Gau_fit*100));
fprintf('\n Amplitude = %.5f, mean = %.5f, sigma_L = %.5f,
sigma_R = %.5f\n\n',  par(1), par(2), par(3), par(4));
fprintf(' Sigma = %.5f, Es = %.5f \n\n',  sigma, Es);
fprintf(' rms = %.5f, skew = %.5f \n\n',  rms, skew);
fprintf(' Amplitude2 = %.5f, mean2 = %.5f, sigma_L2 = %.5f,
```

```
sigma_R2 = %.5f\n\n',  par(5), par(6), par(7), par(8));

fprintf(' Sigma2 = %.5f, Es2 = %.5f \n\n',  sigma2, Es2);

fprintf(' rms2 = %.5f, skew2 = %.5f \n\n',  rms2, skew2);
```

A.2.2   Subscript "AssymGauDevSum.m"

```
function chisq = Assym_Gau_devsum(a,X,Y)

sigma = (a(3)+a(4))/2;

Es = ( a(4)-a(3) )/( a(3)+a(4) );

signe = sign(X-a(2));

sigma2 = (a(7)+a(8))/2;

Es2 = ( a(8)-a(7) )/( a(7)+a(8) );

signe2 = sign(X-a(6));

[col,row] = size(X);

for i=1:col

Gau(i) = a(5)*exp( -0.5*((X(i)-a(6))/(sigma2*(1+signe2(i)*Es2))).^2 )

+ a(1)*exp( -0.5*((X(i)-a(2))/(sigma*(1+signe(i)*Es))).^2 );

end

csq = (Y - Gau').^2;

chisq = sum(csq);

return
```

Appendix B

MATLAB Scripts for Calculating Emittance

The emittance of the HRRL was analyzed using MATLAB. The main script "Emit_Calc.m" loads and digitize electron beam images. Then, 2D beam is projected to x and y axes and the rms values of the projections are calculated by fitting super Gaussians using the subscript "SupGau_devsum.m". After that, the rms values are sent to another subscript "Emit_Parabola_Fit_kl_XProjection". "Emit_Parabola_Fit_kl_XProjecti fits parabolic functions, plots the fit and calculates the emittance and Twiss parameters.

B.1   Emittance Calculator

```
% Emit_Calc.m
% April-2011, Sadiq Setiniyaz
clc;
clear
me = 0.511;      % Electron rest mass in MeV
En = 14.9985 ;   % Enter beam energy here in MeV unit
En_er = En*0.1; % Assume 5% error on Energy
L = 0.08;        % Pole face is 8 cm long in z direction.
R_Bore = 0.0254;% Radius of the Bore aperture = center to
                 % pole face = 1 inch.
I_start=-3.0; % Scan starting current
I_increment=0.2;
```

96

```matlab
scan_current_number=31; % do 13 scan.
scan_times=7;
%for ii = 1:scan_step
%I(ii) = I_start + (ii-1)*I_increment;
%end
p = sqrt(En*En - me*me)/1000;% e- momentum in GeV/c
% Enter the distance from the center of the quad to the screen
S12=3.1;%(in m unit) S12(q4)=1.875 cm. S12(q1)=3.10 cm
erS12 = 0.005; % assume 51 mm error.
%Enter calibration here:
calibration_x=0.04327*0.001; %m/px
calibration_y=0.04204*0.001; %m/px
er_calibration_x=0.00016*0.001;
er_calibration_y=0.00018*0.001;
disp('Reading image ...')
%Get image for background (RF is on and gun is off).
bg1 = imread('Scan_1\RF_on_Gun_off_bg.bmp');
bg2 = imread('Scan_2\RF_on_Gun_off_bg.bmp');
bg3 = imread('Scan_3\RF_on_Gun_off_bg.bmp');
bg4 = imread('Scan_4\RF_on_Gun_off_bg.bmp');
bg5 = imread('Scan_5\RF_on_Gun_off_bg.bmp');
bg6 = imread('Scan_6\RF_on_Gun_off_bg.bmp');
bg7 = imread('Scan_7\RF_on_Gun_off_bg.bmp');
% Averaging background.
bg = (bg1+bg2+bg3+bg4+bg5+bg6+bg7+bg7+bg7)/7;
imd_bg = double(bg(:,:,1));


% Set path for different folders that have beam image.
for ii=1:scan_times
switch ii
```

```matlab
    case 1
        addpath(genpath('\Scan_1'));
    case 2
        addpath(genpath('\Scan_2'));
    case 3
        addpath(genpath('\Scan_3'));
    case 4
        addpath(genpath('\Scan_4'));
    case 5
        addpath(genpath('\Scan_5'));
    case 6
        addpath(genpath('\Scan_6'));
    case 7
        addpath(genpath('\Scan_7'));
end
% Read OTR images.
for scan = 1:scan_current_number;
    thisfilename=ii;
    imNo = ii;
    I(scan) = I_start + (scan-1)*I_increment;
    switch scan
        case 1
% Devide the effetive length by 100 to convert to meter unit.
            im = imread('negative\11.bmp');
            tifname='11';
            L_ef(scan) = 9.95/100;
            Er_L_ef(scan) = 0.17/100;
        case 2
            im = imread('negative\12.bmp'); % reading 1.png
            tifname='12';
```

```matlab
                L_ef(scan) = 9.91/100;

                Er_L_ef(scan) = 0.16/100;

            case 3

                im = imread('negative\13.bmp');

                tifname='13';

                L_ef(scan) = 9.91/100;

                Er_L_ef(scan) = 0.16/100;
% Here, just loeaded for three images as example
    end

    sg = im;                    % Reading 1.png
imd_sg = double(sg(:,:,1));
pic = (imd_sg-imd_bg);      % subtrac background


% Noise Cleaning: Getting red of the dead pixels.
% If there is sudden increase in the pixel brightness,
% then use the pixel brightnesss of the earlier pixel.
for i = 3:768
for j = 3:576
    if pic(j,i)>500
        pic(j,i)=pic(j-1,i);
    elseif pic(j,i)-pic(j-2,i)>20
            pic(j,i)=pic(j-1,i);
    end
end
end
% Determine image size in pixels.
dim=size(pic);
dim_x = dim(1);
dim_y = dim(2);
xunit='m';
```

```matlab
yunit='m';
% Beam transverse profiles.
profx = sum(pic,1); % make x projection
profy = sum(pic,2)';% make y projection
xbins=size(profx);
ybins=size(profy);
x=(1:1:xbins(2));
y=(1:1:ybins(2));
% Set Gaussian fit range.
xl = 1;
xr = 766;
yl = 1;
yr = 576;
%plot(x,profx,'k'); % Checking.
%hold on; % Checking.
%plot(y,profy,'k'); % Checking.
%hold on; % Checking.
% Initialize fit parameters.
$a1=base. a2=amplitude. a3=mean. a4=sigma_0. a5=N.
a1 = 100;
a2 = 7700;
a3 = 280;
a4 = 39;
a5 = 1;
% super gaussian.
% SupGau = a(1)+a(2)*exp(-abs(X-a(3))/(a(4))).^a(5);
a0 = [a1,a2,a3,a4,a5]; % Putting the parameters together.
% Setting fit criteria and use fminsearch optimization.
opts=optimset('TolX',1e-4,'MaxFunEvals',10000,'MaxIter',10000,
'Display','on');
```

```matlab
% Pass fit parameters to SupGau_devsum.
[fitpara_x,fval_x,flag_x,err_x]=fminsearch(@SupGau_devsum,a0,
opts,x,profx);
[fitpara_y,fval_y,flag_y,err_y]=fminsearch(@SupGau_devsum,a0,
opts,y,profy);
% Get the fit parameters of x profile.
base_x = fitpara_x(1);
amplitude_x = fitpara_x(2);
peak_center_x = fitpara_x(3);
sig0_x = fitpara_x(4);
N_x = fitpara_x(5);
sig_x(scan,imNo) = sig0_x*(pi/2).^(2/fitpara_x(5)-1);
% Get the fit parameters of y profile
base_y = fitpara_y(1);
amplitude_y = fitpara_y(2);
peak_center_y = fitpara_y(3);
sig0_y = fitpara_y(4);
N_y = fitpara_y(5);
sig_y(scan,imNo) = sig0_y*(pi/2).^(2/fitpara_y(5)-1);
% Printing out parameters to check.
string_x = [
    num2str(I(scan),'  %2.2f'),'     ', ...
    num2str(imNo,'%d'),'        ', ...
    num2str(base_x,'%12.2f'),'        ', ...
    num2str(amplitude_x,'%12.f'),'          ', ...
    num2str(peak_center_x,'%12.2f'),'        ', ...
    num2str(N_x,'%12.4f'),'     ', ...
    num2str(sig0_x,'%12.2f'),'         ', ...
    num2str(sig_x(scan,imNo),'%12.2f'),'     ', ...
    ];
```

```
%disp(string_x);
string_y = [
    num2str(I(scan),'  %2.2f'),'      ', ...
    num2str(imNo,'%d'),'        ', ...
    num2str(base_y,'%12.2f'),'        ', ...
    num2str(amplitude_y,'%12.f'),'          ', ...
    num2str(peak_center_y,'%12.2f'),'        ', ...
    num2str(N_y,'%12.4f'),'     ', ...
    num2str(sig0_y,'%12.2f'),'        ', ...
    num2str(sig_y(scan,imNo),'%12.2f'),'      ', ...
    ];
%disp(string_y);
%sig
%plot(x,profx,'k'); % Plot to check.
%hold on;
%plot(y,profy,'k');
%hold on;
% Construct fit curve from the fit parameters.
y_fit_x = fitpara_x(1)+fitpara_x(2)*exp( -0.5*(abs(x
-fitpara_x(3))/(fitpara_x(4))).^fitpara_x(5) );
y_fit_y = fitpara_y(1)+fitpara_y(2)*exp( -0.5*(abs(y
-fitpara_y(3))/(fitpara_y(4))).^fitpara_y(5) );
%plot(x,y_fit_x,'r');
%plot(y,y_fit_y,'r');
drawnow
end
end
for scan=1:scan_current_number
% Find mean and standar deviation.
sig_mean_x(scan) = mean(sig_x(scan,:));
```

```
sig_mean_y(scan) = mean(sig_y(scan,:));
sig_x_er(scan)   = std(sig_x(scan,:));
sig_y_er(scan)   = std(sig_y(scan,:));
% Converting from pixels to length (in m unit).
sig_mean_x(scan)=sig_mean_x(scan)*calibration_x; %
sig_mean_y(scan)=sig_mean_y(scan)*calibration_y; %
sig_x_er(scan)= sqrt((sig_x_er(scan)*calibration_x).^2 +
(sig_mean_x(scan)*er_calibration_x).^2);
sig_y_er(scan)= sqrt((sig_y_er(scan)*calibration_y).^2 +
(sig_mean_y(scan)*er_calibration_y).^2);
% Find squared sigma.
sig_sqr_x(scan) = sig_mean_x(scan)*sig_mean_x(scan);
sig_sqr_x_er(scan) = 2*sig_mean_x(scan)*sig_x_er(scan);
sig_sqr_y(scan) = sig_mean_y(scan)*sig_mean_y(scan);
sig_sqr_y_er(scan) = 2*sig_mean_y(scan)*sig_y_er(scan);
%I(scan) = I_start + (scan-1)*I_increment;
%plot(I,sig_mean,'r');
%Get the quarupole strength and error from the dipole current.
k1(scan) =0.2998*(3.6*0.0001+1945*0.000001*I(scan))/(0.0254*p);
k1_Er(1) =0.2998*((3.6+1.3)*0.0001+(1945+2)*0.000001*I(scan))/
(0.0254*p);
k1_Er(2) =0.2998*((3.6-1.3)*0.0001+(1945+2)*0.000001*I(scan))/
(0.0254*p);
k1_Er(3) =0.2998*((3.6+1.3)*0.0001+(1945-2)*0.000001*I(scan))/
(0.0254*p);
k1_Er(4) =0.2998*((3.6-1.3)*0.0001+(1945-2)*0.000001*I(scan))/
(0.0254*p);
er_k1(1)=abs(k1(scan)-k1_Er(1));
er_k1(2)=abs(k1(scan)-k1_Er(2));
er_k1(3)=abs(k1(scan)-k1_Er(3));
```

```
er_k1(4)=abs(k1(scan)-k1_Er(4));
k1_er(scan)=max(er_k1);
k1L(scan) = L_ef(scan)*k1(scan); %k1*L
er_k1L(scan) = sqrt((L_ef(scan)*k1_er(scan) )^2+(Er_L_ef(scan)
*k1(scan))^2);
% Put the parameters together to pass to parabolic fits
FitDatX = [k1L',er_k1L',sig_sqr_x',sig_sqr_x_er'];
FitDatY = [k1L',er_k1L',sig_sqr_y',sig_sqr_y_er'];
end
% Save and print data.
X_fit_data = fopen('X_fit_data.txt','w');
Y_fit_data = fopen('Y_fit_data.txt','w');
%fprintf(X_fit_data,'%4f %4f %4f %4f \n',k1L(16:31)',
er_k1L(16:31)',sig_sqr_x(16:31)*10^6',sig_sqr_x_er(16:31)*10^6'
);
%fprintf(Y_fit_data,'%4f %4f %4f %4f \n',k1L(2:15)',
er_k1L(2:15)', sig_sqr_y(2:15)*10^6', sig_sqr_y_er(2:15)*10^6');
fprintf(X_fit_data,'%4f %4f %4f \n',k1L(16:31)',
sig_sqr_x(16:31)'*10^6,sig_sqr_x_er(16:31)'*10^6);
fprintf(Y_fit_data,'%4f %4f %4f \n',k1L(2:15)',
sig_sqr_y(2:15)'*10^6,sig_sqr_y_er(2:15)'*10^6);
fclose(X_fit_data);
fclose(Y_fit_data);
% Converting to cgs (mm and mrad) units.
[k1L(16:31)' sig_sqr_x(16:31)'*10^6 sig_sqr_x_er(16:31)'*10^6]
[k1L(2:15)' sig_sqr_y(2:15)'*10^6 sig_sqr_y_er(2:15)'*10^6]
% Pass data to calculate emittance/Twiss parameters.
Emit_Parabola_Fit_kl_XProjection(k1L(16:31),
er_k1L(16:31),sig_sqr_x(16:31)*10^6,
sig_sqr_x_er(16:31)*10^6,me,En,En_er,S12,erS12,16);
```

```
Emit_Parabola_Fit_kl_YProjection(k1L(2:15) ,er_k1L(2:15),
sig_sqr_y(2:15)*10^6, sig_sqr_y_er(2:15)*10^6, me,En,En_er,S12,
erS12,14);
```

B.2   Super Gaussian Fit

```
function chisq = SupGau_devsum(a,X,Y)
% a(1)=base, a(2)=amplitude, a(3)=mean, a(4)=sigma_0, a(5)=N.
% N=2: nomal Guassian. N<2: super Gaussian (sharp top).
% N>2: Flat top shape Gaussian.
SupGau = a(1)+a(2)*exp( -0.5*(abs(X-a(3))/(a(4))).^a(5) );
csq = (Y - SupGau).^2;
chisq = sum(csq);
return
```

B.3   Parabolic Fit

```
function varargout = Emit_Parabola_Fit_kl_XProjection(x,erx,y,
ery,me,En,En_er,S12,erS12,NumPoints)
order = 2; % second order fit
ParNum = order + 1;
% finding row matrix beta
for k=1:ParNum
for i=1:NumPoints
    f(k)=power(x(i),k-1);
    %fprintf('   i=%d  f(%d)=%g \t',i,k,f(k));
    beta_element(k,i)=y(i)*f(k)/(ery(i)*ery(i));
    %fprintf('y(i=%d)=%g ery(i=%d)=%g \n',i,y(i),i,ery(i));
    %fprintf('beta(k=%d,i=%d)=%g \n',k,i,beta_element(k,i));
    beta(k)=sum(beta_element(k,:));
```

```matlab
        %fprintf('beta_element(%d,%d)=%g
        %beta(%d)=%g\n',k,i,beta_element(k,i),k,beta(k));
end
end
%beta % Print to check.
% finding matrix alpha
for k=1:ParNum
for l=1:ParNum
    for i=1:NumPoints
        f(k)=power(x(i),k-1);
        f(l)=power(x(i),l-1);
        alpha_element(k,l,i)=f(k)*f(l)/(ery(i)*ery(i));
        alpha(k,l)=sum(alpha_element(k,l,:));
        %fprintf('alpha_element(%d,%d,%d)=%g alpha(%d,%d)=%g\n',
        k,l,i,alpha_element(k,l,i),k,l,alpha(k,l));
    end
end
end
%alpha  % Print to check.
%To find fit parameters, need to invert matrix alpha.
alpha_invert = inv(alpha);
%alpha_invert   % Print to check.
% The fit is y = a(1) + a(2)*x + a(3)*x*x
%fit parameters by matrix inversion method
parameter = beta*alpha_invert; %a(l)=parameter(l)
%parameters   % Print to check.
fit_m_inver = parameter(1) + parameter(2)*x + parameter(3)*x.*x;
% error on the parameters
er_a = sqrt(diag(alpha_invert));
%fit parameters by MatLab
```

```
par = polyfit(x,y,2);
%par    % Print to check.
fit_MatLab = par(3) + par(2)*x + par(1)*x.*x;
% Get constants in the parabolic function.
gamma = En/me;
er_gamma = En_er/me;
beta = sqrt(1-1/gamma^2);
er_beta = er_gamma/(gamma^3*beta);
A=parameter(3);
B=-parameter(2)/(2*A);
C=parameter(1)-A*B^2;
erA = er_a(3);
erB = sqrt( (-er_a(2)/(2*A))^2 + (parameter(2)*erA/(2*A^2))^2 );
erC = sqrt((er_a(1))^2 + (-B^2*erA)^2 + (-2*A*B*erB)^2);
%fprintf('A=%g+-%g  B=%g+-%g  C=%g+-%g\n',A,erA,B,erB,C,erC);
% Calculate emittance and Twiss parameters
emit = sqrt(A*C)/((S12)^2);
er_emit = sqrt((1/2*A^(-1/2)*A^(1/2)*erA/(S12)^2)^2 +
(1/2*A^(1/2)*A^(-1/2)*erC/(S12)^2)^2+( 2*sqrt(A*C)*erS12/
(S12)^3)^2);
emit_n = emit*gamma;
er_emit_n = sqrt((emit*er_gamma*beta)^2+(emit*gamma*er_beta)^2+
(er_emit*gamma*beta)^2);
beta_func = sqrt(A/C);
er_beta_func = sqrt( (1/2*sqrt(1/(A*C))*erA)^2 +
(-1/2*sqrt(A/C^3)*erC)^2 );
alpha_func = beta_func*(B + 1/S12);
er_alpha_func = sqrt(((B+1/S12)*er_beta_func)^2 +
(beta_func*erB)^2 + (-beta_func*erS12/(S12)^2)^2 );
figure(1)
```

```
% Plot the parabolic function.
set(axes,'FontSize',40)
pardat = errorbar(x,y,ery,'MarkerSize',30,'Marker','.','
LineStyle','none',...
'LineWidth',3,...
'DisplayName','Data Points',...
'Color',[0 0 1]);
hold on
%Plot fit done by matrix inversion method.
parfit_m_inver = plot(x,fit_m_inver,'r');
set(parfit_m_inver,'LineWidth',3);
legend('Data','Fit');
set(legend,'Position',[0.73 0.75 0.1 0.1]);
set(legend,'FontSize',40);
set(legend,'FontName','Times New Roman');
hx = xlabel('k_{1}L (m^{-1})','FontSize',48,'FontName','Times
New Roman');
hy = ylabel('\sigma^2_x (mm^2)','FontSize',48,'FontName','Times
New Roman');
box off; % remove the top and right axes
%set(gca,'ticklength',4*get(gca,'ticklength'));
set(gca,'ticklength',[0.06 0.9]);
fit=title('');
%fit=title('15.6 MeV, X-Projection: k_{1}L vs \sigma^2');
set(fit,'FontSize',24,'FontWeight','bold','FontName','Times New
Roman');
axis([-0.05 0.55 2.3 3.2]); %axis([xmin xmax ymin ymax])
%axis('FontSize',28);
% Save plot.
saveas(fit,'Emit_Calc_plots\par_fit_x.fig','fig');
```

```
saveas(fit,'Emit_Calc_plots\par_fit_x.eps','epsc');
saveas(fit,'par_fit_x.eps','epsc');
saveas(fit,'Emit_Calc_plots\par_fit_x.png','png');
drawnow
fprintf('x-projection:\n\nemit=%.3f +- %.3f mm*mrad, emit_norm
=%.2f +- %.2f mm*mrad \n\n', emit, er_emit, emit_n, er_emit_n);
fprintf('beta=%.2f +- %.2f m, alpha=%.2f +- %.2f rad \n\n',
beta_func, er_beta_func, alpha_func, er_alpha_func);
fprintf('parabola fit for y-projection (y in mm unit): \n y =
(%.5f +-%.5f) + (%.5f+-%.5f)*x + (%.5f+-%.5f)*x.*x \n\n',
parameter(1),er_a(1), parameter(2),er_a(2),
parameter(3),er_a(3));
return
```

Appendix C

HRRL Operation

This is courtesy of the Idaho Accelerator Center.

C.1 HRRL Start Up Procedure

1. Turn on one of the two water pumps for the cooling system. Use the pumps alternatively when running for multiple days. Turn on all three chillers.

2. First turn on the breaker on the wall, then turn on "ISA" water skid system and check for leaks (see Figure C.1).

3. Turn on the modulator by unlocking the padlock on SCR enclosure (see Figure C.2).

4. Turn on the HRRL electron gun driver and enable high voltage. It takes 18 minuets to warm up the filament for the beam operation. Turn on the fans inside accelerator cell (see Figure C.3).

5. Press the "Startup" button on the "PanelMate" touchscreen, located at control rack, and wait for the 900 second (15 minuet) countdown (see Figure C.4).

6. Turn on all the power supplies for magnets and klystron (see Figure C.6).

7. Turn on HP pulse generator and enable the output.

8. Make sure the modulator is on. Open the door to thyratron and verify the two lights at the corner of the box are on.

9. Fill the wave guide with SF_6 gas up to 35 lbs. Turn on the fan to the klystron waveguide (see Figure C.5).

10. Turn on the switch on the building interlock system to enable the beam operation. Turn on the key for interlock system. Press all three red buttons in accelerator cell and verify no body is in the accelerator cell. Close the gate to the

accelerator cell.

11. After 900 second countdown, set the repetition rate to lower range (around 10 Hz), turn the core bias on, and turn the key (to accelerator control) to on position.

12. Press the "HV ON" on the touchscreen, wait for 10 seconds, then press "BEAM ON" on the screen. This will start the electron beam.

Figure C.1: ISA water skid system.

C.2   HRRL Shutdown Procedure

1. Turn off and remove the key (to accelerator control).

2. Press "shutdown" on the "PanelMate" touchscreen.

3. Turn off all the power supplies for magnets and klystron.

4. Turn down both potentiometers that control high voltage and grid drive for the electron gun grid driver.

5. Turn off HP pulse generator.

6. Turn off building interlocks and remove the key.

Figure C.2: SCR enclosure and the padlock.
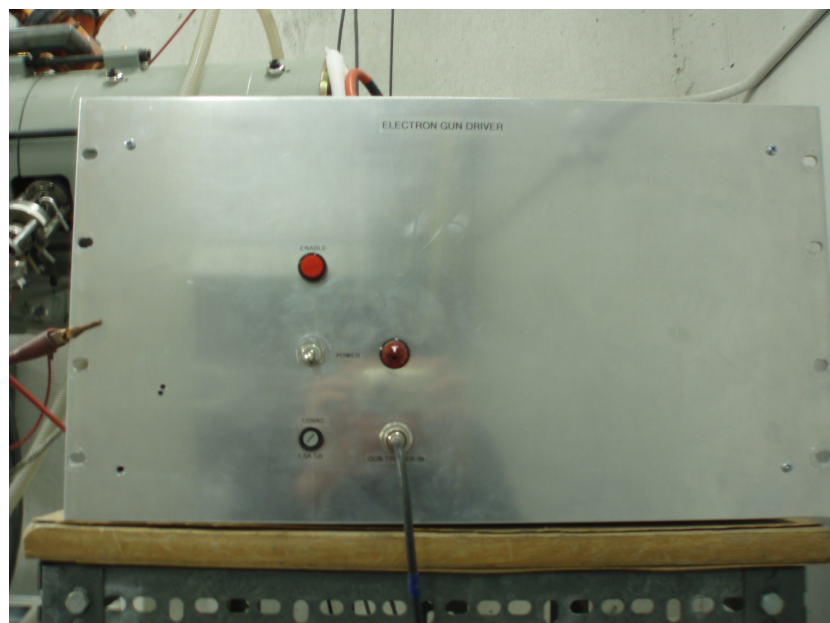
Figure C.3: HRRL electron gun driver high voltage power supply.

Figure C.4: "PanelMate" touchscreen.
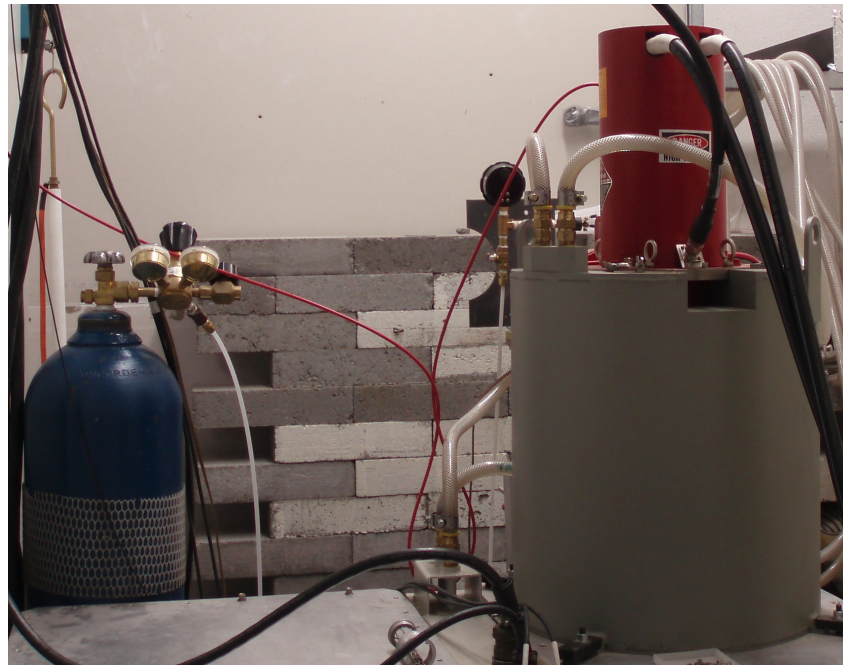
Figure C.5: SF$_6$ gas tank and Klystron.
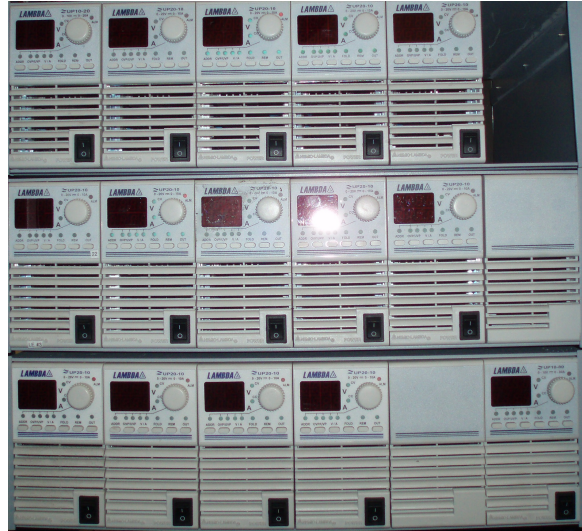
Figure C.6: Power supplies for magnets and Klystron. (a) Power supply for solenoids (top and bottom) and klystron (middle). (b) Power supply for dipoles and quadrupoles.

7. Turn off the electron gun driver. Turn off the two fans in the accelerator cell.

8. Turn off the modulator by locking padlock on SCR enclosure.

9. Wait for the fans (in the modulator room) to turn off (about 15 minuets).

10. Make sure the modulator is off. Open the door to thyratron and verify the two lights at the corner of the box are off.

11. Turn off "ISA" water skid system and turn off the breaker.

12. Turn off the chillers and then the water pump.

C.3   HRRL Electron Beam Tuning

1. Turn off all the quadrupoles and dipoles.

2. Tune RF frequency to maximize the electron beam current observed on the Faraday cup.

3. Turn off the solenoids and steering magnets of the cavity.

4. Tune the gun-side solenoid and maximize the electron beam current observed on the Faraday cup.

4. Tune gun-side steering magnets (both horizontal and vertical) and maximize the electron beam current observed on the Faraday cup. Center the beam on the OTR screen.

5. Tune the exit-side solenoid, maximize the electron beam current observed on the Faraday cup, and center the beam on the OTR screen.

6. Tune exit-side steering magnets (both horizontal and vertical) and maximize the electron beam current observed on the Faraday cup. Try to center the beam on the OTR screen.

7. Repeat steps 3-7 until the electron beam current observed on the Faraday cup is maximized, the beam size is minimized and round, as well as the beam is centered on the OTR screen.

8. Tune the quadrupoles (start from the upstream and go down with order) to optimize beam transmission (maximum current, minimum beam size, beam centered on OTR).

Appendix D

Apparatus

D.1 Quadrupole Magnet

The quadrapole magnets used in the HRRL beamline are type 2 quadrupoles manufactured by "Tesla Engineering Limited" [19]. Bore aperture radius of the quadrapole magnet is 2.54 cm and length of the pole face in z-direction is 8 cm. The magnetic field of the quadrupole magnet was mapped using a Hall probe placed next to the pole face. The probe was installed to a translator to move in the longitudinal direction (z-direction). The probe was placed 13 cm from the pole center and moved with 0.5 cm increment. The current of the quadrupole was increased with 0.2 A increment up to 3 A. The measured B-field strengths at different z-locations and currents are given in Table D.1 and Figure D.1. Quadrupole magnet maximum B-field and effective length at different currents are given in Table D.2

Table D.1: Quadrupole Magnet B-field Measured.

z-axis	B-field (Gauss)														
cm	I_{quad} 0.2 A	I_{quad} 0.4 A	I_{quad} 0.6 A	I_{quad} 0.8 A	I_{quad} 1.0 A	I_{quad} 1.2 A	I_{quad} 1.4 A	I_{quad} 1.6 A	I_{quad} 1.8 A	I_{quad} 2.0 A	I_{quad} 2.2 A	I_{quad} 2.4 A	I_{quad} 2.6 A	I_{quad} 2.8 A	I_{quad} 3.0 A
0.00	-0.28	-0.29	-0.25	-0.33	-0.36	-0.43	-0.36	-0.38	-0.42	-0.41	-0.40	-0.39	-0.37	-0.35	-0.35
2.50	-0.39	-0.58	-0.43	-0.28	-0.38	-0.32	-0.38	-0.35	-0.45	-0.47	-0.46	-0.49	-0.50	-0.47	-0.49
5.00	-0.60	-0.58	-0.55	-0.53	-0.46	-0.39	-0.37	-0.34	-0.30	-0.23	-0.20	-0.11	-0.09	-0.08	-0.03
6.00	-0.38	-0.27	-0.17	-0.06	0.16	0.26	0.39	0.53	0.65	0.74	0.85	1.07	1.17	1.32	1.43
6.50	0.04	0.26	0.41	0.60	0.88	1.18	1.42	1.66	1.90	2.09	2.46	2.70	2.86	3.00	3.27
7.00	0.63	0.94	1.30	1.67	2.03	2.58	2.95	3.30	3.68	3.98	3.54	4.95	5.35	5.68	6.06
7.50	1.44	1.99	2.56	3.11	3.69	4.53	5.10	5.70	6.28	6.80	7.42	8.29	8.90	9.50	10.10
8.00	2.50	3.30	4.11	4.95	6.30	7.15	8.03	8.87	9.75	10.60	11.97	12.85	13.72	14.63	15.50
8.50	3.76	4.89	6.10	7.28	9.07	10.27	11.47	12.70	13.95	15.17	17.07	18.33	19.57	20.82	22.09
9.00	4.60	7.03	8.61	10.22	11.80	13.45	15.90	17.60	19.28	20.94	22.80	24.46	26.14	28.73	30.40
9.50	6.43	8.30	10.20	12.20	14.11	17.11	19.15	21.19	23.22	25.22	28.30	30.37	32.42	34.45	36.52
10.00	7.10	8.97	11.05	14.20	16.38	18.58	20.78	23.13	25.53	28.90	31.15	33.44	35.70	37.96	41.30
10.50	7.50	9.70	11.95	14.24	16.75	19.26	21.74	24.60	26.95	29.50	33.00	35.40	37.77	40.20	42.60
11.00	7.67	9.92	12.20	15.26	17.56	19.95	22.35	24.86	28.57	30.90	33.35	35.80	38.45	41.04	43.67
11.50	7.70	10.02	12.30	14.67	18.25	20.61	23.00	25.44	27.92	30.40	33.95	36.46	38.92	41.38	43.95

Continued on next page

117

Table D.1 – *Continued from previous page*

z-axis	I_{quad}	I_{quad}	I_{quad}	I_{quad}	I_{quad}	I_{quad}	I_{quad}	I_{quad}	I_{quad}	I_{quad}	I_{quad}	I_{quad}	I_{quad}	I_{quad}	I_{quad}
cm	0.2 A	0.4 A	0.6 A	0.8 A	1.0 A	1.2 A	1.4 A	1.6 A	1.8 A	2.0 A	2.2 A	2.4 A	2.6 A	2.8 A	3.0 A
12.00	7.66	9.93	12.33	14.70	17.36	19.82	22.55	25.14	28.96	31.31	33.81	36.30	38.80	41.50	44.44
12.50	7.74	10.08	12.40	14.77	17.46	20.05	22.60	25.26	29.00	31.44	34.04	36.46	39.05	41.77	44.29
13.50	7.73	10.04	12.43	14.80	17.36	20.02	22.86	25.37	29.12	31.61	34.22	36.69	39.60	41.99	44.49
14.00	8.24	10.63	12.98	15.38	17.88	21.74	24.10	26.44	28.94	31.47	34.25	36.90	39.90	42.46	45.08
15.00	8.12	10.50	12.84	15.26	17.90	20.56	23.36	26.00	28.67	31.43	34.23	36.87	39.58	43.26	45.75
15.50	8.01	9.98	12.67	15.95	18.30	20.75	23.23	25.70	29.44	31.17	34.48	37.06	39.45	42.10	46.14
16.00	7.80	10.08	12.44	14.82	17.36	19.96	22.80	25.22	27.99	30.86	33.60	36.09	39.10	41.56	44.38
16.50	7.62	10.04	12.26	14.60	16.90	19.55	22.26	24.76	27.48	30.10	32.62	35.47	38.17	40.59	44.26
17.00	7.18	8.28	11.44	13.60	15.88	18.34	20.75	23.25	25.70	28.00	30.74	33.07	35.50	38.08	40.72
17.50	6.18	7.98	9.86	11.71	13.77	15.88	18.00	19.96	22.10	24.33	26.50	28.76	30.74	32.84	35.12
18.00	4.70	6.11	5.57	9.06	10.70	12.33	14.04	15.67	17.31	18.96	20.62	22.33	24.11	25.66	27.37
18.50	3.14	4.17	5.25	6.29	7.46	8.65	9.86	11.07	12.30	13.60	14.77	16.00	17.19	18.48	19.60
19.00	2.43	2.90	3.35	4.14	4.84	5.65	6.56	7.39	8.20	9.00	9.85	10.70	11.80	12.56	13.30
19.50	0.88	1.33	1.77	2.25	2.77	3.30	3.80	4.34	4.82	5.33	5.88	6.44	7.00	7.68	8.16
20.00	0.00	0.26	0.52	0.82	1.11	1.41	1.72	2.00	2.33	2.66	2.95	3.23	3.57	3.90	4.20
20.50	-0.56	-0.45	-0.29	-0.20	0.00	0.12	0.26	0.46	0.63	0.80	0.90	1.10	1.27	1.45	1.60

B-field (Gauss)

Table D.1 – *Continued from previous page*

z-axis	I_{quad}	I_{quad}	I_{quad}	I_{quad}	I_{quad}	I_{quad}	I_{quad}	B-field (Gauss) I_{quad}	I_{quad}	I_{quad}	I_{quad}	I_{quad}	I_{quad}	I_{quad}	I_{quad}
cm	0.2 A	0.4 A	0.6 A	0.8 A	1.0 A	1.2 A	1.4 A	1.6 A	1.8 A	2.0 A	2.2 A	2.4 A	2.6 A	2.8 A	3.0 A
21.00	-0.88	-0.77	-0.70	-0.62	-0.55	-0.46	-0.39	-0.29	-0.20	-0.13	-0.03	0.03	0.18	0.24	0.33
21.50	-0.89	-0.79	-0.76	-0.71	-0.66	-0.60	-0.53	-0.50	-0.43	-0.40	-0.39	-0.37	-0.26	-0.24	-0.21
22.00	-0.84	-0.81	-0.78	-0.75	-0.70	-0.65	-0.67	-0.62	-0.64	0.58	-0.56	-0.51	-0.52	-0.48	-0.44
22.50	-0.80	-0.75	-0.76	-0.72	-0.70	-0.68	-0.65	-0.62	-0.63	-0.60	-0.60	-0.58	-0.58	-0.55	-0.56
23.00	-0.77	-0.75	-0.73	-0.76	-0.73	-0.72	-0.71	-0.70	-0.68	-0.65	-0.64	-0.62	-0.63	-0.64	-0.62
24.00	-0.70	-0.70	-0.68	-0.72	-0.74	-0.77	-0.72	-0.73	-0.74	-0.75	-0.70	-0.70	-0.71	-0.71	-0.70
25.50	-0.71	-0.72	-0.73	-0.74	-0.73	-0.73	-0.73	-0.73	-0.74	-0.71	-0.74	-0.72	-0.70	-0.69	-0.74
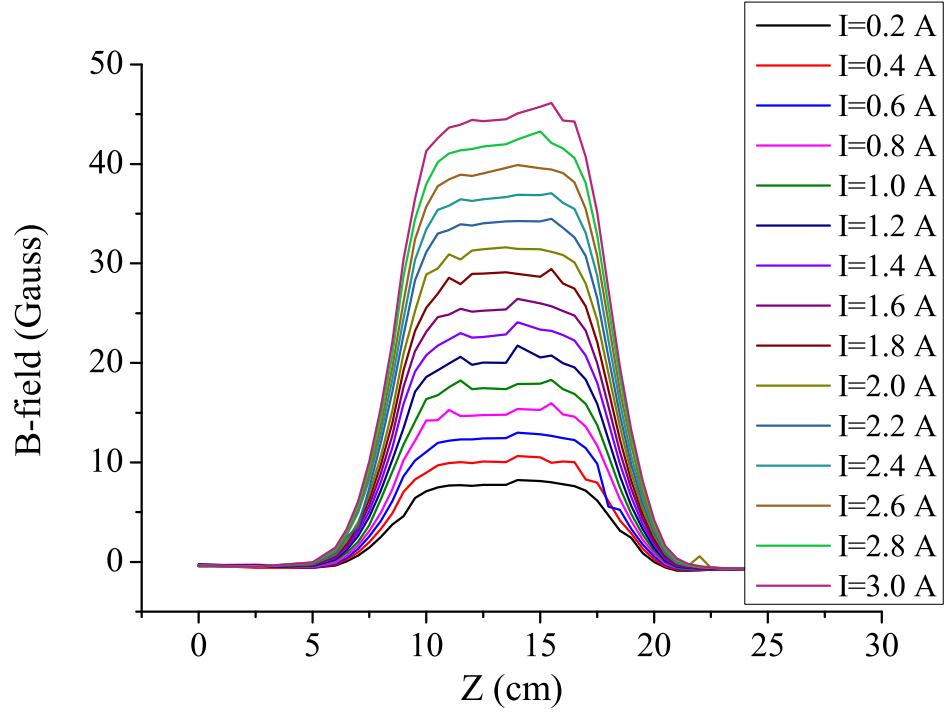
Figure D.1: Quadrupole Magnet B-field Measured.

D.2 Dipole Magnet

The dipole magnets were manufactured by "ISYS Ion Beam Systems Inc." [22] and were designed to bend a beam by 45° with 318.5 mm radius. The dipole chamber has 18 mm vertical aperture. The magnetic field of the dipole was measured for 4 current settings given in Table D.2 and shown in Figure D.2.

Table D.3: Dipole Magnet B-field Measured Along the Reference Beam Path.

S	B-field	B-field	B-field	B-field
(mm)	(Gauss)	(Gauss)	(Gauss)	(Gauss)
	$I = -6.50$ A	$I = -15.25$ A	$I = -24.00$ A	$I = -33.00$ A
0	-2.67	-6.00	-9.24	-11.43
5.00	-2.84	-7.02	-10.84	-13.42

Continued on next page

120

S (mm)	B-field (Gauss) -6.50 A	B-field (Gauss) -15.25 A	B-field (Gauss) -24.00 A	B-field (Gauss) -33.00 A
10.00	-3.07	-8.27	-12.77	-15.83
15.00	-3.12	-9.77	-15.12	-18.25
20.00	-3.67	-11.60	-17.98	-22.32
25.00	-4.33	-13.84	-21.49	-26.68
30.00	-5.12	-16.60	-25.81	-31.87
35.00	-6.10	-20.01	-30.97	-38.50
40.00	-7.30	-24.25	-37.58	-46.74
45.00	-8.77	-29.55	-45.83	-57.04
50.00	-10.61	-35.96	-56.18	-69.95
55.00	-15.76	-44.25	-69.18	-86.18
60.00	-23.88	-54.67	-85.54	-106.59
65.00	-29.55	-67.78	-106.12	-132.26
70.00	-36.45	-84.23	-131.39	-164.52
75.00	-45.32	-104.81	-164.27	-204.86
80.00	-56.34	-130.50	-204.61	-255.22
85.00	-70.09	-162.49	-254.87	-317.70
90.00	-87.25	-202.43	-317.34	-395.93
92.00	-95.26	-221.08	-346.60	-432.40
94.00	-104.05	-241.53	-378.67	-472.48
96.00	-113.69	-263.96	-413.85	-516.44
98.00	-124.26	-288.57	-452.39	-564.64
100.00	-135.87	-315.31	-494.75	-617.51
102.00	-148.53	-344.89	-541.15	-675.33
104.00	-162.44	-377.23	-591.94	-738.69
105.11	-170.82	-395.22	-615.64	-767.57

Table D.3 – *Continued from previous page*

S	B-field	B-field	B-field	B-field
(mm)	(Gauss)	(Gauss)	(Gauss)	(Gauss)
	-6.50 A	-15.25 A	-24.00 A	-33.00 A
107.90	-193.30	-447.35	-696.51	-868.32
110.68	-218.32	-505.17	-787.10	-980.56
113.46	-245.15	-576.45	-884.20	-1101.20
116.24	-271.55	-629.02	-979.92	-1220.80
119.02	-296.28	-686.30	-1069.30	-1331.60
121.81	-316.00	-733.05	-1142.40	-1422.50
124.59	-339.95	-766.68	-1195.00	-1487.80
127.37	-348.80	-788.63	-1229.20	-1530.30
130.15	-350.18	-798.95	-1249.70	-1558.40
132.94	-351.56	-809.26	-1261.30	-1570.30
138.50	-352.38	-815.77	-1271.50	-1582.90
144.07	-352.64	-817.76	-1274.70	-1586.90
149.63	-352.72	-818.35	-1275.70	-1588.20
155.20	-352.80	-818.59	-1276.20	-1588.74
166.33	-352.86	-818.79	-1276.70	-1589.30
177.46	-352.92	-819.04	-1277.00	-1589.80
188.58	-352.95	-819.25	-1277.50	-1590.37
199.71	-352.96	-819.45	-1277.90	-1590.73
210.84	-352.97	-819.59	-1278.20	-1591.05
221.97	-352.99	-819.72	-1278.40	-1591.40
233.10	-353.00	-819.86	-1278.70	-1591.80
244.23	-352.99	-820.00	-1279.00	-1592.07
255.36	-353.04	-820.16	-1279.20	-1592.30
266.49	-353.05	-820.30	-1279.44	-1592.40
277.62	-353.04	-820.40	-1279.56	-1592.70

Continued on next page

S (mm)	B-field (Gauss) -6.50 A	B-field (Gauss) -15.25 A	B-field (Gauss) -24.00 A	B-field (Gauss) -33.00 A
288.75	-353.02	-820.43	-1279.52	-1592.70
294.32	-352.97	-820.40	-1279.46	-1592.60
299.88	-352.83	-820.39	-1279.40	-1592.46
305.44	-352.68	-820.38	-1279.26	-1592.30
311.01	-351.80	-820.24	-1279.00	-1592.00
316.57	-350.65	-819.74	-1278.17	-1590.90
322.14	-348.40	-817.73	-1275.00	-1586.97
324.92	-344.00	-815.06	-1270.80	-1581.70
327.70	-336.00	-809.82	-1262.60	-1571.50
330.49	-322.34	-799.64	-1246.67	-1551.80
333.27	-301.64	-780.86	-1217.40	-1515.25
336.05	-275.00	-749.13	-1167.80	-1453.60
338.83	-245.83	-700.97	-1092.50	-1360.00
341.62	-215.58	-639.14	-996.14	-1239.46
344.40	-187.72	-570.24	-888.66	-1105.50
347.18	-162.57	-500.24	-779.86	-969.80
349.96	-140.66	-435.41	-679.20	-844.62
352.75	-133.46	-377.20	-588.10	-732.05
355.53	-120.30	-326.14	-508.20	-632.51
356.53	-108.55	-305.79	-481.38	-597.30
358.53	-98.02	-275.51	-433.77	-538.20
360.53	-84.15	-248.38	-391.15	-485.20
362.53	-72.44	-224.38	-353.00	-437.70
365.53	-62.42	-192.56	-302.89	-375.37
368.53	-59.42	-165.48	-260.44	-322.40

S (mm)	B-field (Gauss) -6.50 A	B-field (Gauss) -15.25 A	B-field (Gauss) -24.00 A	B-field (Gauss) -33.00 A
371.53	-46.53	-142.40	-224.09	-277.28
372.53	-36.59	-135.47	-213.18	-263.90
377.53	-28.92	-105.75	-166.37	-205.84
382.53	-23.13	-82.85	-130.30	-161.10
387.53	-18.53	-65.20	-102.48	-126.58
392.53	-14.95	-51.56	-81.01	-99.94
397.53	-9.96	-41.05	-64.45	-79.38
402.53	-6.86	-32.90	-51.60	-63.56
412.53	-3.07	-21.71	-33.78	-41.35
422.53	-1.62	-14.63	-22.83	-27.64
447.53	-6.12	-6.12	-9.45	-11.30
472.53	-2.94	-2.94	-4.46	-5.19

The effective magnetic field of a dipole magnet is calculated by dividing the area under the magnetic field curve, shown in Figure D.2 and column 2 in Table D.4, by the length of a reference particle path inside the dipole. The bending radius of the dipole is 318.5 mm and the bending angle is 45°. The length of particle path inside the dipole is

$$s = \rho \times \theta = 318.5 \times \pi/4 = 250.15 \text{ mm}. \tag{D.1}$$

The required magnetic bending strength for a particle with momentum p and charge q for a given bending radius ρ is described by magnet (or momentum) rigidity [8]

$$p = qB\rho \tag{D.2}$$

Table D.2: Quadrupole Magnet Maximum B-field and Effective Length at Different Currents.

I Amp	Area Under the Curve Gauss·cm	B_{max} Gauss	L_{eff} cm
3.0	445.35	44.78 ± 0.76	9.95 ± 0.17
2.8	420.64	42.44 ± 0.70	9.91 ± 0.16
2.6	396.30	40.01 ± 0.54	9.91 ± 0.13
2.4	370.81	37.64 ± 0.53	9.85 ± 0.14
2.2	345.33	35.06 ± 0.58	9.85 ± 0.16
2.0	314.01	31.80 ± 0.61	9.87 ± 0.19
1.8	288.32	29.36 ± 0.58	9.82 ± 0.19
1.6	263.57	26.73 ± 0.47	9.86 ± 0.17
1.4	237.03	24.35 ± 0.46	9.73 ± 0.18
1.2	209.26	21.69 ± 0.49	9.65 ± 0.22
1.0	177.86	18.32 ± 0.42	9.71 ± 0.22
0.8	150.72	15.74 ± 0.37	9.58 ± 0.23
0.6	124.96	13.22 ± 0.35	9.45 ± 0.25
0.4	98.49	10.75 ± 0.32	9.16 ± 0.27
0.2	71.96	8.18 ± 0.24	8.80 ± 0.26
0.0	37.90	4.59 ± 0.21	8.26 ± 0.38
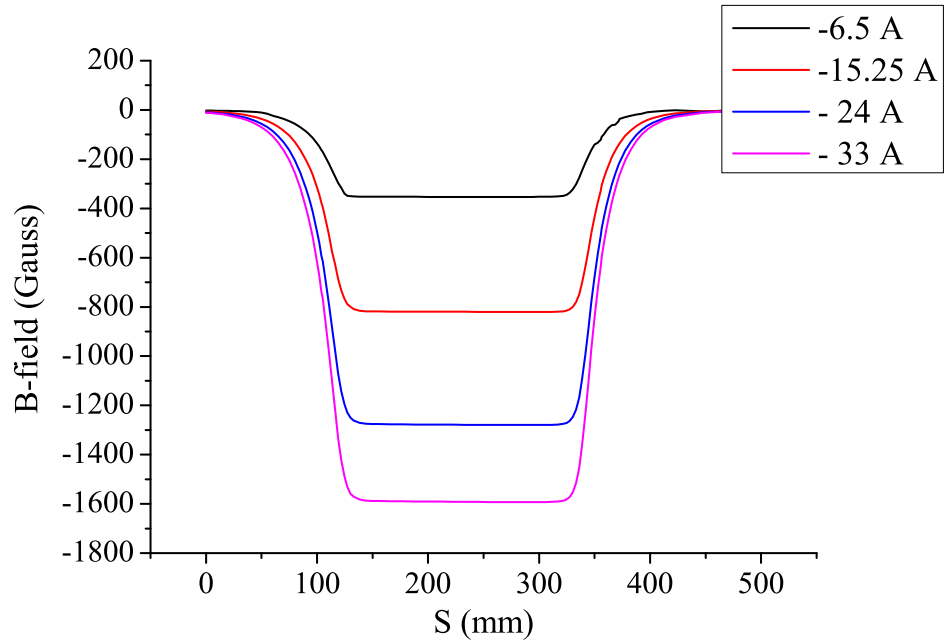
Figure D.2: Dipole magnet B-field measured along the reference beam path.

Table D.4: Quadrupole Magnet B-field Measured vs Dipole Current.

Dipole Current (A)	Area Under the Curve (Gauss·mm)	Beam Path in Dipole (mm)	Effective B-field (Gauss)
-6.50	-90700.33	250.15	-362.58
-15.25	-210413.96	250.15	-841.15
-24.00	-328194.85	250.15	-1312.00
-33.00	-408481.83	250.15	-1632.95

For an electron

$$p[\text{kg} \cdot \text{m/s}] = eB\rho \tag{D.3}$$

or

$$p[\text{GeV/c}] = 0.2998B\rho \tag{D.4}$$

The relation of dipole current to the electron beam energy (to complete a 45°
bend) is given in Figure D.3 and the fit is

$$En(\text{MeV}) = (-0.68 \pm 0.65) + (0.67 \pm 0.08)I(\text{A}) + (-0.005 \pm 0.002)I^2(\text{A}) \tag{D.5}$$
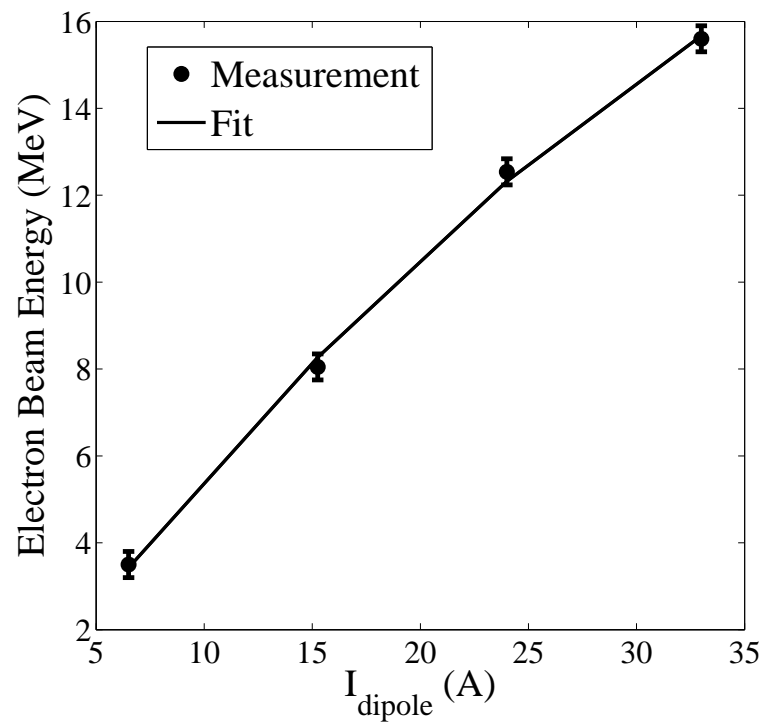
Figure D.3: The relation of dipole current to the electron beam energy for completing a 45° bend.

Appendix E

ROOT Script for Positron and Electron Rate Estimation

This is the ROOT script used to calculate number/charge of e^-/e^+ and the ratio of the two. It loads ROOT files created from positron production runs, plots the spectrum, and prints results to a file.

```
#include <stdio.h>
#include <exception>
#include <stdlib.h>
#include <string.h>
char filename1[255],filename2[255],filename3[255];
char output2hist[255],output2hist2[255];
Int_t Reprate=0,ri=0,ro=0,run_in=0,run_out=0,pulses=0;
Int_t run_time_out=0,run_time_in=0;
Int_t event_num_in=0,event_num_out=0;
Int_t int1=0,event1=0,bin_content[4001],NaI_mode=0,i=0;
Double_t a=0,b=0,c=0;
Double_t QT=,QT_er=0,Ne=0,Ne_er=0;
Long64_t ne1=0,ne2=0;    //total e- number
Double_t P_rate=0,P_rate_er=0;
Double_t ADC9_fit_mean=0,ADC9_fit_mean_er=0,Qs=0;
Double_t pos_ele_ratio=0,pos_ele_ratio_er=0;
Double_t ne=0,E_rate=0,E_rate_er=0,E_pp=0,Ie=0,Ie_er=0,e_rate=0;
Double_t Qt=0,Qt_er=0,Qt1=0,Qt2=0,Qpp1=0,Qpp2=0;
```

```cpp
Double_t Qps1=0,Qps2=0,Qt1_er=0,Qt2_er=0,ne=0,sum_sqrt=0;
Double_t Q_e = 1.60217646*1e-19; //electron charge
Double_t Q_Calb = (0.93*1e-9)/50,Q_Calb_er = (0.14*1e-9)/50;
Double_t FC1_Area = 1.2011e-6/50,sum_sqrt_er=0;//Vs/ohm *1s =C
ofstream myfile;
struct foo_return_type
{
Double_t a=0;
Double_t b=0;
Double_t c=0;
};


//hist_mod=1 is whole histogram
//hist_mod=2 is cut the histogram around 511 region.
main(Int_t Reprate, Int_t hist_mod, Int_t subtract) {
myfile.open ("3MeV.txt");
Reprate=300;
printf("reprate: %d\n",Reprate,hist_mod);
if(hist_mod==1){printf("draw around 511 keV.");}
if(hist_mod==2){printf("draw whole histogram.");}
if(subtract==1){printf("draw subtracted histogram.");}
if(subtract!=1){printf("draw overlayed histogram.");}
for(ri=1; ri<=2; ri++){
foo_return_type results;
results = NE(0,ri, Reprate);
cout << results.a << endl;
cout << results.b << endl;
cout << results.c << endl;
QT=results.a;
QT_er=results.b;
```

```
Ne=results.c;
printf("\n\n\n");
printf("\n\n\nQT=%g, QT_er=%g, Ne=%g\n",QT,QT_er,Ne);
printf("\nNe=T/Q_e=%g,  QT=Ne*Q_e=%g\n",QT/Q_e,Ne*Q_e);
printf("\nQ_e=QT/Ne=%g \n\n\n",QT/Ne);
printf("\n\n\n");
for(ro=1; ro<=1; ro++){
for(NaI_mode =1; NaI_mode <=2;  NaI_mode++){
//printf("%d %d %d %d\n",ri, ro, NaI_mode);
if(ri==1){run_in=3735;}
if(ri==2){run_in=3737;}
if(ro==1){run_out=3736;
}


draw(run_in, run_out, NaI_mode, Reprate, Ne, hist_mod, subtract);
}}}
if(hist_mod==1){
printf("draw around 511 keV.");
}
if(hist_mod==2){
printf("draw whole histogram.");
}
if(subtract==1){
printf("draw subtracted histogram.");
}
if(subtract!=1){
printf("draw overlayed histogram.");
}
myfile.close();
}
```

```
foo_return_type NE(Int_t re, Int_t ri, Int_t Reprate){

printf("%d %d \n",ri, Reprate);

if(ri==1) {

TFile *f=new TFile("/rootfiles/7-27-12/r3735.root");

run_time=1002;

Reprate=300;

events=9045;

pulses=301462;

}

if(ri==2) {

TFile *f=new TFile("/rootfiles/7-27-12/r3737.root");

run_time=1094;

Reprate=300;

events=15361;

pulses=329368;}

TTree *ntuple = (TTree*)f->Get("ntuple");

TH1F *f9=new TH1F("f9","ADC9",4000,0,4000);

TCanvas * c2 = new TCanvas("c2", "c2",600 ,500);

c2->cd();

ntuple->Draw("ADC9>>f9");

printf("%bin# Bin Content%d\n");

//_____Method 1_____//

for(i=1; i<=4000; i++){

foo_return_type fret;

bin_content[i] = f9->GetBinContent(i);

int1+=i*bin_content[i];

Qt1+=i*bin_content[i]*Q_Calb*(pulses/events);//Charge in a run.

event1+=bin_content[i];

sum_sqrt+=i*i*bin_content[i];
```

```
sum_sqrt_er=sqrt(sum_sqrt);

Qt1_er=sqrt(sum_sqrt_er*sum_sqrt_er*Q_Calb*Q_Calb+

sum_sqrt*sum_sqrt*Q_Calb*Q_Calb)*(pulses/events);

//printf("%d  %d  %g \n",i,bin_content[i],Qt1);}

printf("Method1: integrate all the channels of scintilator.\n");

printf("1.total charge: %g\n",Qt1);

//printf("%d  %d  %g \n",i,bin_content[i],Qp2);

//printf("total e- charge in this run with method 2: %g\n",Qp2);

//printf("Reprate: %d\n",Reprate);

ne1=Qt1/Q_e; //Ne: number of electrons in this run.

printf("1.total number of e-: %g\n\n",ne1);

//_____Method 2_____//

Double_t ADC9_mean, ADC9_rms;

ADC9_mean = f9->GetMean(1);

ADC9_rms  = f9->GetRMS(1);

printf("ADC9_mean=%g, ADC9_mean_er=%g \n\n",ADC9_mean,ADC9_rms);

//Qp: charge per pulse.

//Calibration: 1.22 (9nV s)/(ADC channel), 50 ohm terminal.

Qpp2 = ADC9_mean*Q_Calb;

printf("Method2: calculate with (ADC9_mean*Q_Calb)*pulses.\n");

printf("2. charge per pulse : %g nC\n",Qpp2);

Qps2 = Qpp2*Reprate; //charge per second

printf("2.charge per second : %g nC\n",Qps2);

printf("2.number of pulses : %g \n\n\n",pulses);

//printf("2.number of pulses : %g \n\n\n",Reprate*run_time);

Qt2=Qpp2*pulses;

Qt2_er=ADC9_rms*Q_Calb*pulses;

printf("2.total charge of e-: %g C\n",Qt2);

//_____Average of 2 method_____//

Qt = (Qt1+Qt2)/2;
```

```
Qt_er = sqrt(Qt1_er*Qt1_er + Qt2_er*Qt2_er)/2;

ne = Qt/Q_e;

printf("Comparing two method of calculating electron charge:\n");

printf("Method1: Total charge in this run, Qt1 = %g\n",Qt1);

printf("Method2: Total charge in this run, Qt2 = %g\n",Qt2);

printf("Qt1/Qt2 = %g\n\n",Qt1/Qt2);

printf("Qt=%g, Qt_er=%g, ne=%g\n",Qt,Qt_er,ne);

c2->Close();

f->Close();

fret.a=Qt;

fret.b=Qt_er;

fret.c=ne;

return fret;

}


draw(run_in,run_out,NaI_mode,Reprate,Ne,hist_mod,subtract){

printf("%d %d %d %d %d \n",run_in, run_out, NaI_mode, Reprate);

//_____T2 IN - Out_____//

if(run_in ==3735) {

run_time_in  = 1002;

event_num_in  = 9045;

}

if(run_in ==3737) {

run_time_in  = 1094;

event_num_in  = 15361;

}

if(run_out==3736) {

run_time_out = 892;

event_num_out = 3735;

}
```

```
if(hist_mod==1){

if(run_in ==3735) {

TString run_time_in_char

("(ADC6>1150 && ADC6<1550 && ADC5>1150 && ADC5<1550)/1002");

}

if(run_in ==3737) {

TString run_time_in_char

("(ADC6>1150 && ADC6<1550 && ADC5>1150 && ADC5<1550)/1094");

}

if(run_out==3736) {

TString run_time_out_char

("(ADC6>1150 && ADC6<1550 && ADC5>1150 && ADC5<1550)/892");

}

}else if{

if(run_in ==3735) {

TString run_time_in_char("1/1002");

}

if(run_in ==3737) {

TString run_time_in_char("1/1094");

}

if(run_out==3736) {

TString run_time_out_char("1/892");

}}

if(run_in==3735)  {

TFile *f = new TFile("/rootfiles/7-27-12/r3735.root");

TTree *ntuple = (TTree*)f->Get("ntuple");

}

if(run_in==3737)  {

TFile *f = new TFile("/rootfiles/7-27-12/r3737.root");

TTree *ntuple = (TTree*)f->Get("ntuple");
```

```
}
if(run_out==3736) {
TFile *f2 = new TFile("/rootfiles/7-27-12/r3736.root");
TTree *ntuple_out = (TTree*)f2->Get("ntuple");
}
if(NaI_mode==1) {
TH1F *T2_in_NaI_L=new TH1F("T2_in_NaI_L","",120,100,1300);
}
if(NaI_mode==2) {
TH1F *T2_in_NaI_R=new TH1F("T2_in_NaI_R","",120,100,1300);
}
if(NaI_mode==1) {
TH1F *T2_out_NaI_L=new TH1F("T2_out_NaI_L","T2_out_L",120,100,
1300);}
if(NaI_mode==2) {
TH1F *T2_out_NaI_R=new TH1F("T2_out_NaI_R","T2_out_R",120,100,
1300);}
TCanvas * Canvas_1=new TCanvas("Canvas_1","Canvas_1",700,500);
Canvas_1->SetMargin(0.2,0.01,0.17,0.03);
if( NaI_mode==1) {
T2_in_NaI_L->SetLineColor(kBlack);
T2_in_NaI_L->SetLineWidth(3);
T2_in_NaI_L->SetLineStyle(2);
T2_in_NaI_L->GetXaxis()->SetTitle("Energy (keV)");
T2_in_NaI_L->GetYaxis()->SetTitle("Rate (Hz)");
T2_in_NaI_L->GetXaxis()->SetTitleSize(0.09);
T2_in_NaI_L->GetYaxis()->SetTitleSize(0.09);
T2_in_NaI_L->GetXaxis()->SetLabelSize(0.08);
T2_in_NaI_L->GetYaxis()->SetLabelSize(0.08);
T2_in_NaI_L->GetXaxis()->SetTitleOffset(0.85);
```

```
T2_in_NaI_L->GetYaxis()->SetTitleOffset(1.1);

T2_in_NaI_L->GetXaxis()->SetLabelFont(132);

T2_in_NaI_L->GetXaxis()->SetTitleFont(132);

T2_in_NaI_L->GetYaxis()->SetLabelFont(132);

2_in_NaI_L->GetYaxis()->SetTitleFont(132);

}

if( NaI_mode==2) {

T2_in_NaI_R->SetLineColor(kBlack);

T2_in_NaI_R->SetLineWidth(3);

T2_in_NaI_R->SetLineStyle(2);

T2_in_NaI_R->GetXaxis()->SetTitle("Energy (keV)");

T2_in_NaI_R->GetYaxis()->SetTitle("Rate (Hz)");

T2_in_NaI_R->GetXaxis()->SetTitleSize(0.09);

T2_in_NaI_R->GetYaxis()->SetTitleSize(0.09);

T2_in_NaI_R->GetXaxis()->SetLabelSize(0.08);

T2_in_NaI_R->GetYaxis()->SetLabelSize(0.08);

T2_in_NaI_R->GetXaxis()->SetTitleOffset(0.85);

T2_in_NaI_R->GetYaxis()->SetTitleOffset(1.1);

T2_in_NaI_R->GetXaxis()->SetLabelFont(132);

T2_in_NaI_R->GetXaxis()->SetTitleFont(132);

T2_in_NaI_R->GetYaxis()->SetLabelFont(132);

T2_in_NaI_R->GetYaxis()->SetTitleFont(132);

}

gStyle->SetTitleFontSize(0.07);

gStyle->SetLabelSize(0.06,"X");

gStyle->SetLabelSize(0.06,"Y");

gStyle->SetTitleSize(0.065,"X");

gStyle->SetTitleSize(0.065,"Y");

gStyle->SetTitleOffset(1,"X");

gStyle->SetTitleOffset(1.2,"Y");
```

```
gStyle->SetOptStat(0);

gStyle->SetTextFont(132);

//if(hist_mod==1){gStyle->SetOptStat("neMR");}

//if(hist_mod==2){gStyle->SetOptStat("neMRi");}

if(NaI_mode==1) {

T2_out_NaI_L->SetLineColor(kBlack);

T2_out_NaI_L->SetLineWidth(2);

}

if(NaI_mode==2) {

T2_out_NaI_R->SetLineColor(kBlack);

T2_out_NaI_R->SetLineWidth(2);

}

//if(subtract==1)

//_____T2 IN _____

if(NaI_mode==1){

ntuple->Draw("ADC6/2.66>>T2_in_NaI_L",run_time_in_char,"AC*");

}

if(NaI_mode==2){

ntuple->Draw("ADC5/2.61>>T2_in_NaI_R",run_time_in_char,"AC*");

}

//_____T2 OUT_____

if(NaI_mode==1)  {

ntuple_out->Draw("ADC6/2.66>>T2_out_NaI_L",run_time_out_char);

}

if(NaI_mode==2)  {

ntuple_out->Draw("ADC5/2.61>>T2_out_NaI_R",run_time_out_char);

}

//_____subtract_____

if(NaI_mode==1){

T2_in_NaI_L->Add(T2_out_NaI_L,-1); T2_in_NaI_L->Draw();
```

```
}
if(NaI_mode==2){
T2_in_NaI_R->Add(T2_out_NaI_R,-1); T2_in_NaI_R->Draw();
}
gPad->Update();
if(NaI_mode==1) {
TPaveStats *st = (
TPaveStats*)T2_in_NaI_L->FindObject("stats");
P_rate = T2_in_NaI_L->Integral();
}
if(NaI_mode==2) {
TPaveStats *st = (
TPaveStats*)T2_in_NaI_R->FindObject("stats");
P_rate = T2_in_NaI_R->Integral();
}
//if(subtract==2)
{
//_____T2 IN _____
if(NaI_mode==1){
ntuple->Draw("ADC6/2.66>>T2_in_NaI_L",run_time_in_char,"AC*");
}
if(NaI_mode==2){
ntuple->Draw("ADC5/2.61>>T2_in_NaI_R",run_time_in_char,"AC*");
}
//_____T2 OUT_____
if(NaI_mode==1)  {
ntuple_out->Draw("ADC6/2.66>>T2_out_NaI_L",run_time_out_char);
}
if(NaI_mode==2)  {
ntuple_out->Draw("ADC5/2.61>>T2_out_NaI_R",run_time_out_char);
```

```
}
//_____overlap_____
if(NaI_mode==1){
T2_in_NaI_L->Draw("");T2_out_NaI_L->Draw("same");
}
if(NaI_mode==2){
T2_in_NaI_R->Draw("");T2_out_NaI_R->Draw("same");
}}
//E_pp=Ne/Pulses;                    //electron number per pulse
E_rate=Ne/run_time_in;           //electron number per second
//Ie=E_rate*Q_e;
Ie=QT/run_time_in;
Ie_er=QT_er/run_time_in;
Ne_er=QT_er/Q_e;
pos_ele_ratio=P_rate/E_rate; //positron and electron ratio
P_rate_er=sqrt(P_rate/run_time_in);
E_rate_er=Ne_er/run_time_in;
pos_ele_ratio_er=sqrt(P_rate_er*P_rate_er+(P_rate_er*P_rate_er
*E_rate_er*E_rate_er)/(E_rate*E_rate))/E_rate;
printf("electrons per second:%g+-%g\n",E_rate,E_rate_er);
printf("electron current:%g+-%g, \n",Ie,Ie_er);
printf("positrons per second:%g +- %g\n",P_rate,P_rate_er);
printf("e+ to e- ratio:%g +- %g\n",pos_ele_ratio,
pos_ele_ratio_er);
sprintf(output2hist, "%.2g Hz e^{+} / %.2f \\muA e^{-}", P_rate,
Ie*1e6);
sprintf(output2hist2, "%.5g Hz e^{+} / %.5f \\muA e^{-}", P_rate,
Ie*1e6);
printf("\n %s \n",output2hist);
if(subtract!=1){
```

```
//NDC sets coords relative to pad
TPaveText *myText = new TPaveText(0.53,0.7,0.64,0.77, "NDC");
myTextEntry = myText->AddText("T2 in");
myText->SetTextSize(0.07);
myText->SetTextColor(kBlack);
myText->SetFillColor(0);          //white background
myText->SetTextAlign(12);
myText->SetTextFont(132);
myText->Draw();
TPaveText *myText_out = new TPaveText(0.53,0.4,0.66,0.47, "NDC");
myText_outEntry = myText_out->AddText("T2 out");
myText_out->SetTextSize(0.07);
myText_out->SetTextColor(kBlack);
myText_out->SetFillColor(0);
myText_out->SetTextAlign(12);
myText_out->SetTextFont(132);
myText_out->Draw();
}
if(subtract==1){
if(NaI_mode==1){
T2_in_NaI_L->Add(T2_out_NaI_L,-1); T2_in_NaI_L->Draw();
}
if(NaI_mode==2){
T2_in_NaI_R->Add(T2_out_NaI_R,-1); T2_in_NaI_R->Draw();
}}
if(hist_mod==1){
if(NaI_mode==1){
T2_in_NaI_L->SetAxisRange(0, 0.045, "Y");
}
if(NaI_mode==2){
```

```
T2_in_NaI_R->SetAxisRange(0, 0.045, "Y");
}
}else if{
if(NaI_mode==1){
T2_in_NaI_L->SetAxisRange(0, 0.10, "Y");
}
if(NaI_mode==2){
T2_in_NaI_R->SetAxisRange(0, 0.45, "Y");
}}


TPaveText *myText_rate=new TPaveText(0.51,0.8,0.95,0.885, "NDC");
myText_rateEntry=myText_rate->AddText(output2hist);
myText_rate->SetTextSize(0.07);
myText_rate->SetTextColor(kBlack);
myText_rate->SetFillColor(0);          //white background
myText_rate->SetTextAlign(12);
myText_rate->SetTextFont(132);
myText_rate->Draw();


//_____save data _____
sprintf(filename1, "\"r%d_sub_r%d.txt\"", run_in, run_out);
sprintf(filename2, "\"r%d_sub_r%d.png\"", run_in, run_out);
sprintf(filename3, "\"r%d_sub_r%d.eps\"", run_in, run_out);
printf("\nfilename1:%s\n",filename1);
printf("\nfilename2:%s\n",filename2);
printf("\nfilename3:%s\n",filename3);
if(NaI_mode==1) {
myfile <<"Reprate = "<<Reprate<<" Hz\n\n";
myfile <<"Run time = "<<run_time_in<<" s\n\n";
myfile <<"Pulses = "<<pulses<<"\n\n";
```

```
myfile <<"Events = "<<events<<"\n\n";

myfile <<"Electron numbers="<<Ne<<"+-"<<Ne_er<<"\n\n";

myfile <<"Electron charge="<<QT<<"+-"<<QT_er<<"C\n\n";

myfile <<"e- rate=" << E_rate <<"+-"<< E_rate_er <<" (Hz)\n\n";

myfile <<"e+ rate=" << P_rate <<"+-"<< P_rate_er <<" (Hz)\n\n";

myfile <<"e+/e-="<<pos_ele_ratio<<"+-"<<pos_ele_ratio_er<<"\n\n";

myfile <<"e- current:I_e-=" << Ie <<"+-"<< Ie_er <<" (A)\n\n";

myfile <<"e+/I_e-=" << output2hist2  <<"\n" ;
}
//_____save figures_____
if(NaI_mode==2) {

if(run_in==3735 && run_out==3736) {

Canvas_1->SaveAs("NaI_R/r3735_sub_r3736.root");

Canvas_1->SaveAs("NaI_R/r3735_sub_r3736.png");

Canvas_1->SaveAs("NaI_R/r3735_sub_r3736.eps");

rename("pos_ele_ration.txt", "NaI_R/r3735_sub_r3736.txt");}

if(run_in==3735 && run_out==3736) {

Canvas_1->SaveAs("NaI_R/r3735_sub_r3736.root");

Canvas_1->SaveAs("NaI_R/r3735_sub_r3736.png");

Canvas_1->SaveAs("NaI_R/r3735_sub_r3736.eps");

rename("pos_ele_ration.txt", "NaI_R/r3735_sub_r3736.txt");}
}
if(NaI_mode==1) {

if(run_in==3735 && run_out==3736) {

Canvas_1->SaveAs("NaI_L/r3735_sub_r3736.root");

Canvas_1->SaveAs("NaI_L/r3735_sub_r3736.png");

Canvas_1->SaveAs("NaI_L/r3735_sub_r3736.eps");

rename("pos_ele_ration.txt", "NaI_L/r3735_sub_r3736.txt");}

if(run_in==3735 && run_out==3736) {

Canvas_1->SaveAs("NaI_L/r3735_sub_r3736.root");
```

```
Canvas_1->SaveAs("NaI_L/r3735_sub_r3736.png");

Canvas_1->SaveAs("NaI_L/r3735_sub_r3736.eps");

rename("pos_ele_ration.txt", "NaI_L/r3735_sub_r3736.txt");}

}

if(NaI_mode==2) {

if(run_in==3737 && run_out==3736) {

Canvas_1->SaveAs("NaI_R/r3737_sub_r3736.root");

Canvas_1->SaveAs("NaI_R/r3737_sub_r3736.png");

Canvas_1->SaveAs("NaI_R/r3737_sub_r3736.eps");

rename("pos_ele_ration.txt", "NaI_R/r3737_sub_r3736.txt");}

if(run_in==3737 && run_out==3736) {

Canvas_1->SaveAs("NaI_R/r3737_sub_r3736.root");

Canvas_1->SaveAs("NaI_R/r3737_sub_r3736.png");

Canvas_1->SaveAs("NaI_R/r3737_sub_r3736.eps");

rename("pos_ele_ration.txt", "NaI_R/r3737_sub_r3736.txt");}

}

if(NaI_mode==1) {

if(run_in==3737 && run_out==3736) {

Canvas_1->SaveAs("NaI_L/r3737_sub_r3736.root");

Canvas_1->SaveAs("NaI_L/r3737_sub_r3736.png");

Canvas_1->SaveAs("NaI_L/r3737_sub_r3736.eps");

rename("pos_ele_ration.txt", "NaI_L/r3737_sub_r3736.txt");}

if(run_in==3737 && run_out==3736) {

Canvas_1->SaveAs("NaI_L/r3737_sub_r3736.root");

Canvas_1->SaveAs("NaI_L/r3737_sub_r3736.png");

Canvas_1->SaveAs("NaI_L/r3737_sub_r3736.eps");

rename("pos_ele_ration.txt", "NaI_L/r3737_sub_r3736.txt");}

}

// Delete histograms

if( subtract==1 || subtract!=1 ){
```

```
if(NaI_mode==1){T2_in_NaI_L->Delete();}
if(NaI_mode==2){T2_in_NaI_R->Delete();}
}
Canvas_1->Close();
f->Close();
f2->Close();
}
```

Appendix F

G4beamline Script for Positron Generation Using HRRL Beamline

To have better understanding of The ratios of positrons, detected using NaI detectors in coincidence mode, to the electrons impinging on T1 and to study the processes of position generation and transportation, simulations were performed using G4beamline. The G4beamline script for positron generation using HRRL beamline is given below.

```
#HRRL.g4bl
#G4beamline script for HRRL beamline.
#All units are in mm, Tesla, MeV, ns
#Written by Sadiq Setiniyaz.
#The "default" physics list is QGSP_BERT.
#QGSP_BERT is better for low-energy simulations.
#for e- process : ElectroNuclear
#models : CHIPSElectroNuclear from 0 GeV to 30000 GeV
#cross sections : ElectroNuclearXS from 0 GeV to 100000 GeV
#physics QGSP_BERT
physics QGSP_BERT_EMX
randomseed Time
param -unset param1=1
#use $first for the Root file (.root will be appended)
#param histoFile=$param1
#output $histoFile.out
```

```
#parameters

param En_ele=11.0 M=0.510998910

param P=sqrt($En_ele*$En_ele-$M*$M)

param emitX=0.37*15*10^(-6) emitY=0.30*15*10^(-6)

param betaX=1.4 betaY=1.17 alphaX=0.97 alphaY=0.24

param gammaX=(1+$alphaX^2)/$betaX gammaY=(1+$alphaY^2)/$betaY

param -unset T1T=1.016 T1R=15.875

param beam_z=-260 DG_z=-259.9

param Q1_z=75 Q2_z=315 Q3_z=553 Q4_z=1503 Q5_z=1753

param Q6_z=1990 DD1_z=2419.9 D1_z=2542

param Q7_z=$D1_z+443.356 D2_z=$D1_z+927.0 Deg90_z=3469.84375

param T1_z=943.5

param FDT1_z=$T1_z-26.52 DT1_z=$T1_z+1 DBT1_z=$T1_z+26.52 DQ4_z=1427.9

param Q7_x=443.356 D2_x=927.0 Q8_x=1562  Q9_x=2101 Q10_x=2642

param NaI_x=6369.5 NaIR_z=$Deg90_z+170+38.1 NaIL_z=$Deg90_z-170-38.1

#magnet currents and gradiants

param -unset I_Q1=3 I_Q2=3 I_Q3=0 I_Q4=2 I_Q5=0 I_Q6=0

param -unset I_Q2=0 I_Q7=10 I_Q8=2 I_Q9=2 I_Q10=2

param -unset g_Q1=(3.6*10^(-4)+1945*10^(-6)*$I_Q1)/0.0254

param -unset g_Q2=(3.6*10^(-4)+1945*10^(-6)*$I_Q2)/0.0254

param -unset g_Q3=(3.6*10^(-4)+1945*10^(-6)*$I_Q3)/0.0254

param -unset g_Q4=(3.6*10^(-4)+1945*10^(-6)*$I_Q4)/0.0254

param -unset g_Q5=(3.6*10^(-4)+1945*10^(-6)*$I_Q5)/0.0254

param -unset g_Q6=(3.6*10^(-4)+1945*10^(-6)*$I_Q6)/0.0254

param -unset g_Q7=(3.6*10^(-4)+1945*10^(-6)*$I_Q7)/0.0254

param -unset g_Q8=(3.6*10^(-4)+1945*10^(-6)*$I_Q8)/0.0254

param -unset g_Q9=(3.6*10^(-4)+1945*10^(-6)*$I_Q9)/0.0254

param -unset g_Q10=(3.6*10^(-4)+1945*10^(-6)*$I_Q10)/0.0254

param -unset g_D1_By=0.001

param -unset Jaw_W=3.57*25.4 Jaw_H=1.978*25.4
```

```
param -unset Jaw_L=0.995*25.4 JawGap1=3.5*25.4 JawGap2=-3.5*25.4
param -unset L_zpect_to_Jaw1X=(9.0-5.88)*25.4
param -unset Q7OFF=(sqrt(2)/2)*0.4889294
#beampipe
param -unset BeamPipeColor=0.6,0.6,0.6,0.3
tubs BeamPipe innerRadius=24 outerRadius=25.4 length=2420-$beam_z \
material=Al kill=1 color=$BeamPipeColor
place BeamPipe z=(2420-$beam_z)/2+$beam_z x=0
tubs BeamPipe45 innerRadius=24 outerRadius=25.4 \
length=sqrt(($D2_z-$D1_z)^2+$D2_x^2)-260 material=Al kill=1 \
color=$BeamPipeColor
place BeamPipe45 z=$Q7_z+$Q7OFF+30  x=$Q7_x-$Q7OFF+30 rotation=Y45
tubs BeamPipe90 innerRadius=24 outerRadius=25.4 \
length=($NaI_x-$D2_x)-200 material=Al kill=1 color=$BeamPipeColor
place BeamPipe90 z=$Deg90_z  x=$D2_x+($NaI_x-$D2_x)/2 rotation=Y90


#Jaw is 34.8 mm wide in the experiment.
box Jaw width=100 height=100 length=10 material=W kill=1 \
color=0.1,0.9,0.5
place Jaw x=$Q7_x-75-200+(50+34.8/2)/sqrt(2) y=0 \
z=$Q7_z-75-200-(50+34.8/2)/sqrt(2) rotation=Y45
place Jaw x=$Q7_x-75-200-(50+34.8/2)/sqrt(2) y=0 \
z=$Q7_z-75-200+(50+34.8/2)/sqrt(2) rotation=Y45
#tungsten targets, T1 and T2.
cylinder T1 outerRadius=$T1R length=$T1T material=W color=1,0,0
cylinder T2 outerRadius=$T1R length=$T1T material=W color=1,0,0
#place quadrupoles.
genericquad QuadTypeQC fieldLength=97  poleTipRadius=25.4 \
coilRadius=36 coilHalfwidth=47 ironRadius=81 ironLength=80 \
ironColor=0,1,0 kill=1
```

```
genericquad QuadTypeII fieldLength=150 poleTipRadius=25.4 \
coilRadius=36 coilHalfwidth=47 ironRadius=81 ironLength=150 \
ironColor=0,1,0 kill=1
genericquad Quad fieldLength=97 ironLength=80 apertureRadius=25.4 \
ironRadius=81 kill=1
#virtual detectors.
virtualdetector  DT    radius=25.4  length=0.001 color=0,1,1 \
format=root
virtualdetector  DG    radius=31.75 length=0.001 color=0,1,1 \
format=root
virtualdetector  FDT1  radius=31.75 length=0.001 color=0,1,1 \
format=root
virtualdetector  DT1   radius=31.75 length=0.001 color=0,1,1 \
format=root
virtualdetector  DUPT1 radius=31.75 length=0.001 color=0,1,1 \
format=root require=PDGid==-11
virtualdetector  DDNT1 radius=31.75 length=0.001 color=0,1,1 \
format=root require=PDGid==-11
virtualdetector  DQ4   radius=24    length=0.001 color=0,1,1 \
format=root
virtualdetector  DD1UP radius=24    length=0.001 color=0,1,1 \
format=root
virtualdetector  D45   radius=24    length=0.001 color=0,1,1 \
format=root
virtualdetector  DD2DN radius=24    length=0.001 color=0,1,1 \
format=root
virtualdetector  NaIL  radius=24    length=76.2  color=0,1,1 \
format=root
virtualdetector  NaIR  radius=24    length=76.2  color=0,1,1 \
format=root
```

```
virtualdetector  DT2UP radius=31.75 length=0.001 color=0,1,1 \
format=root
virtualdetector  DT2DN radius=31.75 length=0.001 color=0,1,1 \
format=root
#beampipe.
param -unset PbColor1=0.5,0.5,0.0,0.5 PbColor2=0.5,0.0,0.5,0.5
tubs  PbColR1 innerRadius=40    outerRadius=25.4*2+40 \
length=25.2*2+76.2+25.2*2 material=Pb color=$PbColor1
tubs  PbColL1 innerRadius=40    outerRadius=25.4*2+40 \
length=25.2*2+76.2+25.2*2 material=Pb color=$PbColor1
tubs  PbColR2 innerRadius=25.4   outerRadius=40 \
length=25.2*2   material=Pb color=$PbColor2
tubs  PbColL2 innerRadius=25.4   outerRadius=40 \
length=25.2*2   material=Pb color=$PbColor2
#place virtual detectors.
place DG         z=$DG_z
place T1         z=$T1_z              rotation=X-45
place DUPT1      z=$FDT1_z
place DT1        z=$DT1_z             rotation=X-45
place DDNT1      z=$DBT1_z+2
place DQ4        z=$DQ4_z
place DD1UP      z=$DD1_z
place DD2DN      z=$Deg90_z x=$Q8_x-80 rotation=Y90
place D45 z=$Q7_z+$Q7OFF-40 x=$Q7_x-$Q7OFF-40 rotation=Y45
#place quadrupoles.
place QuadTypeQC rename=Q1  gradient=$g_Q1  z=$Q1_z
place QuadTypeQC rename=Q2  gradient=$g_Q2  z=$Q2_z
place QuadTypeQC rename=Q3  gradient=$g_Q3  z=$Q3_z
place QuadTypeQC rename=Q4  gradient=$g_Q4  z=$Q4_z
place QuadTypeQC rename=Q5  gradient=$g_Q5  z=$Q5_z
```

```
place QuadTypeQC rename=Q6  gradient=$g_Q6  z=$Q6_z
place QuadTypeII rename=Q8  gradient=$g_Q8  z=$Deg90_z \
x=$Q8_x       rotation=Y90
place QuadTypeII rename=Q9  gradient=$g_Q9  z=$Deg90_z \
x=$Q9_x       rotation=Y90
place QuadTypeII rename=Q10 gradient=$g_Q10 z=$Deg90_z \
x=$Q10_x      rotation=Y90
place QuadTypeQC rename=Q7  gradient=$g_Q7  z=$Q7_z+$Q7OFF \
x=$Q7_x-$Q7OFF rotation=Y45
#place detection system
place PbColR1    z=$NaIR_z  x=$NaI_x
place PbColL1    z=$NaIL_z  x=$NaI_x
place PbColR2    z=$NaIR_z-38.1-25.4 x=$NaI_x
place PbColL2    z=$NaIL_z+38.1+25.4 x=$NaI_x
place NaIR       z=$NaIR_z     x=$NaI_x
place NaIL       z=$NaIL_z     x=$NaI_x
place T2         z=$Deg90_z    x=$NaI_x        rotation=Y-45,X45
place DT2UP      z=$Deg90_z  x=$NaI_x-26.52  rotation=Y90,X45
place DT2DN      z=$Deg90_z  x=$NaI_x+26.52  rotation=Y90,X45
#dipoles.
param -unset Test_mom=sqrt(3^2-0.510998910^2)
param -unset By_1MeV=-0.0146422385 By_2MeV=-0.0329363535 \
By_3MeV=-0.0503527912 By_4MeV=-0.0675724021 By_5MeV=-0.0847114822
param -unset Zoffset=0 Xoffset=0 D2_Zoffset=0 D2_Xoffset=0
param -unset Mom1=sqrt(1^2-0.510998910^2) \
Mom2=sqrt(2^2-0.510998910^2) Mom3=sqrt(3^2-0.510998910^2) \
Mom4=sqrt(4^2-0.510998910^2) Mom5=sqrt(5^2-0.510998910^2)
param -unset Mom=$Mom5 By_MeV=$By_5MeV
genericbend B fieldWidth=150 fieldHeight=25 fieldLength=150 \
ironColor=1,0,0 ironWidth=240 ironHeight=240 ironLength=150
```

```
place B rename=B1 By=$By_MeV z=$D1_z+$Zoffset x=$Xoffset \
 rotation=Y22.5
place B rename=B1 By=$By_MeV z=$D2_z+$D2_Zoffset x=$D2_x+$D2_Xoffset \
rotation=Y67.5
#generate beam.
param -unset RMul=1
beam gaussian sigmaX=sqrt($emitX*$betaX) sigmaY=sqrt($emitY*$betaY) \
sigmaXp=sqrt($emitX*$gammaX) sigmaYp=sqrt($emitY*$gammaY) particle=e-\
beamX=0 beamY=0 beamZ=$beam_z meanMomentum=0.85958 nEvents=10*$RMul
beam gaussian particle=e+ beamX=0 sigmaX=0 beamY=0 sigmaY=0 \
beamZ=2419.8994140625 beamXp=0 sigmaXp=0 beamYp=0 sigmaYp=0 \
meanMomentum=$Mom nEvents=20*$RMul
```